

Copyright Warning & Restrictions

The copyright law of the United States (Title 17, United States Code) governs the making of photocopies or other reproductions of copyrighted material.

Under certain conditions specified in the law, libraries and archives are authorized to furnish a photocopy or other reproduction. One of these specified conditions is that the photocopy or reproduction is not to be “used for any purpose other than private study, scholarship, or research.” If a user makes a request for, or later uses, a photocopy or reproduction for purposes in excess of “fair use” that user may be liable for copyright infringement,

This institution reserves the right to refuse to accept a copying order if, in its judgment, fulfillment of the order would involve violation of copyright law.

Please Note: The author retains the copyright while the New Jersey Institute of Technology reserves the right to distribute this thesis or dissertation

Printing note: If you do not wish to print this page, then select “Pages from: first page # to: last page #” on the print dialog screen

The Van Houten library has removed some of the personal information and all signatures from the approval page and biographical sketches of theses and dissertations in order to protect the identity of NJIT graduates and faculty.

ABSTRACT

Modeling and Simulation of Magnetic Micromotor Performance

by

Ping Wang

The objective of this research was to model the performance and optimize geometries for two types of magnetic micromotors: yoke-type (YTMM) and yokeless (YSMM). The two selected micromotor types matched the designs that have been described in the recent research literature. Modeling was accomplished using MAXWELL, an advanced 2-D and 3-D simulator. The micromotors with nickel and nickel-iron magnetic thin films for the rotor and stator were simulated for torque performance. Three-phase power supplies with overlapping and non-overlapping phases were used. Rotor diameter dimensions were varied from 285 to 600 μm , and the rotor-stator air gap was varied from 3 to 5 μm . The number of rotor poles was varied from 4 to 10. The maximum torque obtained from the YTMM was in the range 76nNt-m to 360nNt-m, depending on geometry and permeability. The maximum torque that could be obtained from the YSMM was 15.5nNt-m, which was considerably less than that for the YTMM for comparable permeability, dimensions, and rotor/stator pole combinations. The torque advantage of the YTMM is due to the decreased reluctance in the magnetic path. Simulation indicated that the motor torque increased with ampere turns, rotor/stator pole thickness, relative permeability of the material, and the number of rotor/stator poles. The torque was found to decrease as the inverse air gap separation. This work is significant because it is the first detailed study of magnetic micromotors by computer simulation.

**MODELING AND SIMULATION OF MAGNETIC
MICROMOTOR PERFORMANCE**

by
Ping Wang

**A Thesis
Submitted to the Faculty of
New Jersey Institute of Technology
in Partial Fulfillment of the Requirements for the Degree of
Master of Science in Electrical Engineering**

Department of Electrical and Computer Engineering

May 1993

APPROVAL PAGE

Modeling and Simulation of Magnetic Micromotor Performance

by

Ping Wang

Dr. William N. Carr, Thesis Adviser
Professor and Holder of Sponsored Chair in Microelectronics, NJIT

5/13/93
Date

Dr. Roy H. Cornely, Committee Member
Professor of Electrical Engineering, NJIT

5/12/93
Date

Dr. Durga Misra, Committee Member
Assistant Professor of Electrical Engineering, NJIT

5/6/93
Date

BIOGRAPHICAL SKETCH

Author: Ping Wang

Degree: Master of Science in Electrical Engineering

Date: May 1993

Date of Birth:

Place of Birth:

Undergraduate and Graduate Education:

- Master of Science in Electrical Engineering,
New Jersey Institute of Technology, Newark, NJ, 1993
- Bachelor of Science in Electrical Engineering,
Shanghai Jiao Tong University, China, 1989

Major: Electrical Engineering

Dedicated to
My Mother

ACKNOWLEDGMENT

I have a chance here to express my sincere gratitude to many people who assisted me during my thesis work, especially to my graduate advisor Dr. William N. Carr for his guidance and inspiration. Without his support, the thesis would not be done.

Special thanks to Dr. Roy Cornely and Dr. Durga Misra for serving as members of the committee.

I would also like to express my appreciation to my friends at NJIT, who gave me their kindly assistance. I feel particularly grateful to Guang Yang, Susan Wu, Robert Okojie, Paul Gelencser, Chao Ye and Chao Sun who helped me a lot for my thesis. And I am greatly indebted to my sponsor Fen-Dow Chu and his wife Petra Chu who have supported me a lot these years in America.

Finially, a sincerely thank you to my mother. She is always my support.

TABLE OF CONTENTS

Chapter	Page
1 INTRODUCTION.....	1
1.1 Introduction.....	1
1.2 References	7
2 ANALYSIS OF THE YOKE-TYPE VARIABLE RELUCTANCE MAGNETIC MICROMOTOR	8
2.1 Previous Research	8
2.2 Structures and Processes	11
2.3 Performance Modeling	13
2.3.1 Selected Geometry	13
2.3.2 First Order Analytical Model	15
2.3.3 Numerical Modeling with MAXWELL	18
2.4 Variation of Torque with Important Design Parameters	44
2.4.1 Variation of Torque with Relative Permeability	44
2.4.2 Variation of Torque with Air Gap	45
2.5 Summary of Modeling Results	47
2.6 References	49
3 ANALYSIS OF YOKELESS VARIABLE RELUCTANCE MAGNETIC MICROMOTOR	51
3.1 Previous Research	51
3.2 Structures and Processes	52
3.2.1 Structures	52
3.2.2 Processes	55
3.3 Performance Modeling	60
3.3.1 Selected Geometry	60
3.3.2 First Order Analytical Model	61

Chapter	Page
3.3.3 Numerical Modeling with MAXWELL	63
3.4 Summary of Modeling Results	68
3.5 References	68
4 CONCLUSIONS	70
APPENDIX A MAXWELL PROGRAMMING DETAIL (EXAMPLE SCREENS FOR YTMM-5)	73
APPENDIX B BOUNDARY CONDITIONS FOR 2-D AND 3-D SIMULATIONS	95

LIST OF TABLES

Table	Page
4.1 Different magnetic micromotor designs and the relative characteristics	71

LIST OF FIGURES

Figure	Page
1.1 Magnetic micromotor (top view) -- not to scale.	3
1.2 Photomicrograph of a fabricated and assembled planar reluctance magnetic micromotor [1.3].	4
1.3 SEM photomicrograph of a completed and packaged magnetic micromotor [1.2].	4
1.4 A three-dimensional YTMM geometry -- not to scale.	5
2.1 Conventional variable reluctance magnetic motor -- not to scale.	8
2.2 Photomicrograph of integrated planar magnetic micromotor [2.1].	10
2.3 Simplified cross sectional processing sequence [2.1].	11
2.4 Yoke-type magnetic micromotor ($P_s/P_r=6/4$) -- not to scale.	13
2.5 Yoke-type magnetic micromotor ($P_s/P_r=12/8$) -- not to scale.	14
2.6 Symbols and axis defined for a rotor-stator pole pair.	15
2.7 Yoke-type magnetic micromotor YTMM-1 -- not to scale.	18
2.8 YTMM-1 with coils wrapped around stator poles Drawn to scale using MAXWELL.....	19
2.9 Magnetic flux for YTMM-1 with one stator pole pair active ($P_s/P_r=6/4$). Rotor diameter= $285\mu\text{m}$	20
2.10 Optical photomicrograph of magnetic micromotor [2.1].	21
2.11 Torque curve for YTMM-1 micromotor with non-overlapping current supply phase sequence.	22
2.12 Torque curve for YTMM-1 micromotor with overlapping current supply phase sequence.	24
2.13 Yoke-type magnetic micromotor YTMM-2 -- not to scale.	25
2.14 Torque curve for YTMM-2 micromotor with non-overlapping current supply phase sequence.	27
2.15 Torque curve for YTMM-2 micromotor with overlapping current supply phase sequence.	29

Figure	Page
2.16 Yoke-type magnetic micromotor YTMM-3 -- not to scale.	30
2.17 The micromotor with coils wrapped around one stator pole pair. Drawn to scale using MAXWELL.....	31
2.18 The magnetic flux across the entire micromotor when only one stator pole pair active. Rotor diameter=285 μ m.	32
2.19 Torque curve for YTMM-3 micromotor with non-overlapping current supply phase sequence.	33
2.20 Torque curve for YTMM-3 micromotor with overlapping current supply phase sequence.	35
2.21 Yoke-type magnetic micromotor YTMM-4 -- not to scale.	36
2.22 Torque curve for YTMM-4 micromotor with non-overlapping current supply phase sequence.	37
2.23 Torque curve for YTMM-4 micromotor with overlapping current supply phase sequence.	39
2.24 Yoke-type magnetic micromotor YTMM-5 -- not to scale.	40
2.25 Torque curve for YTMM-5 micromotor with non-overlapping current supply phase sequence.	41
2.26 Torque curve for YTMM-5 micromotor with overlapping current supply phase sequence.	43
2.27 Maximum torque T_{\max} versus relative permeability μ_r	45
2.28 Maximum torque T_{\max} versus the air gap g	46
3.1 Schematic diagram of modified planar variable reluctance magnetic micromotor. The structure consists of 12 stator poles and 10 rotor poles in three-phase [3.1].	53
3.2 Meander type inductive component (top). A multilevel magnetic core is "wrapped" around a planar conductor coil. This structure is similar to the standard inductive component (bottom) [3.1].	54
3.3 Fabrication process for the micromotor.	57
3.4 Photomicrograph of the fully fabricated micromotor [3.1].	58
3.5 Photomicrograph of the actuated rotor. When 0.5A current was applied to each stator phase, 12 degrees of rotation was observed [3.1].	59
3.6 Yokeless magnetic micromotor geometry YSMM ($P_s/P_r=12/10$). Drawn to scale using MAXWELL.	61

Figure	Page
3.7 Magnetic flux for YSMM with two stator pole pairs active (Ps/Pr=12/10). The orientation is the same as Figure 3.6. Rotor diameter=600 μ m.	64
3.8 Torque curve for YSMM micromotor with non-overlapping current supply phase sequence.	65
3.9 Torque curve for YSMM micromotor with overlapping current supply phase sequence.	67
A.1 Screen of setting the unit.	73
A.2 Screen of setting the grid type.	74
A.3 Screen of "Axis" sub-menu.	75
A.4 Screen of "line" sub-menu.	76
A.5 Screen of "edit" sub-menu.	77
A.6 Screen of "mesh" sub-menu.	78
A.7 Screen of "Refine" sub-menu.	79
A.8 Screen of geometry with mesh.	80
A.9 Screen of "file" sub-menu.	81
A.10 Screen of "Att Set" sub-menu.	82
A.11 Screens of setting the parameters for different materials in this problem.	86
A.12 Screen of "B Pick" sub-menu.	87
A.13 Screen of "B Type" sub-menu.	88
A.14 Screen of "Solve" sub-menu.	89
A.15 Screen of "post" -- "line" sub-menu.	90
A.16 Screen of "Lne Calc" sub-menu.	91
A.17 Screen of "Lne Calc" sub-menu with calculating result.	92
A.18 Screen of "plot" sub-menu.	93
A.19 Screen of "Equi" settings.	94
B.1 Lines of magnetic field at Neumann, Dirichlet and Ballooned Boundaries.	96

CHAPTER 1

INTRODUCTION

1.1 Introduction

This research models the performance of two kinds of magnetic micromotors: yoke-type (YTMM) and yokeless (YSMM) micromotors. The yoke-type magnetic micromotors (YTMM) are studied with several rotor, stator and air gap configurations. The rotor diameter varies from $3\mu\text{m}$ to $4.5\mu\text{m}$. The YTMM micromotors provide peak torques in the range $76\text{nNt}\cdot\text{m}$ to $360\text{nNt}\cdot\text{m}$. The design for yokeless magnetic micromotor (YSMM) is $600\mu\text{m}$ rotor diameter, $5\mu\text{m}$ air gap, 12 stator poles and 10 rotor poles. The maximum torque is $15.5\text{nNt}\cdot\text{m}$. These micromotors are made of nickel and nickel-iron. It is concluded that the torque increases when the air gap decreases, the number of rotor and stator poles increases, the ampere turns (NI) increases, the rotor and stator pole thickness increase, and the relative permeability μ_r of the magnetic path increases. YTMM has a greater torque than YSMM with comparable dimensions.

The rapidly developing integrated-circuit (IC) technology has made great changes in the world today. Many of the materials and processes used to produce integrated microcircuits are now used in new ways to produce microsensors and transducers. Micromechanical transducer structures such as micro-bridges, diaphragms, and cantilevers have

been fabricated by silicon processing for various useful applications. Micromachines with rotatable joints, sliding or translating members, and mechanical-energy storage elements provide the basis for more general micromachine designs. IC-based microfabrication processes utilizing these microstructures are now being investigated for micromachines.

As a technology for accurately fabricating very small structures with or without assembly, silicon micromachining is developing very fast. Silicon micromachining was used to fabricate structures that have rotary or linear bearings allowing motion of the moving component in one degree of freedom.

A micromotor is a micromachine that has rotatable or translational bearings driven by magnetic or electrical fields. They are physically much smaller than motors manufactured using conventional technology with the potential of great manufacturing economic effects. Micromotors have very low moments of inertia and develop low internal stresses during operation. They are ideally suited for high-speed operation. Magnetic micromotors can be fabricated with a variety of magnetic materials. So far they have been made with nickel and nickel-iron electroformed magnetic materials. During recent years, there has been much research work toward realizing practical micromotors for a variety of applications by using both magnetic and electrostatic designs. The magnetic micromotors were only recently demonstrated for the first time in 1993 [1.1][1.2]. Magnetic micromotors will potentially have applications in a myriad of systems, such as biomedical implanted actuators and very small, very high speed computer hard disk drivers. Longer term, the economics of mass produced micromotors should

result in many automotive, consumer electronics, and industrial control applications.

A magnetic micromotor is shown in Figure 1.1. The rotor and the stator each have a different number of poles. Coils are wrapped around the stator poles to create a magnetic field in the gap between the rotor and stator. Each coil is electrically isolated from the others. The rotor will rotate incrementally until the rotor poles align with the stator poles in an equilibrium position where the system has maximum reluctance. When the stator currents are turned on and off sequentially, the rotor can rotate continuously. Figure 1.2 is a photomicrograph of a fabricated and assembled planar reluctance magnetic micromotor [1.2].

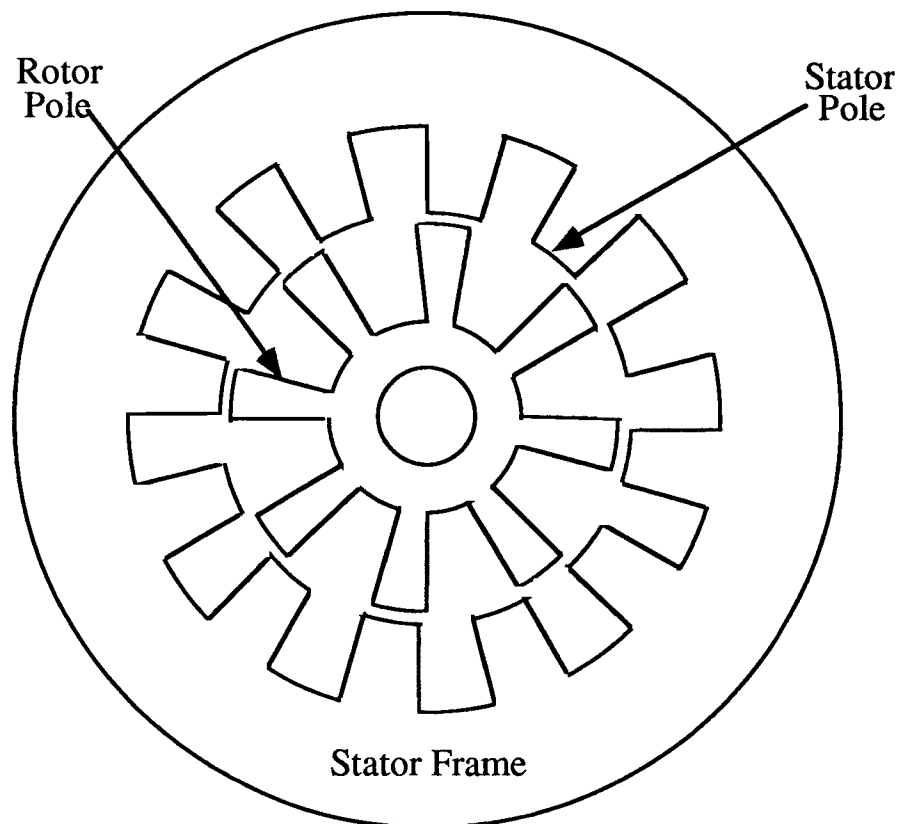


Figure 1.1 Magnetic micromotor, yoke-type (top view) -- not to scale.

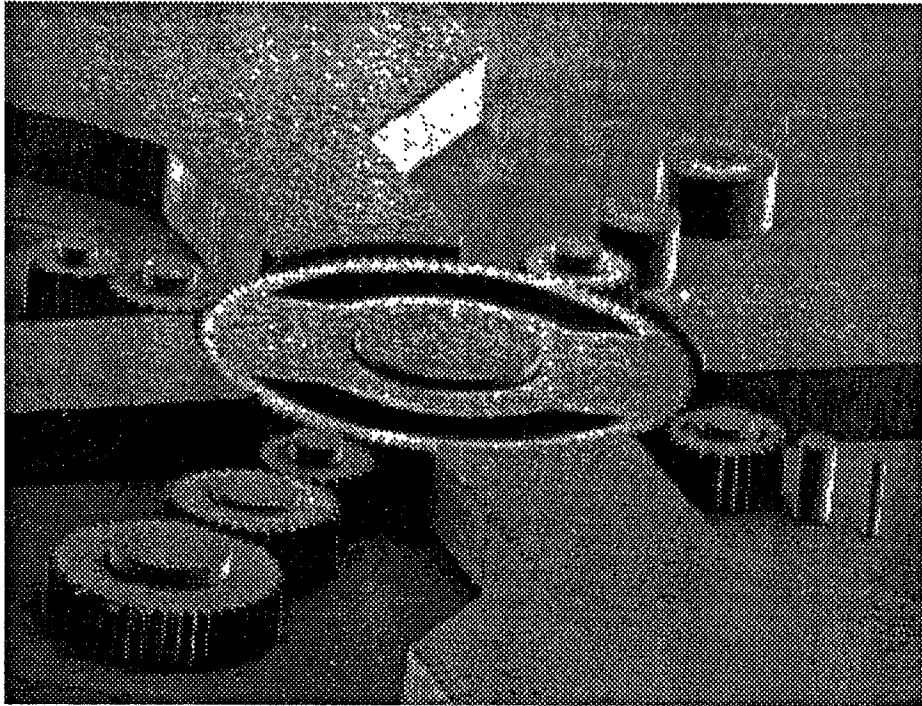


Figure 1.2 Photomicrograph of a fabricated and assembled planar reluctance magnetic micromotor [1.3]

A SEM photomicrograph of a completed and packaged magnetic micromotor is shown in Figure 1.3. The flat pack is 2.5cm x 2.5cm

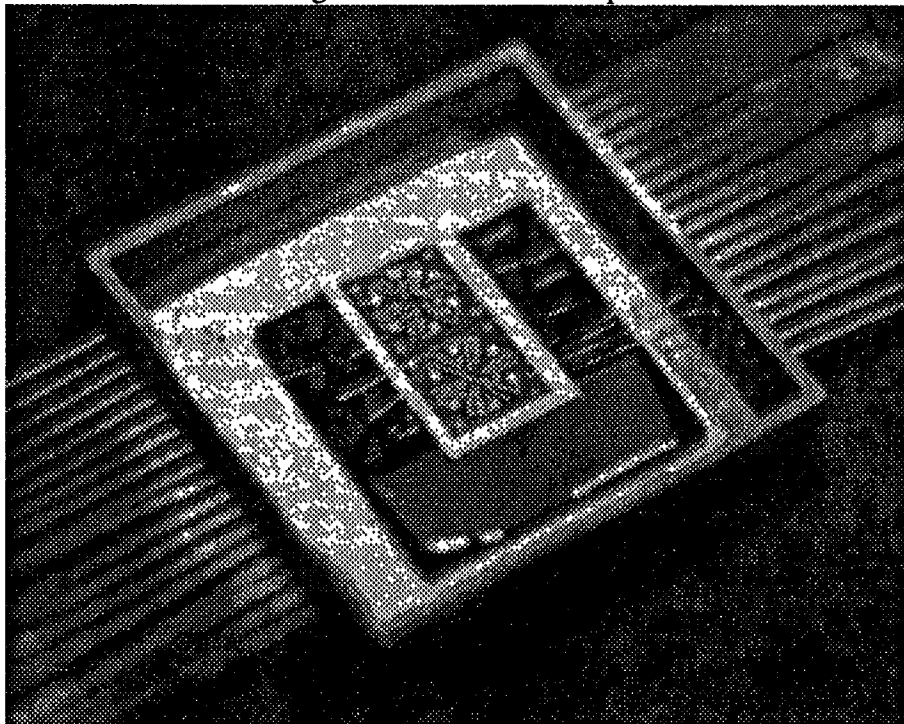


Figure 1.3 SEM photomicrograph of a completed and packaged magnetic micromotor [1.2].

and contains two motor dies [1.1]. Compared with the electrostatic micromotor, the magnetic micromotor has much greater torque. For example, a magnetic micromotor can reach a torque of $360\text{nNt}\cdot\text{m}$, but an electrostatic micromotor of comparable dimension develops $80\text{pNt}\cdot\text{m}$ of torque [1.4]. With this larger torque, the magnetic micromotor is expected to find extensive applications.

The two magnetic micromotor designs available today are of the variable reluctance type. We define one of these micromotors: the **Yoke-Type Variable Reluctance Magnetic Micromotor (YTMM)**. A three-dimensional YTMM geometry is shown in Figure 1.4 and discussed in chapter 2. Because there is an energy loss

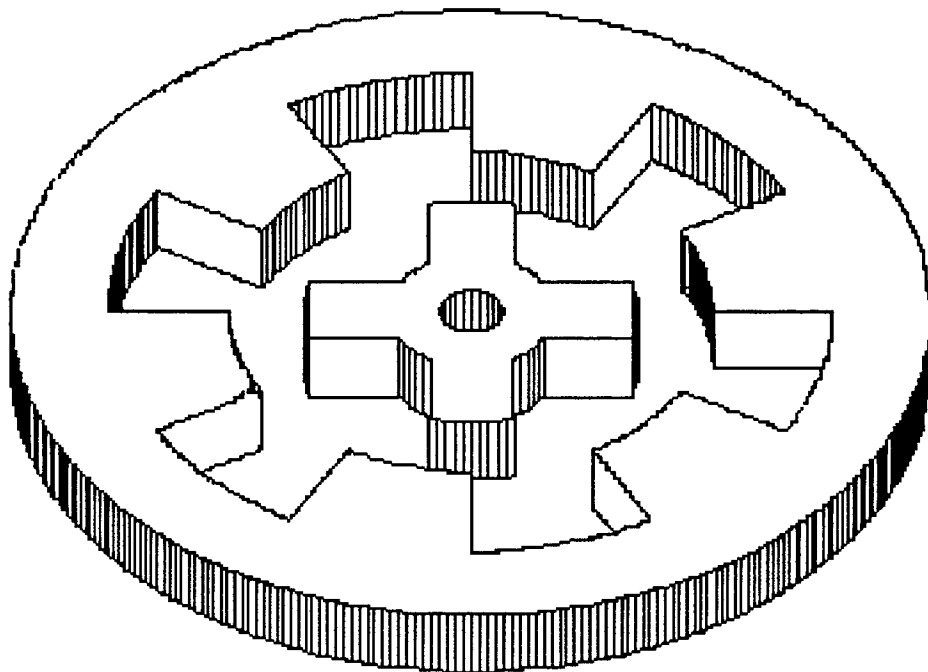


Figure 1.4 A three-dimensional YTMM geometry -- not to scale.

in the stator frame magnetic path, a modified structure has been developed and discussed in chapter 3. It still has a reluctance path, but it is a small one and totally different from the yoke-type (YTMM) structure. This second configuration does not contain a magnetic return path across all stator poles. We define this type of micromotor: the **Yokeless Variable Reluctance Magnetic Micromotor (YSMM)**.

Chapter 2 describes the **Yoke-Type Variable Reluctance Magnetic Micromotor (YTMM)**. Simulations with MAXWELL have been made for this type of micromotor with different rotor and stator pole combinations, rotor diameters, and magnetic gaps.

Chapter 3 describes the second type of magnetic micromotor -- **Yokeless Variable Reluctance Magnetic Micromotor (YSMM)**. It not only uses an improved magnetic path, but also integrated coils wrapped around planar meander conductors and a fully integrated stator. Simulations with MAXWELL have been used to analyze the performance of this micromotor also.

Chapter 3 describes the second type of magnetic micromotor -- **Yokeless Variable Reluctance Magnetic Micromotor (YSMM)**. It not only uses an improved magnetic path, but also integrated coils wrapped around planar meander conductors and a fully integrated stator. Simulations with MAXWELL have been used to analyze the performance of this micromotor also.

1.2 References

- [1.1] Chong H. Ahn, Yong J. Kim, and Mark G. Allen, "A planar variable reluctance magnetic micromotor with fully integrated stator and wrapped coils", Fort Lauderdale, Florida, February, 1993. (IEEE Catalog Number 93DH3265-6).
- [1.2] H. Guckel and K. J. Skrobis, "A first functional current excited planar rotational magnetic micromotor", Fort Lauderdale, Florida, February, 1993. (IEEE Catalog Number 93DH3265-6).
- [1.3] H. Guckel and K. J. Skrobis, "Fabrication and testing of the planar magnetic micromotor", Journal of Micromechanics and Microengineering, August, 1991.
- [1.4] H. Yu, "Electrostatic micromotor design and simulation", M.S. Thesis, NJIT, 1991.

CHAPTER 2

ANALYSIS OF THE YOKE-TYPE VARIABLE RELUCTANCE MAGNETIC MICROMOTOR (YTMM)

2.1 Previous Research

The Yoke-Type variable reluctance Magnetic Micromotor (YTMM) is a type of conventional variable reluctance magnetic motor. The YTMM consists of the rotor and the stator, as shown in Figure 2.1.

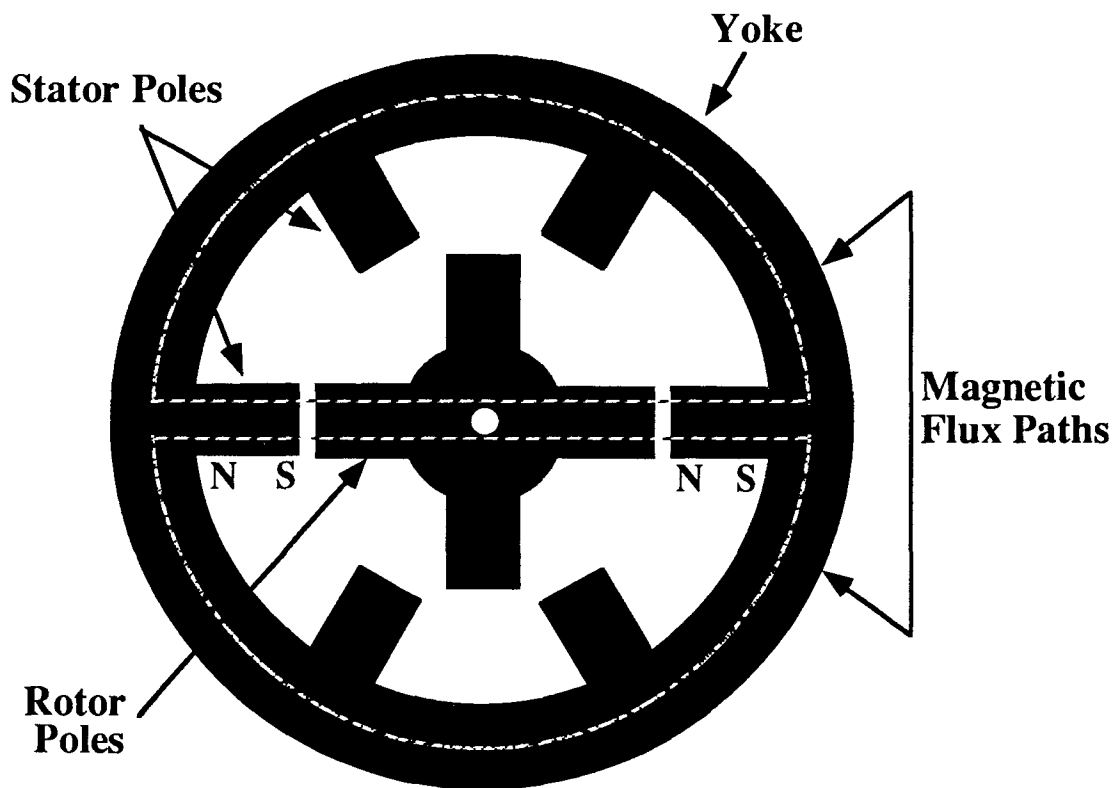


Figure 2.1 Conventional variable reluctance magnetic motor

-- not to scale.

The stator poles require magnetic yokes to reduce the reluctance of the magnetic path, from one stator pole, through the rotor, through the stator pole directly across from the first stator pole, and back around the yoke to the first pole. The reluctance between stator poles for each torque producing current pulse should be minimized. For "conventional" large scale motors, the reluctance of the yoke is so small that it can usually be neglected, but the reluctance of the yoke is significant in a micromotor. For a micromotor, the yoke reduces the motor size and can be fabricated in cleanroom with IC technology. The fabrication of the micromotor is based on deep x-ray lithography and electroplating processing or LIGA, which has been shown to be integrable with standard IC processing [2.2], and allow structure replication independent of a synchrotron [2.3]. Figure 2.2 is a photomicrograph of an integrated planar magnetic micromotor recently reported [2.1]. This motor has six stator poles and four rotor poles. Three pairs of stator poles have three separate phases of current supplied with timing for maximum average torque.

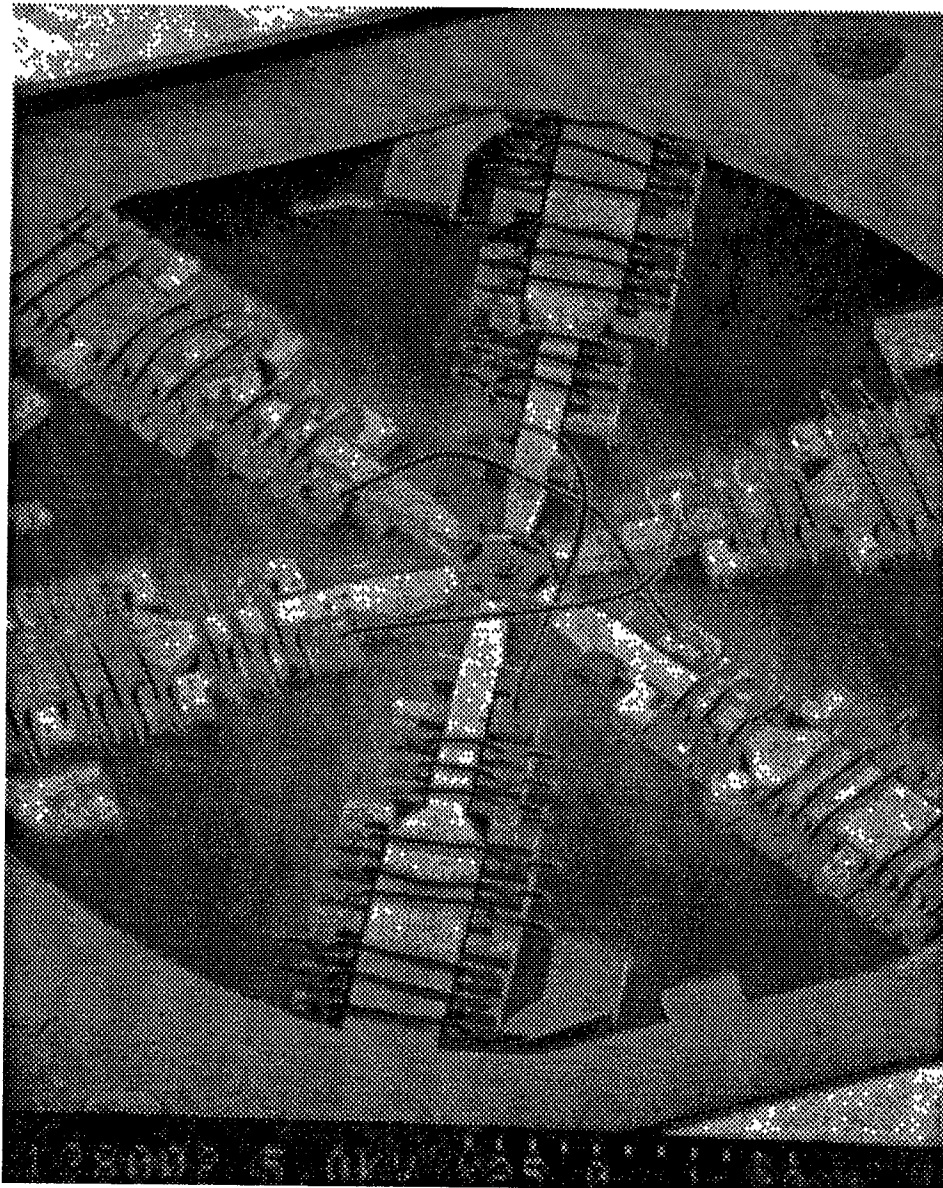


Figure 2.2 Photomicrograph of integrated planar magnetic micromotor [2.1].

2.2 Structures and Processes

A simplified cross sectional fabricating process sequence is shown in Figure 2.3. Four optical mask levels are required in addition to two x-ray masks for this type of magnetic micromotor.

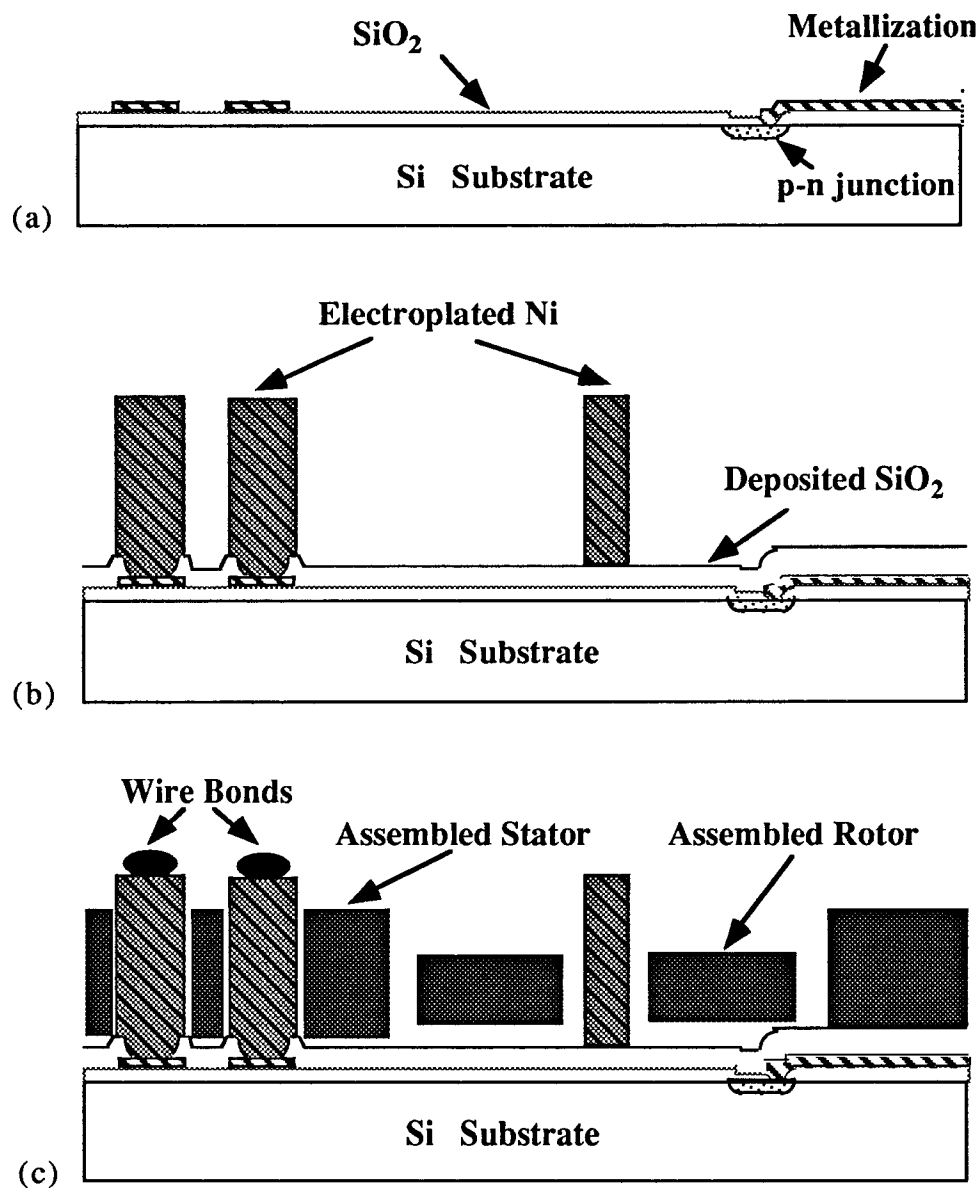


Figure 2.3 A simplified cross sectional processing sequence [2.1].

Glasses, metals and semiconductors can be used as flat substrates to fabricate the motor levels. In the Wisconsin process [2.1], three inch silicon substrates were used [2.1] to allow fabrication of integrated silicon p-n junction photodetectors. First, a $0.6\mu\text{m}$ thermal oxide was used to electrically isolate the substrate. Mask level #1 defines the photodiode geometry through this oxide. This is followed by "implant", "drive" and "oxidize" steps. Mask level #2 is used to define the contact to the photodiodes. Mask level #3 is used to pattern the metallization layer with $4\mu\text{m}$ of nickel on a 20nm Ti adhesion layer and to define the current winding vias which lies under the stator poles as well as photodiode connection runners [2.1].

Micromotor fabrication continues with a $2.0\mu\text{m}$ deposited oxide to provide isolation between the windings and the magnetic paths. This oxide layer is defined by the fourth mask to open up contact areas to the nickel metallization layer for coil and photodiode connection. Deep x-ray lithography and electroplating sequences follow. First, a plating base of 30nm Ti plus 30nm Ni is sputtered which is covered by a cast PMMA layer of several hundred microns. The first x-ray mask is used to expose the areas of PMMA where nickel will be electroplated and permanently attached to the substrate. These areas include the vertical portions of the coil, the rotor bearing post, and guide pins for the stator. Removal of PMMA and plating base in the field regions completes processing for this level (Figure 2.3 (b)). The stator and rotor are defined with a second x-ray exposure on a substrate which is provided with an unpatterned sacrificial layer. Since the stator and rotor are assembled, different designs may be tested on the same motor substrate

pattern. Rotors with various bearing tolerances and outside diameters may be tested with the same motor. Figure 2.3 (c) shows the processing cross section after stator and rotor assembly and wire bonding.

2.3 Performance Modeling

2.3.1 Selected Geometry

The geometries of the yoke-type magnetic micromotor are shown in Figure 2.4 and Figure 2.5. Figure 2.4 shows the micromotor with six

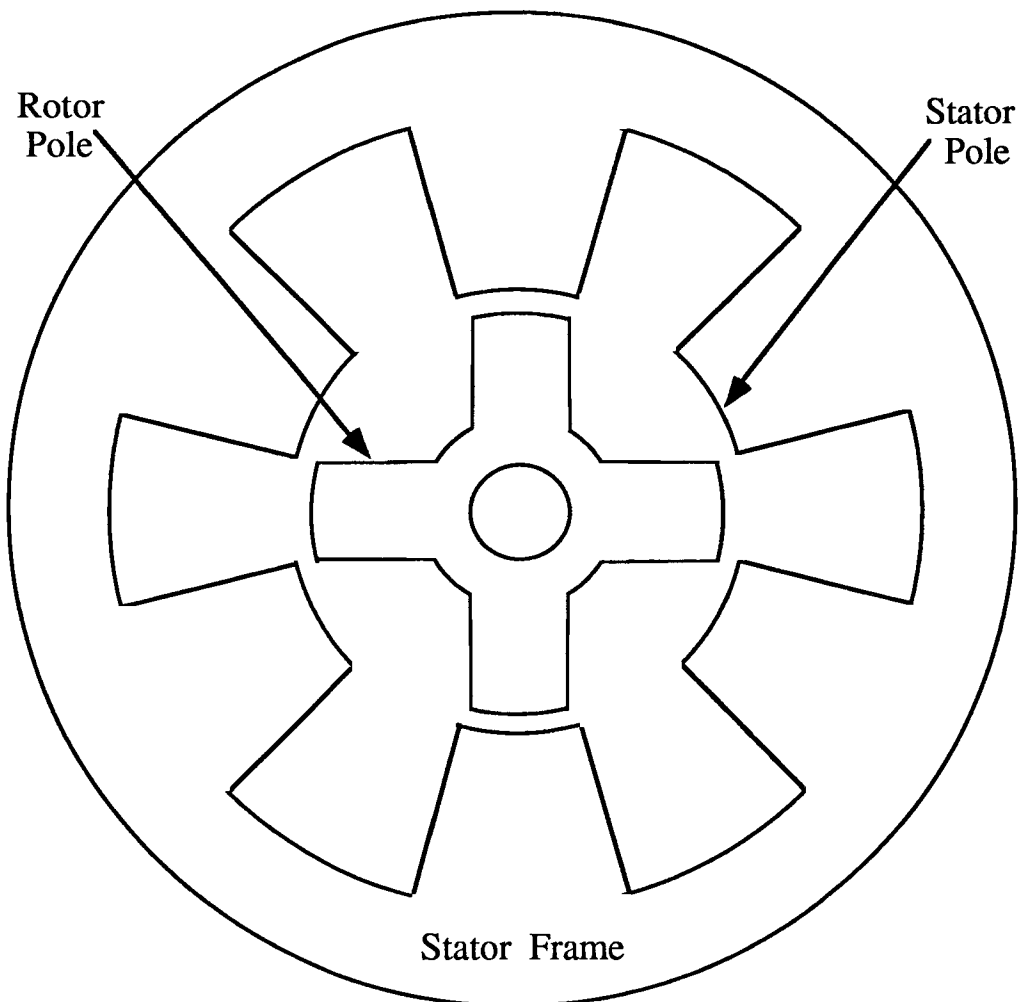


Figure 2.4 Yoke-type magnetic micromotor ($P_s/P_r=6/4$) -- not to scale.

stator poles and four rotor poles. Figure 2.5 shows the micromotor with 12 stator poles and eight rotor poles. These two micromotor geometries can have different rotor and bearing diameters. Simulations based on the geometry of Figure 2.4 used two rotor diameters. The smaller rotor case is $285\mu\text{m}$ in diameter with a bearing post diameter of $72\mu\text{m}$ and a $3\mu\text{m}$ air gap. The larger rotor case is $423\mu\text{m}$ in diameter with a bearing post diameter of $108\mu\text{m}$ and a $3\mu\text{m}$ air gap. Additional simulations have been performed for the geometry of Figure 2.5. The smaller rotor case is $285\mu\text{m}$ in diameter with a bearing post diameter of $72\mu\text{m}$ and a $3\mu\text{m}$ air gap as in Figure 2.4. The larger rotor case is $423\mu\text{m}$ in diameter with a bearing post diameter of $108\mu\text{m}$, a $3\mu\text{m}$ air gap and a $4.5\mu\text{m}$ air gap.

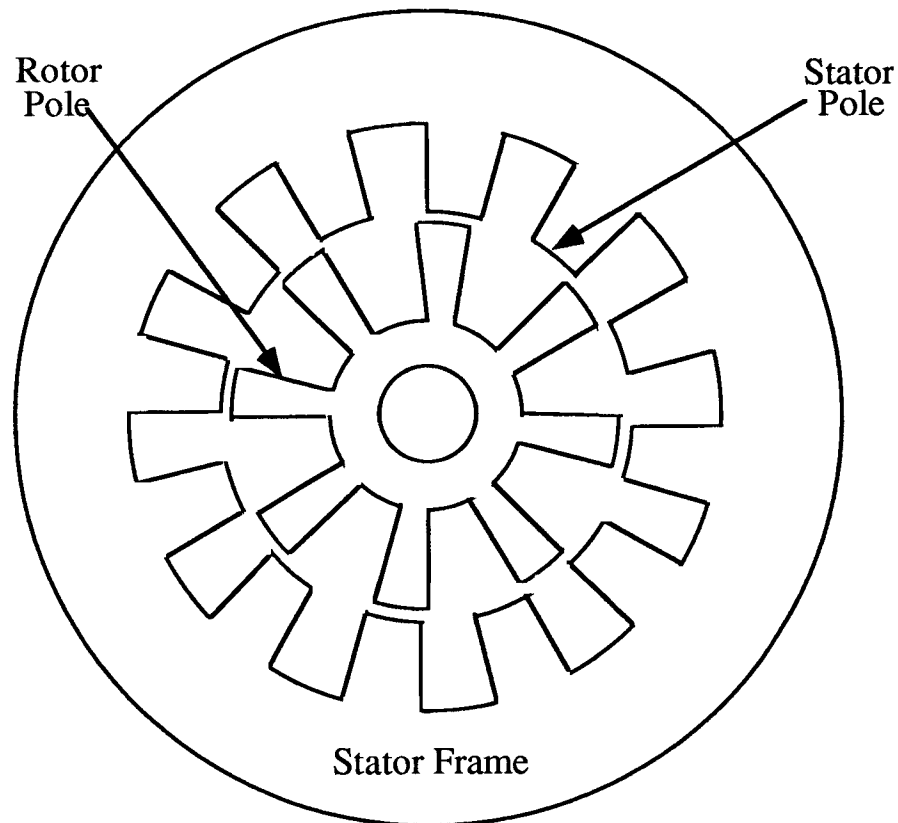


Figure 2.5 Yoke-type magnetic micromotor ($P_s/P_r=12/8$) -- not to scale.

The thickness of the rotor is $100\mu\text{m}$ in every case. Nickel is used as the magnetic material to fabricate the rotor and the stator. The relative permeability μ_r of nickel is 100 for the modeling in this thesis.

2.3.2 First Order Analytical Model

The motor torque can be calculated to a first order from first principles for each pole pair.

$$\mathbf{F} = -\nabla W \quad (2-1)$$

$$\mathbf{T} = \mathbf{F} \times \mathbf{r}_o \quad (2-2)$$

where \mathbf{T} is torque, W is energy stored in a pole-pair, \mathbf{F} is action force at the end of the rotor pole, \mathbf{r}_o is the rotor radius.

In an ideal case (as shown in Figure 2.6), for example:

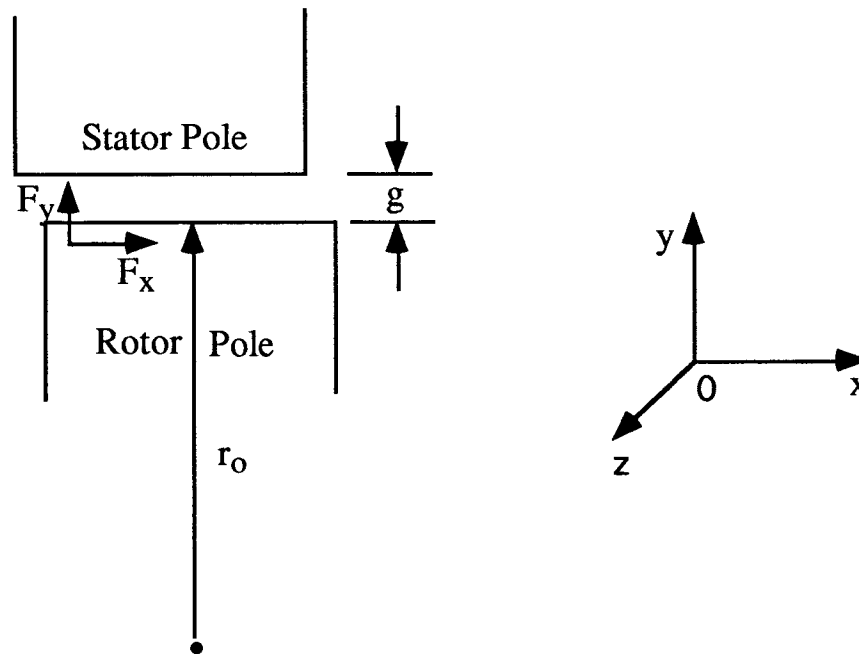


Figure 2.6 Symbols and axis defined for a rotor-stator pole pair.

When the reluctance of the magnetic circuit external to gap is neglected, the \mathbf{H} -field \mathbf{H}_g in the gap becomes

$$\mathbf{H}_g g = NI \quad (2-3)$$

The energy W stored in the pole gap is express as

$$W = \frac{1}{2} \mathbf{B}_g \mathbf{H}_g \int dV \quad (2-4)$$

or

$$W = \frac{1}{2} \mu_o \mu_r \mathbf{H}_g^2 \int dx dy dz \quad (2-5)$$

where $\mathbf{B} = \mu \mathbf{H}$

When fringing fields are neglected, the magnetic energy stored in the air gap g where $\mu_r = 1$, the following relationship is obtained

$$\mathbf{H}_g = NI / g \quad (2-6)$$

$$W = \frac{1}{2} \mu_o \left(\frac{NI}{g} \right)^2 ghx \quad (2-7)$$

where x =stator-rotor pole overlap and h =pole thickness.

The force of the rotor can now be expressed using Equation 2-1 and Equation 2-2:

$$\mathbf{F}_x = -\nabla W = \frac{1}{2} \mu_o (NI)^2 h / g \quad (2-8)$$

From Equation 2-2 and Equation 2-8, the torque of the rotor can be expressed:

$$T_x = \frac{1}{2} \mu_o (NI)^2 r_o h / g \quad (2-9)$$

From Equation 2-9, several observations can be made. For a practical multiple pole micromotor with overlapping stator currents, an additional torque multiplier M occurs due to simultaneous torque from adjacent pole pairs. The net torque including the multiplier M for a multiple pole micromotor now becomes:

$$T_x = \frac{1}{2} M \mu_o (NI)^2 r_o h / g \quad (2-10)$$

In a practical case with finite reluctance in the stator, reducing the air gap g increases torque. Also if one increases the thickness of the rotor, the torque will increase. This occurs because the reluctance of the stator magnetic path is finite. Furthermore, the torque is proportional to the square of the current-turns in this first order model. It should be emphasized that the first order model described above neglects fringing magnetic fields in the rotor-stator gap and the reluctance of the magnetic path external to the gap.

2.3.3 Numerical Modeling with MAXWELL

(1) Yoke-type magnetic micromotor geometry YTMM-1

The first magnetic micromotor geometry selected for simulation is shown in Figure 2.7 and is designated as YTMM-1.

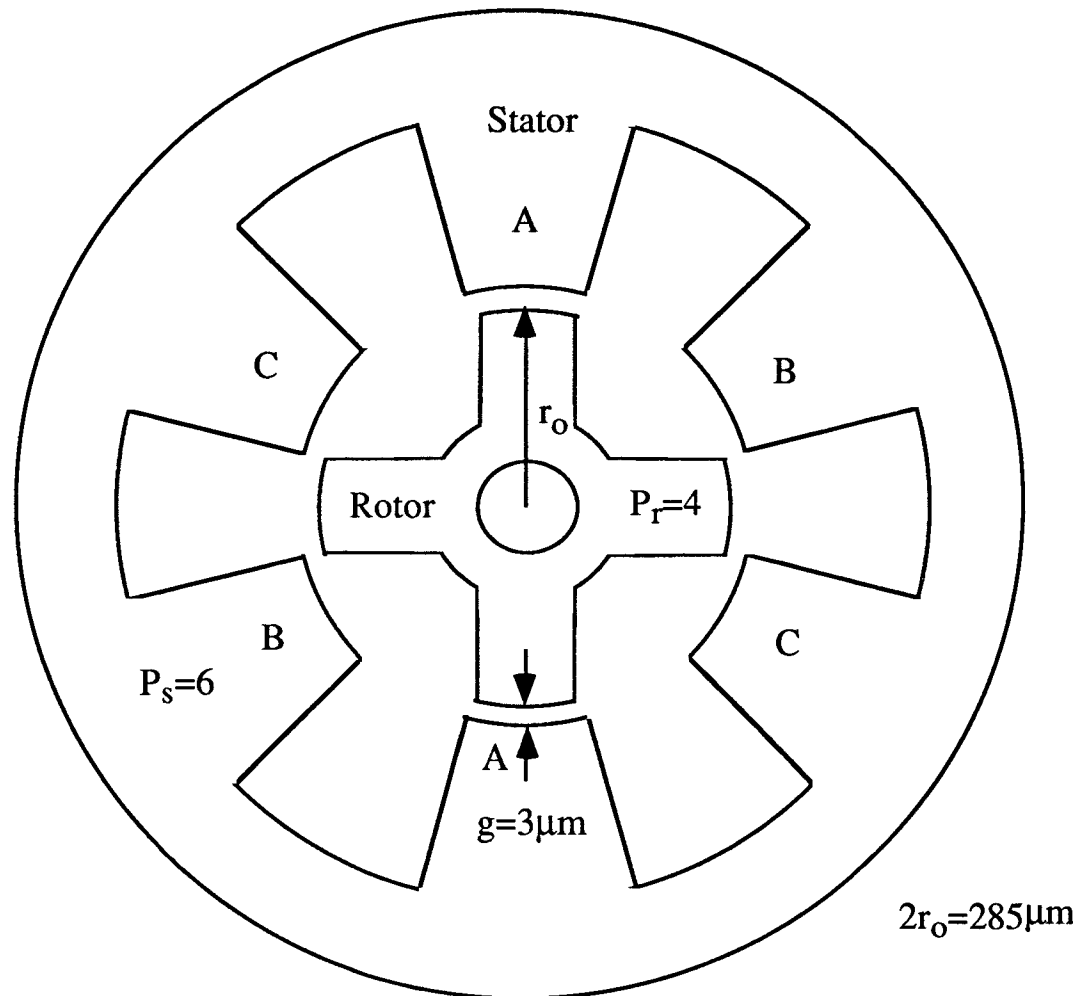


Figure 2.7 Yoke-type magnetic micromotor YTMM-1 -- not to scale.

The motor has six stator poles and four rotor poles. The rotor is $285\mu\text{m}$ in diameter with a bearing post diameter of $72\mu\text{m}$. Both the rotor

and stator poles have a width of 30 degrees. The radial rotor-stator air gap is $3\mu\text{m}$. This motor can be driven by a three-phase current. The currents can be non-overlapping or overlapping. When the stator poles are energized sequentially clockwise, the rotor will move counterclockwise. A representative micromotor with coils wrapped around the stator poles is shown in Figure 2.8.

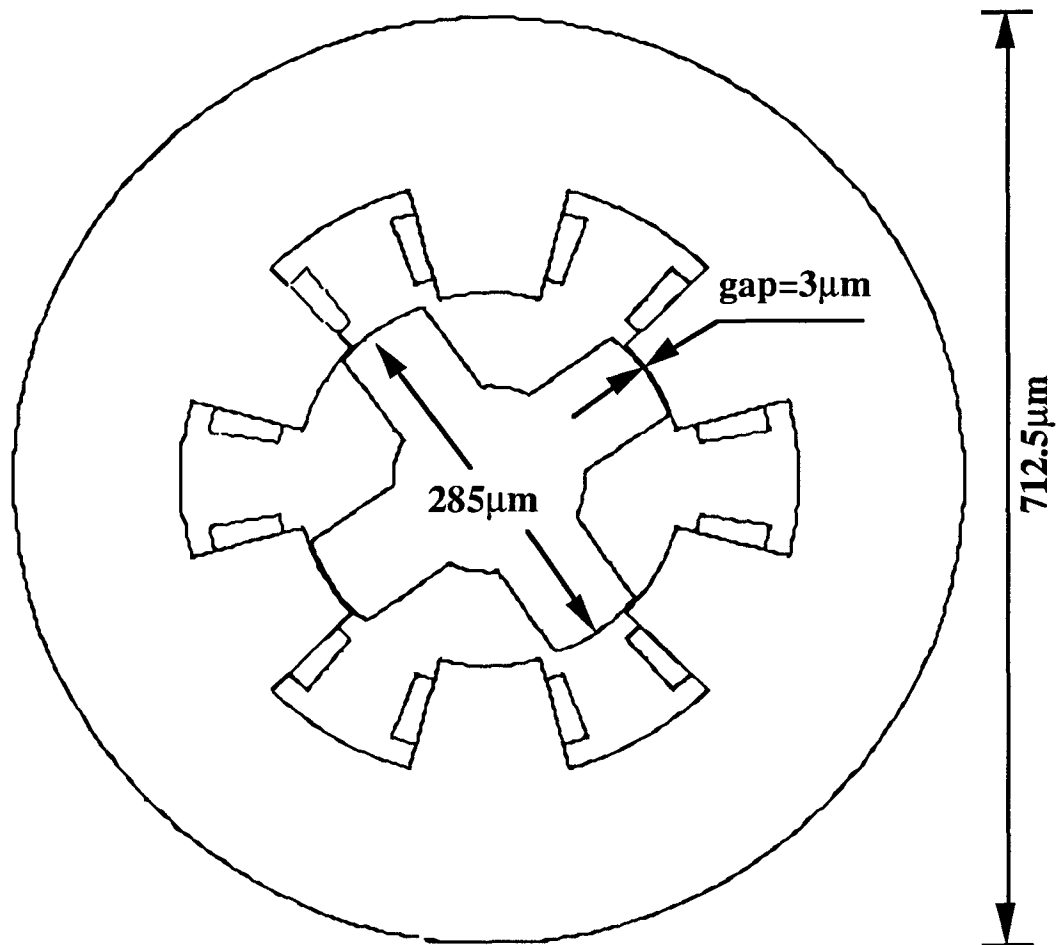


Figure 2.8 YTMM-1 with coils wrapped around stator poles. Drawn to scale using MAXWELL.

The magnetic flux across the whole micromotor when only one stator pole pair is active is shown in Figure 2.9. The orientation is the same as Figure 2.8.

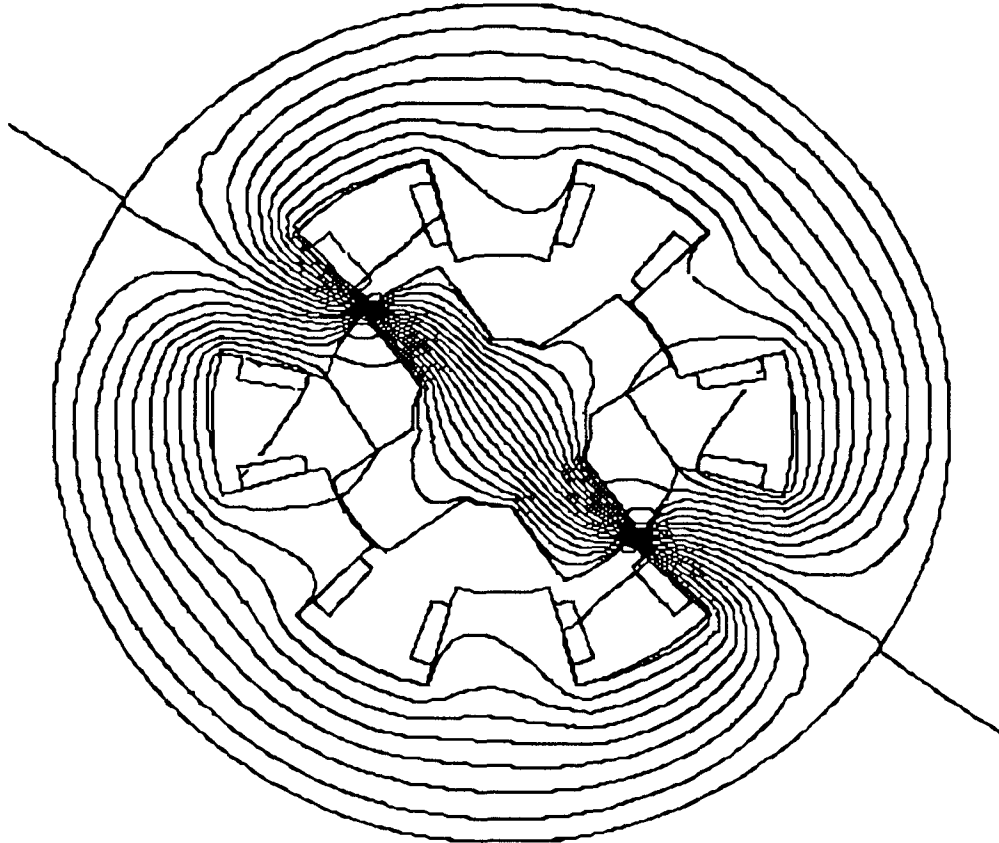


Figure 2.9 Magnetic flux for YTMM-1 with one stator pole pair active ($P_s/P_r=6/4$). Rotor diameter= $285\mu\text{m}$.

The optical photomicrograph of a rotor and stator poles for the YTMM micromotor is shown in Figure 2.10. In this simulation, we use nine turns per stator pole and 0.6A per turn.

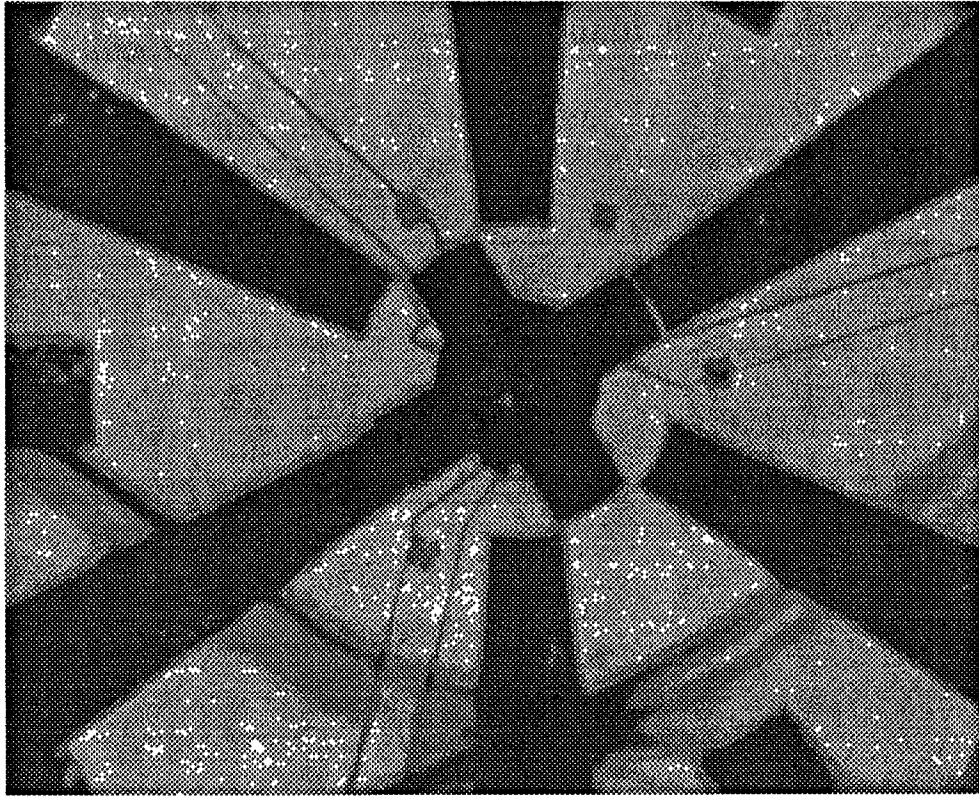
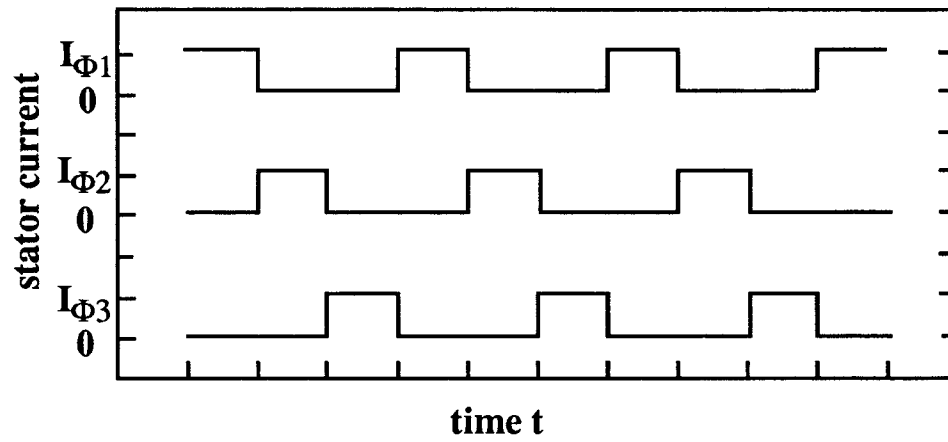
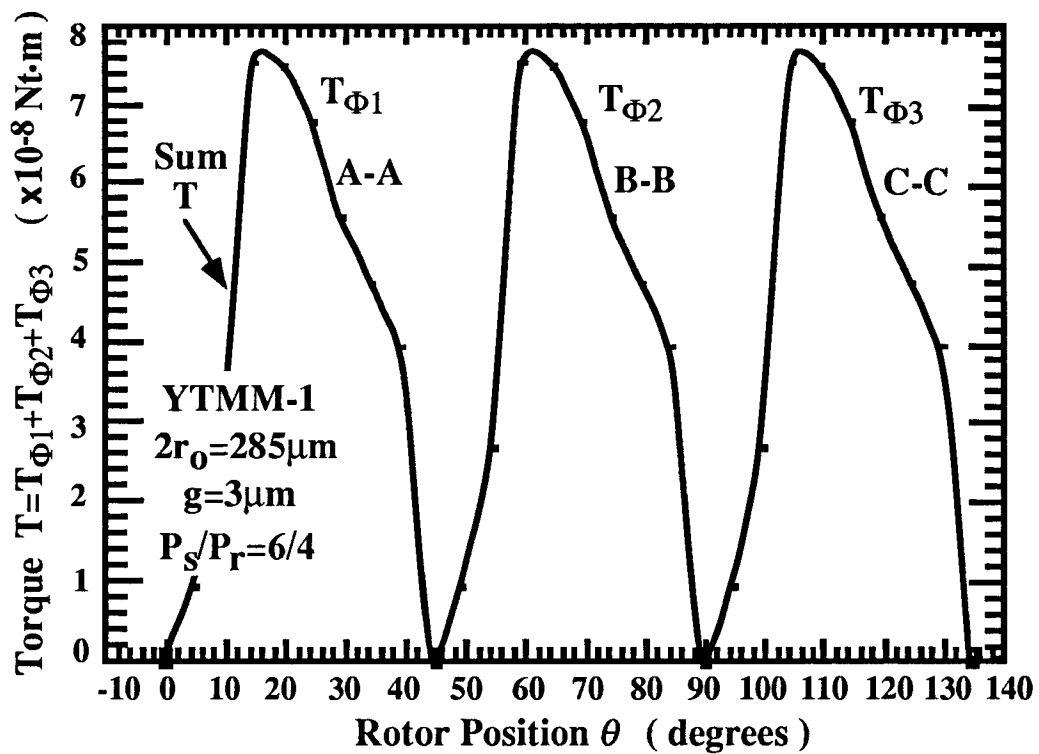


Figure 2.10 Optical photomicrograph of magnetic micromotor [2.1].

The stator current supply with non-overlapping phase sequence is shown in Figure 2.11(a), and the corresponding torque curve is shown in Figure 2.11 (b). The maximum torque is approximately $76\text{nNt}\cdot\text{m}$, and the minimum torque is 0. Note that the torque varies rapidly when the rotor angular position changes.



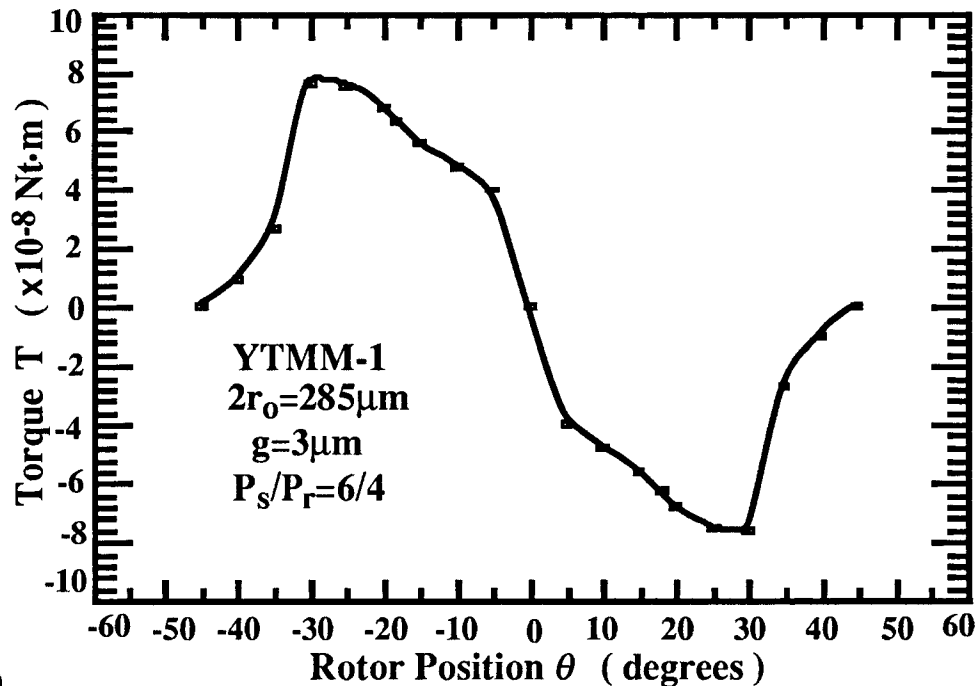
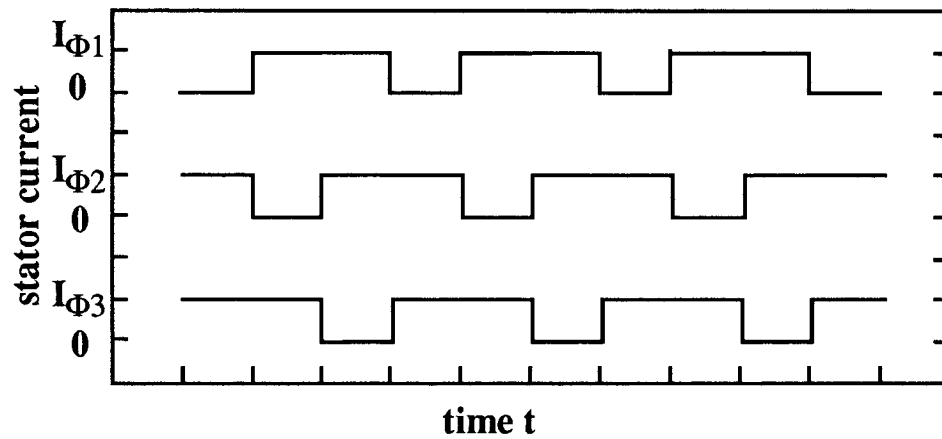
(a)



(b)

Figure 2.11 Torque curve for YTM-1 micromotor with non-overlapping current supply phase sequence: (a) stator current supply with non-overlapping phase sequence; (b) sum torque versus rotor position characteristics.

When overlapping stator currents (as shown in Figure 2.12 (a)) are applied to the stator poles, the torque curve of Figure 2.12 (b) has been calculated for a single phase of excitation. The sum torque curve obtained with three-phase current supply is shown in Figure 2.12 (c). The maximum torque is approximately $76\text{nNt}\cdot\text{m}$, and the minimum torque is approximately $57\text{nNt}\cdot\text{m}$. The angular variation of the sum torque in Figure 2.12 (b) is 20%. Reference [2.4] said the average torque is $20\text{nNt}\cdot\text{m}$.



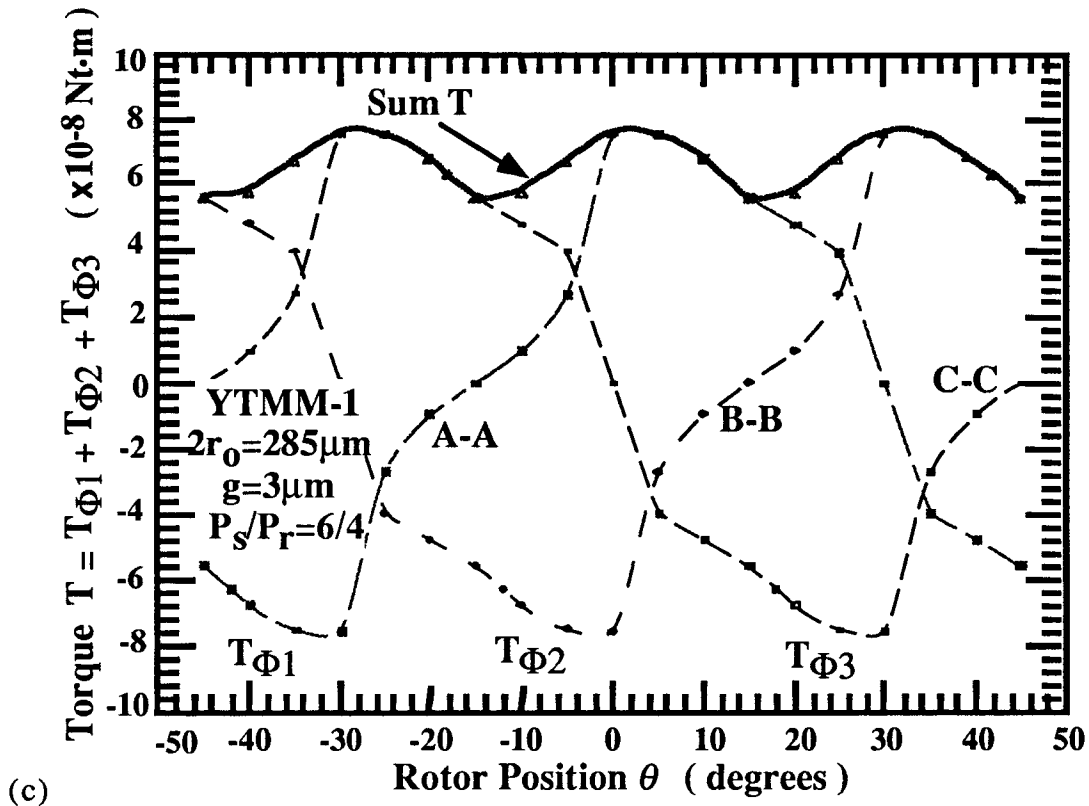


Figure 2.12 Torque curve for YTMM-1 micromotor with overlapping current supply phase sequence: (a) stator current supply with overlapping phase sequence; (b) torque versus rotor position characteristics for a single phase of excitation; (c) sum torque versus rotor position characteristics with three-phase current supply.

The overlapping stator current supply in the example of Figure 2.12 provides an increased sum torque compared to the case of Figure 2.11 with non-overlapping stator current supply. The sum torque curve has less variation. Because the retarding frictional forces are significant in micromotors, the torque minima is very important. If the rotor stops near one of these low drive torque positions, it is more difficult to restart due to the static friction. The small drop in the high torque

region is a characteristic of this design and is due to a reduction in the fringing field area as the rotor aligns to the stator poles.

(2) Yoke-type magnetic micromotor geometry YTMM-2

The second magnetic micromotor geometry selected for simulation is shown in Figure 2.13. This motor has six stator poles and four rotor poles.

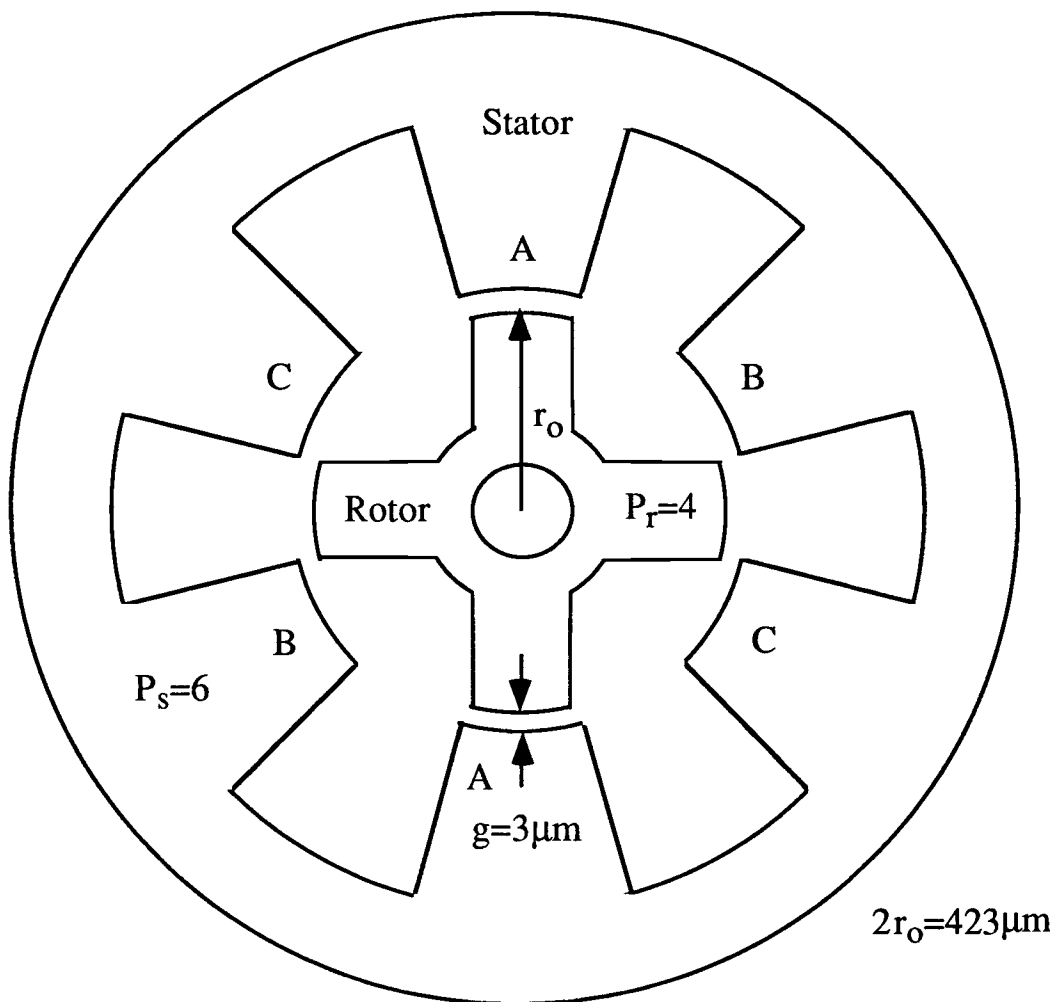
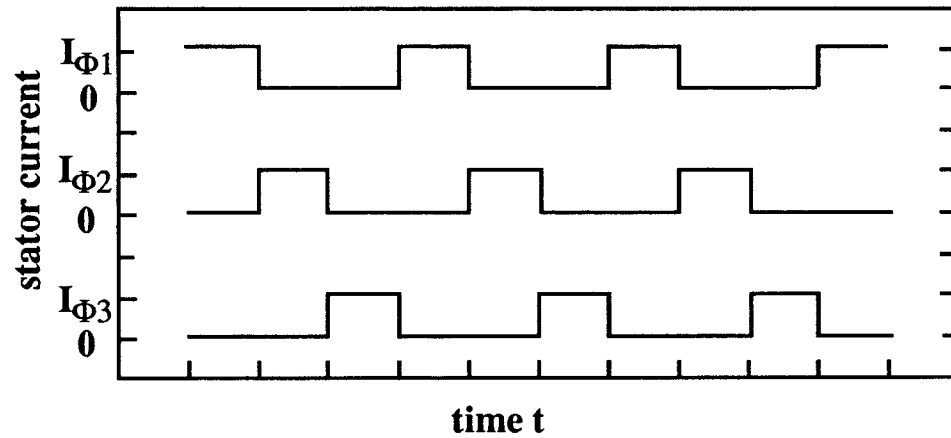


Figure 2.13 Yoke-type magnetic micromotor YTMM-2 -- not to scale.

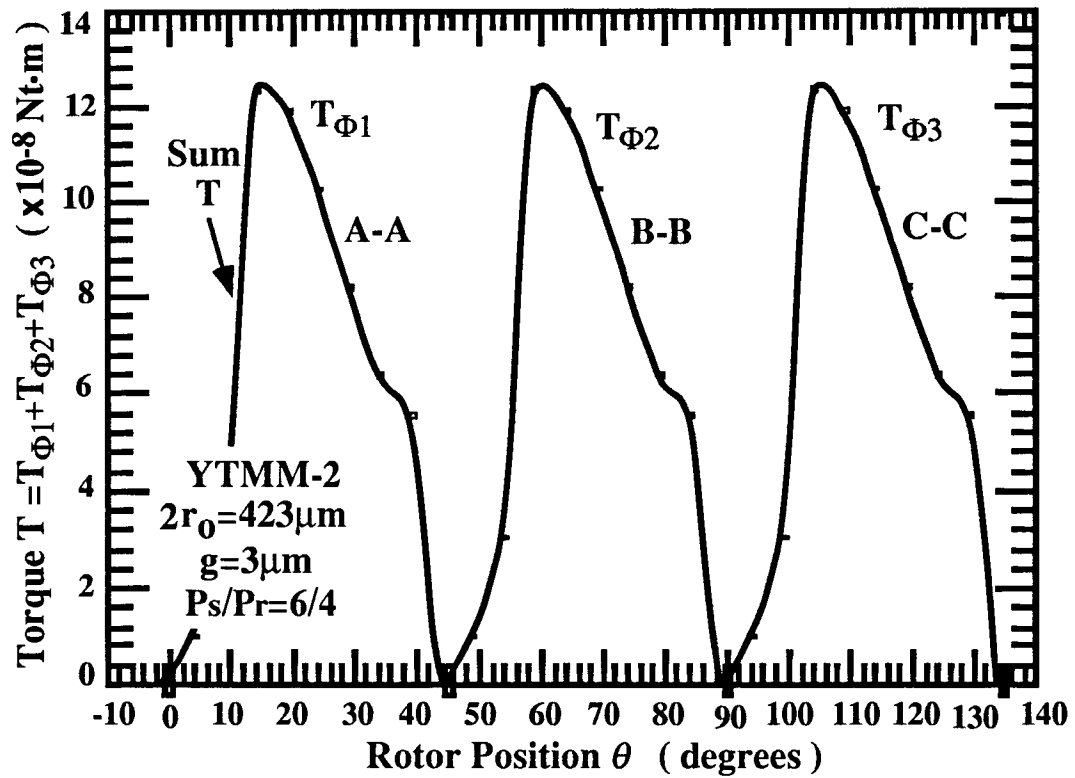
The rotor is $423\mu\text{m}$ in diameter with a bearing post diameter of $108\mu\text{m}$. The rotor poles have a width of 30 degrees, and the stator poles have a width of 30 degrees, too. Lateral rotor-stator air gap is $3\mu\text{m}$. This motor can be driven by a three-phase current. Similar to the simulation of YTMM-1, we use nine turns per stator pole and 0.6A per turn. The currents supplying this micromotor can be non-overlapping or overlapping.

When the stator current supply with non-overlapping phase sequence (as shown in Figure 2.14 (a)), the corresponding sum torque curve is shown in Figure 2.14 (b). The maximum torque is approximately $124\text{nNt}\cdot\text{m}$, and the minimum torque is 0.

When the stator current supply with overlapping phase sequence (as shown in Figure 2.15 (a)), the torque curve of Figure 2.12 (b) has been calculated for a single phase of excitation. The corresponding sum torque curve obtained with three-phase current supply is shown in Figure 2.15 (c). The maximum torque is approximately $124\text{nNt}\cdot\text{m}$, and the minimum torque is approximately $74\text{nNt}\cdot\text{m}$. The angular variation in torque for this configuration is 40%.

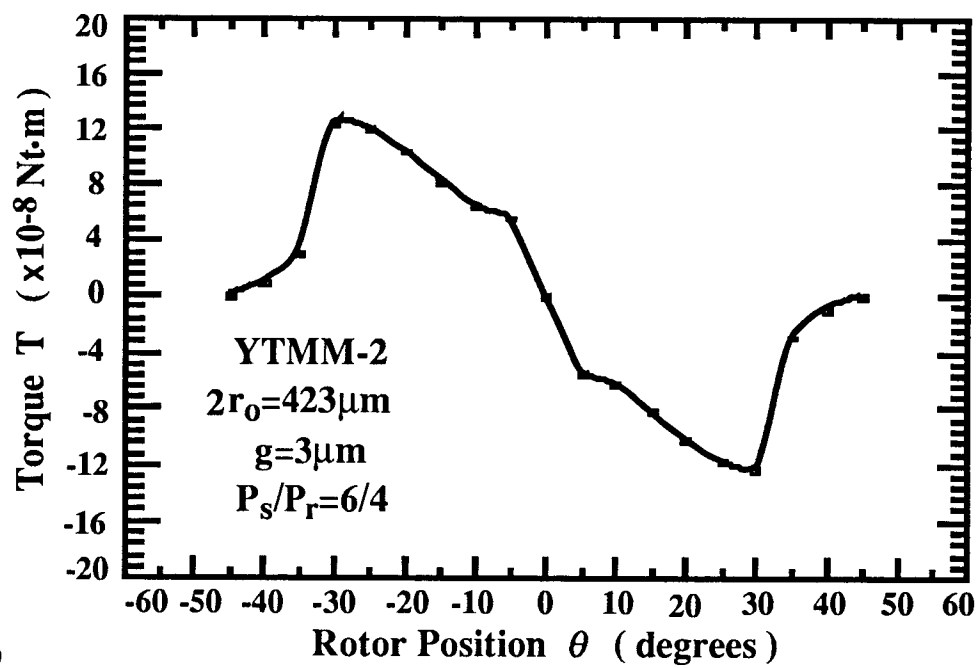
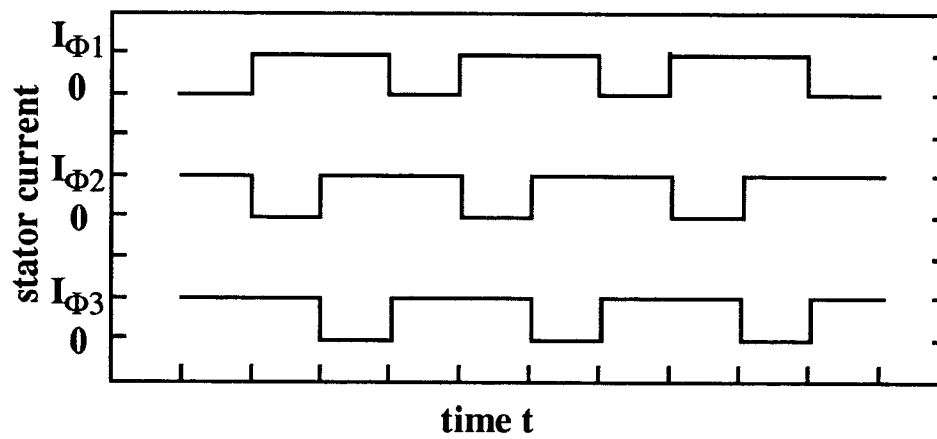


(a)



(b)

Figure 2.14 Torque curve for YTMM-2 micromotor with non-overlapping current supply phase sequence: (a) stator current supply with non-overlapping phase sequence; (b) sum torque versus rotor position characteristics.



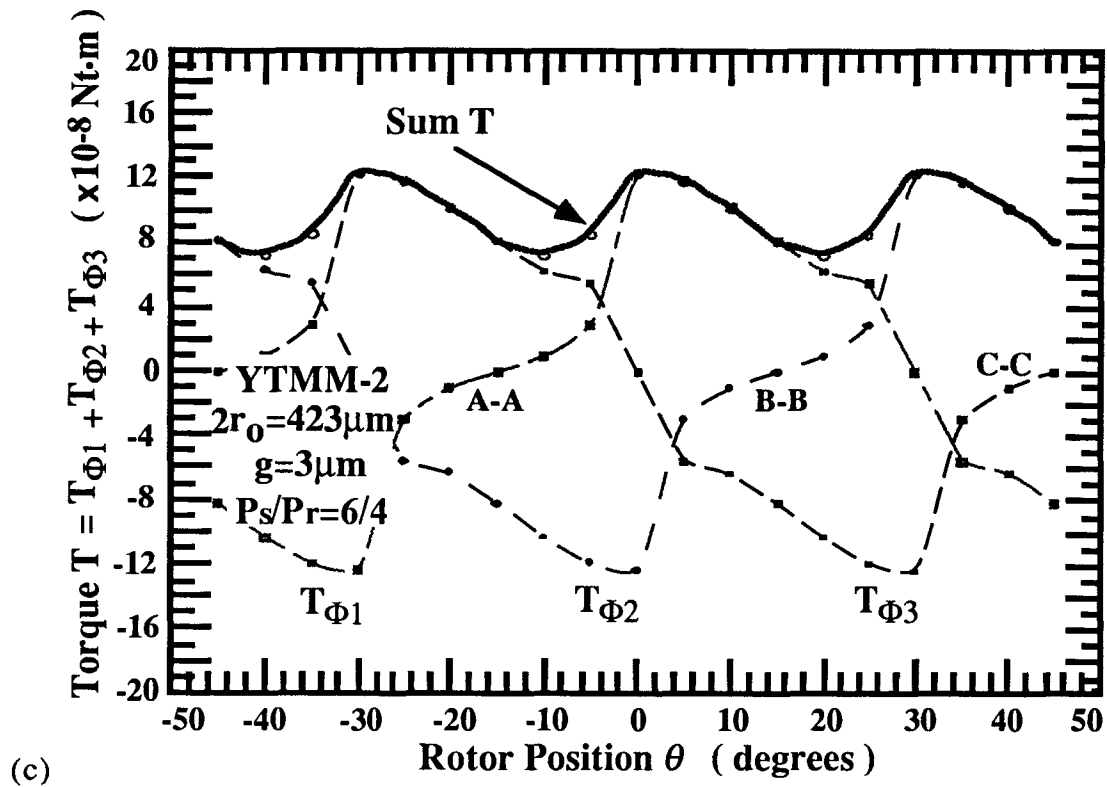


Figure 2.15 Torque curve for YTMM-2 micromotor with overlapping current supply phase sequence: (a) stator current supply with overlapping phase sequence; (b) torque versus rotor position characteristics for a single phase of excitation; (c) sum torque versus rotor position characteristics with three-phase current supply.

The torque curve with overlapping current supply is much smoother and flatter, and the motor average torque is higher for YTMM-2 motor in Figure 2.15 when the same motor is driven by non-overlapping stator current in Figure 2.14.

(3) Yoke-type magnetic micromotor geometry YTMM-3

Geometry for YTMM-3 is shown in Figure 2.16. This motor has 12 stator poles and eight rotor poles. The rotor is $285\mu\text{m}$ in diameter with a

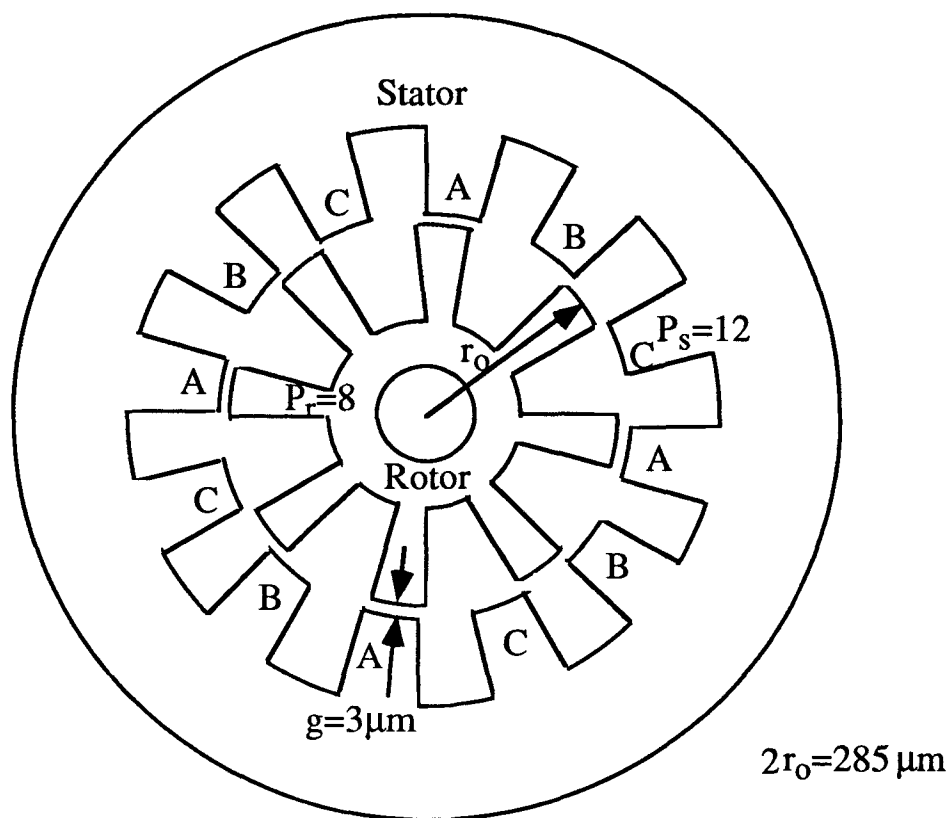


Figure 2.16 Yoke-type magnetic micromotor YTMM-3 -- not to scale.

bearing post diameter of $72\mu\text{m}$. The rotor poles have a width of 15 degrees, and the stator poles have a width of 15 degrees, too. Lateral rotor-stator air gap is $3\mu\text{m}$. This motor can also be driven by a three-phase current. These three-phase currents can be non-overlapping or overlapping. This micromotor with coils wrapped around one stator pole pair is shown in Figure 2.17. The magnetic flux across the entire micromotor when only one stator pole pair active is shown in Figure 2.18. In this simulation, we use nine coil turns per stator pole and 0.6A current per turn. This results in an \mathbf{H} -vector of $5.4\text{A}\cdot\text{turns}$.

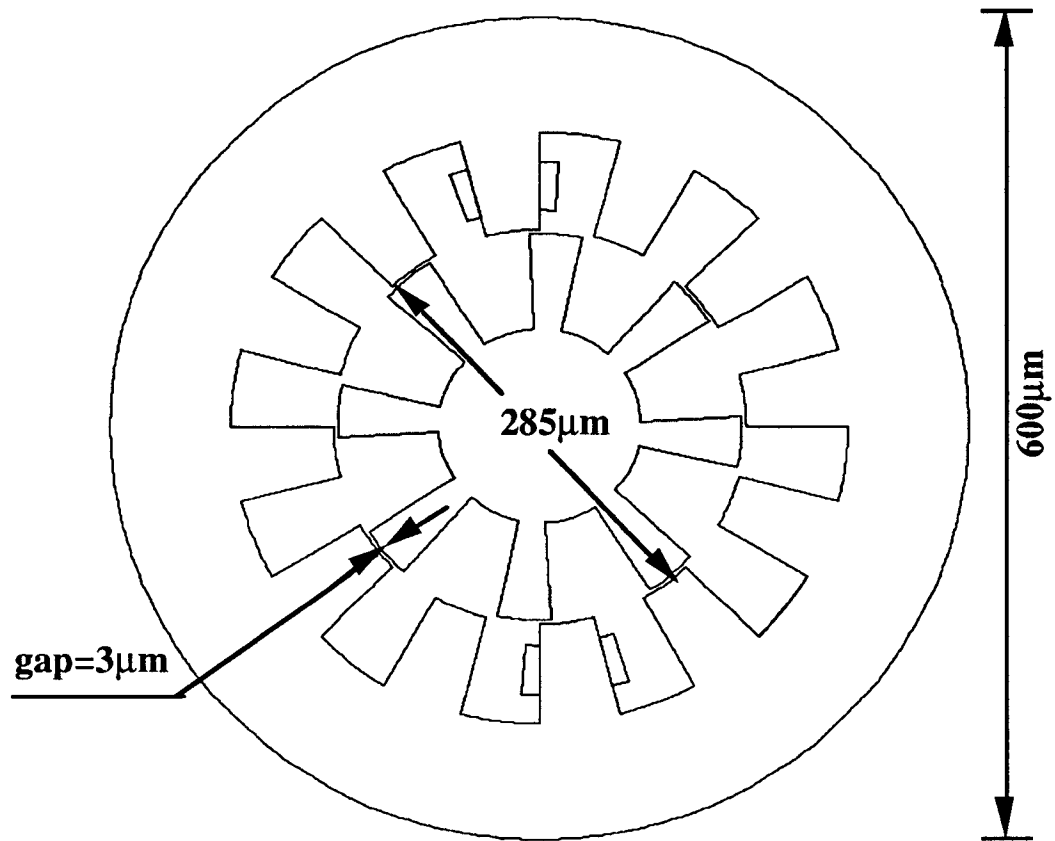


Figure 2.17 The micromotor with coils wrapped around one stator pole pair. Drawn to scale using MAXWELL.

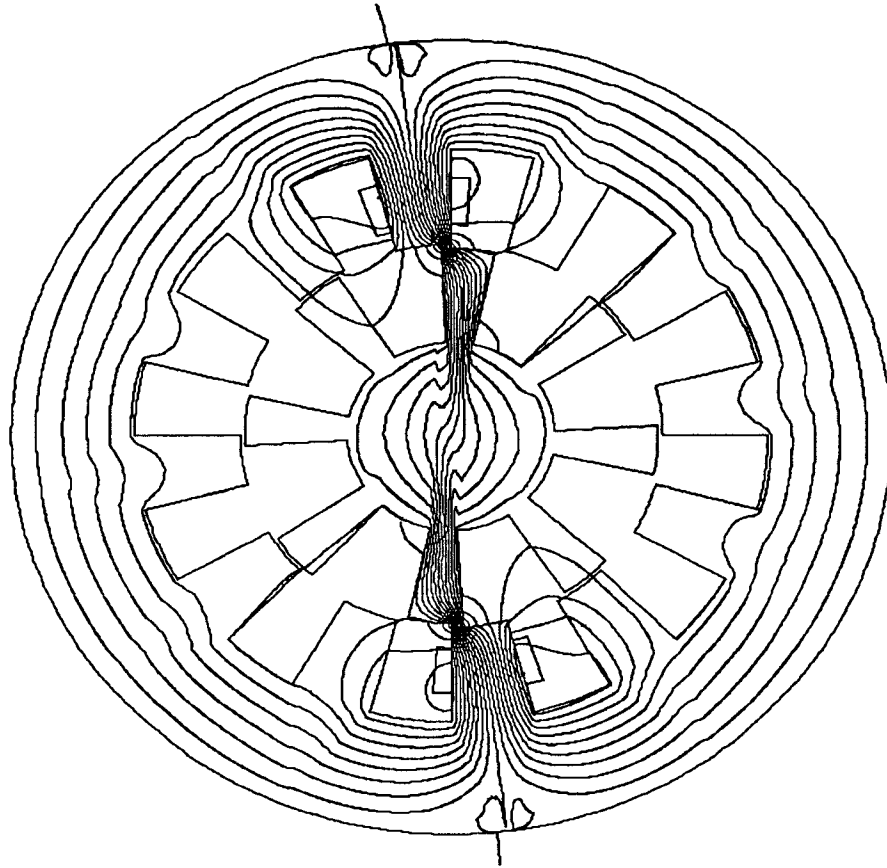
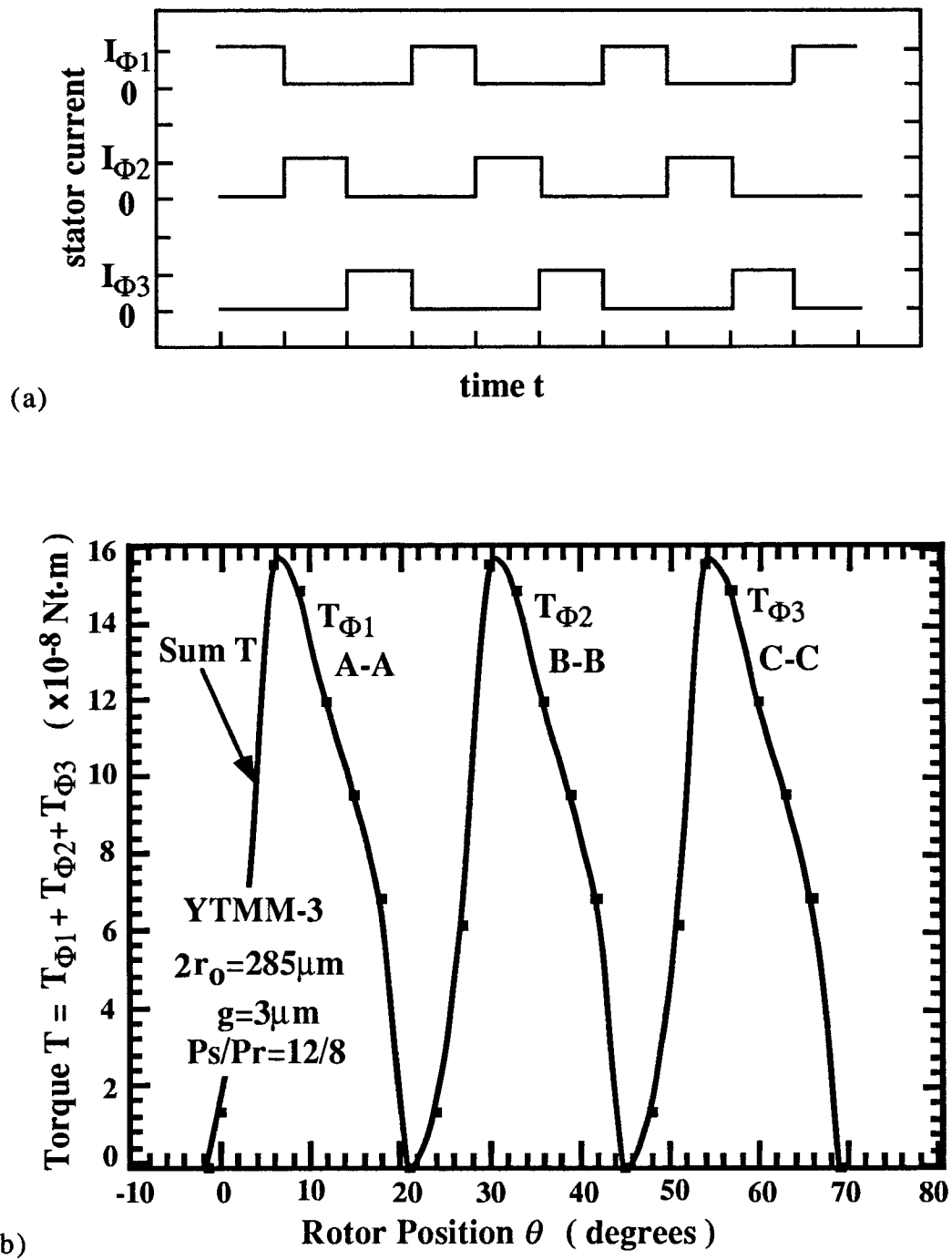
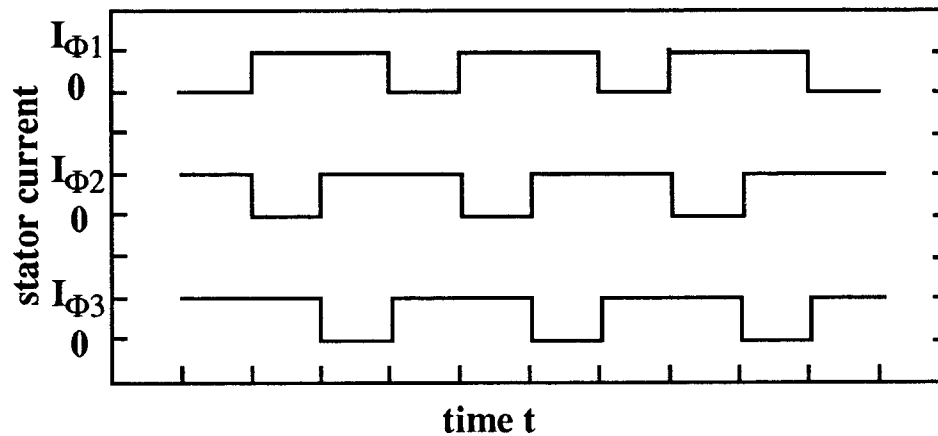


Figure 2.18 The magnetic flux across the entire micromotor when only one stator pole pair active. Rotor diameter = $285\mu\text{m}$.

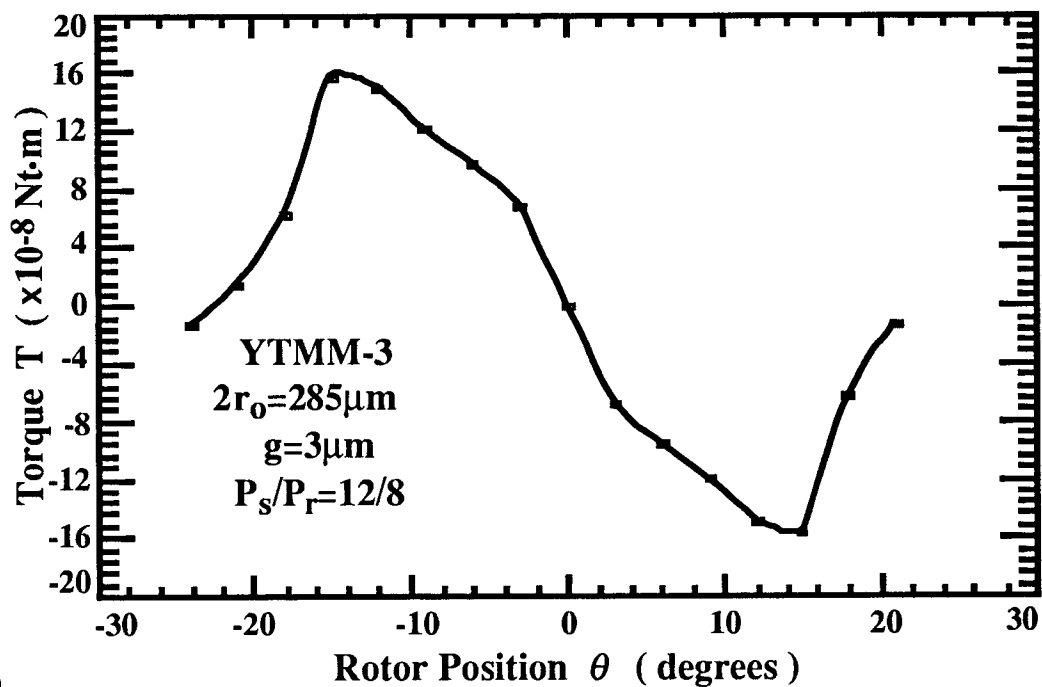
When non-overlapping stator currents (as shown in Figure 2.19 (a)) are applied to the stator poles, the sum torque curve is shown in Figure 2.19 (b). The maximum torque is approximately $158\text{nN}\cdot\text{m}$, and the minimum torque is 0. The torque curve is very peaked.



When overlapping stator currents (as shown in Figure 2.20 (a)) are applied to the stator poles, the torque curve of Figure 2.20 (b) has been calculated for a single phase of excitation. The sum torque curve obtained with three-phase current supply is shown in Figure 2.20 (c).



(a)



(b)

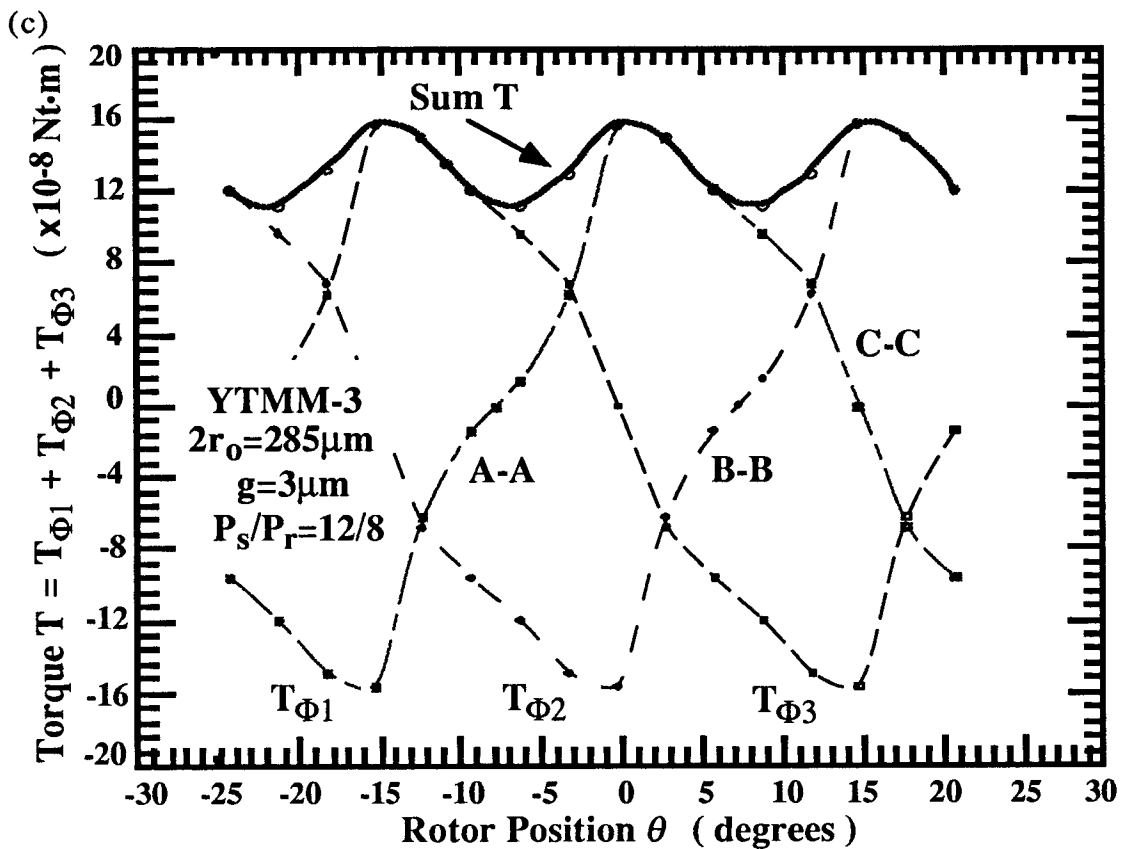


Figure 2.20 Torque curve for YTMM-3 micromotor with overlapping current supply phase sequence: (a) stator current supply with overlapping phase sequence; (b) torque versus rotor position characteristics for a single phase of excitation; (c) sum torque versus rotor position characteristics with three-phase current supply.

The maximum torque is approximately $158 \text{ nNt}\cdot\text{m}$, and the minimum torque is approximately $112 \text{ nNt}\cdot\text{m}$. The angular variation of the torque in Figure 2.20 is 29%.

Compared Figure 2.19 and Figure 2.20, the sum torque curve with overlapping current supply is much smoother and flatter, and the average torque is higher for YTMM-3 motor than the same micromotor is driven by non-overlapping current supply.

(4) Yoke-type magnetic micromotor geometry YTMM-4

The magnetic micromotor geometry selected for simulation is shown in Figure 2.21. This motor has 12 stator poles and eight rotor poles. The rotor is $423\mu\text{m}$ in diameter with a bearing post diameter of $108\mu\text{m}$. The rotor poles have a width of 15 degrees, and the stator poles have a width of 15 degrees. The lateral rotor-stator air gap is $4.5\mu\text{m}$. This motor is driven by a three-phase current in this example for torque calculations. Like the simulation of YTMM-3, we use nine turns per stator pole and 0.6A per turn. The current supply can be non-overlapping or overlapping.

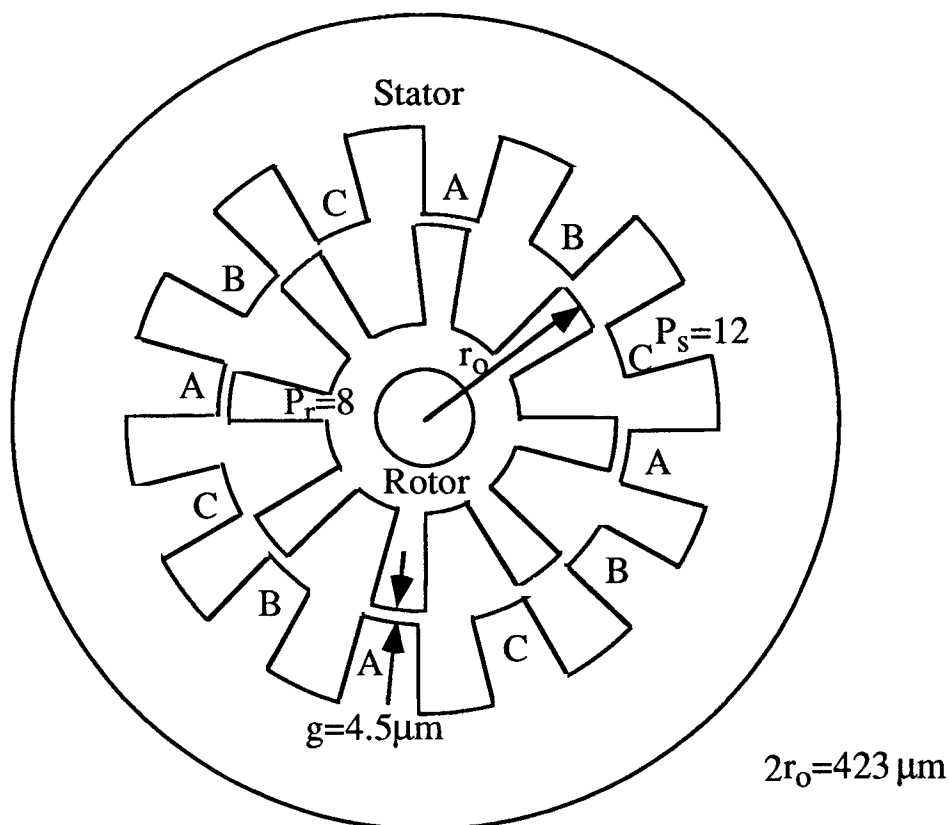
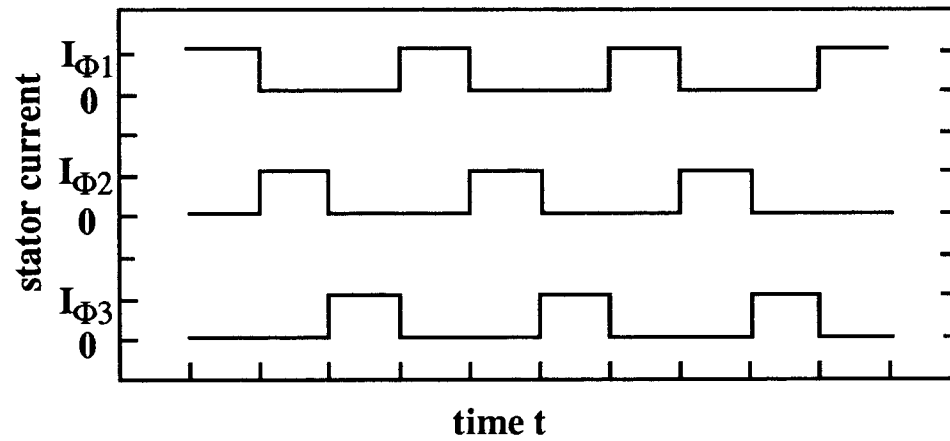
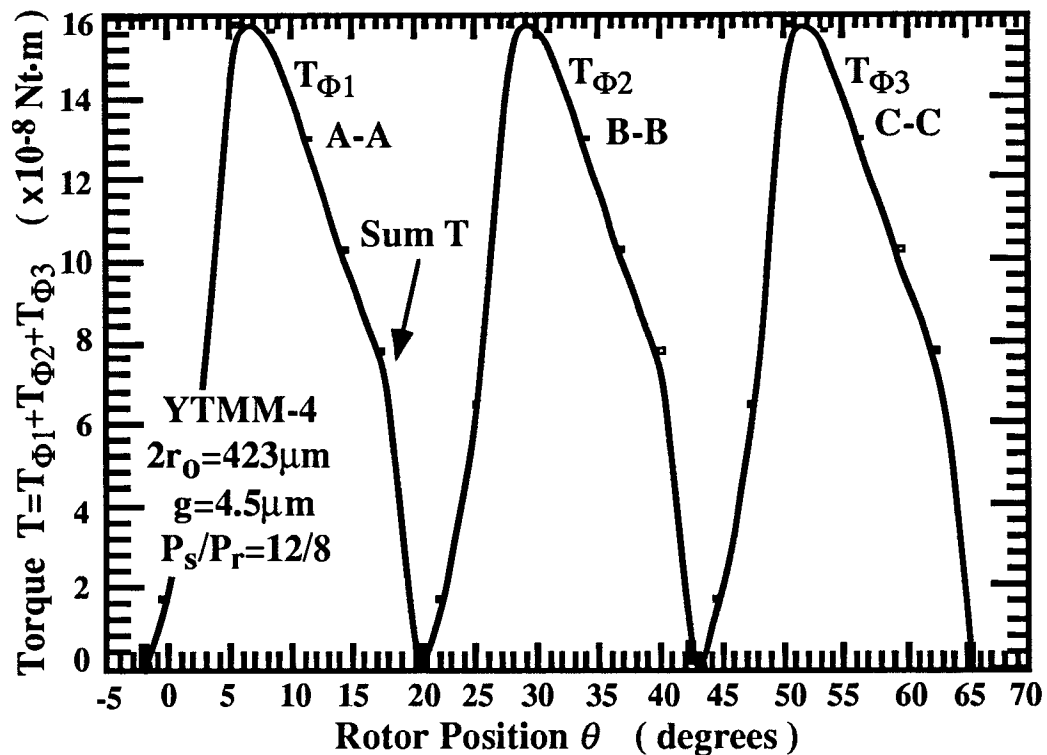


Figure 2.21 Yoke-type magnetic micromotor YTMM-4 -- not to scale.

When non-overlapping stator currents (as shown in Figure 2.22 (a))



(a)

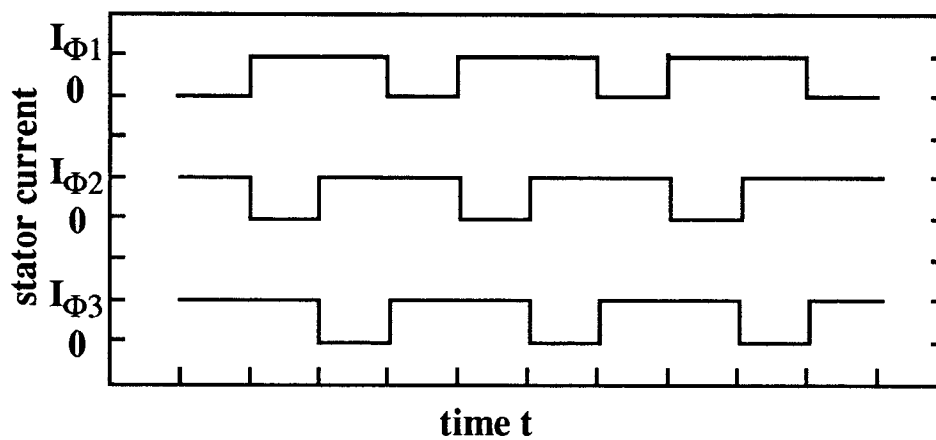


(b)

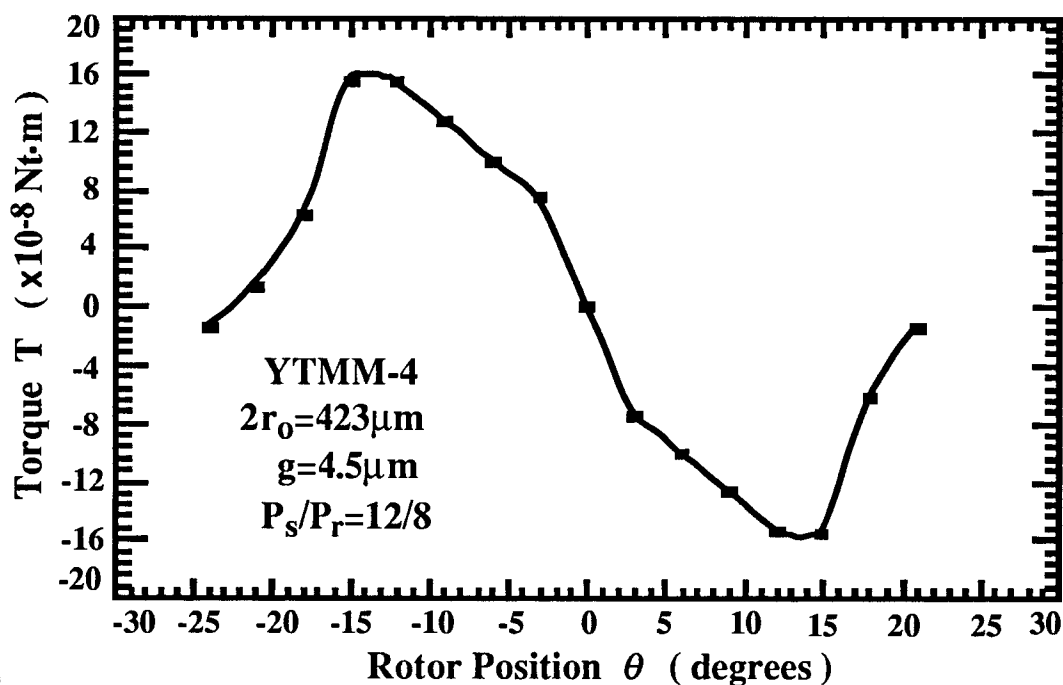
Figure 2.22 Torque curve for YTMM-4 micromotor with non-overlapping current supply phase sequence: (a) stator current supply with non-overlapping phase sequence; (b) sum torque versus rotor position characteristics.

are applied to the stator poles, the sum torque curve is shown in Figure 2.22 (b). The maximum torque is approximately $156 \text{ nNt}\cdot\text{m}$, and the minimum torque is 0. The torque varies rapidly when the rotor position changes.

When overlapping stator currents (as shown in Figure 2.23 (a)) are



(a)



(b)

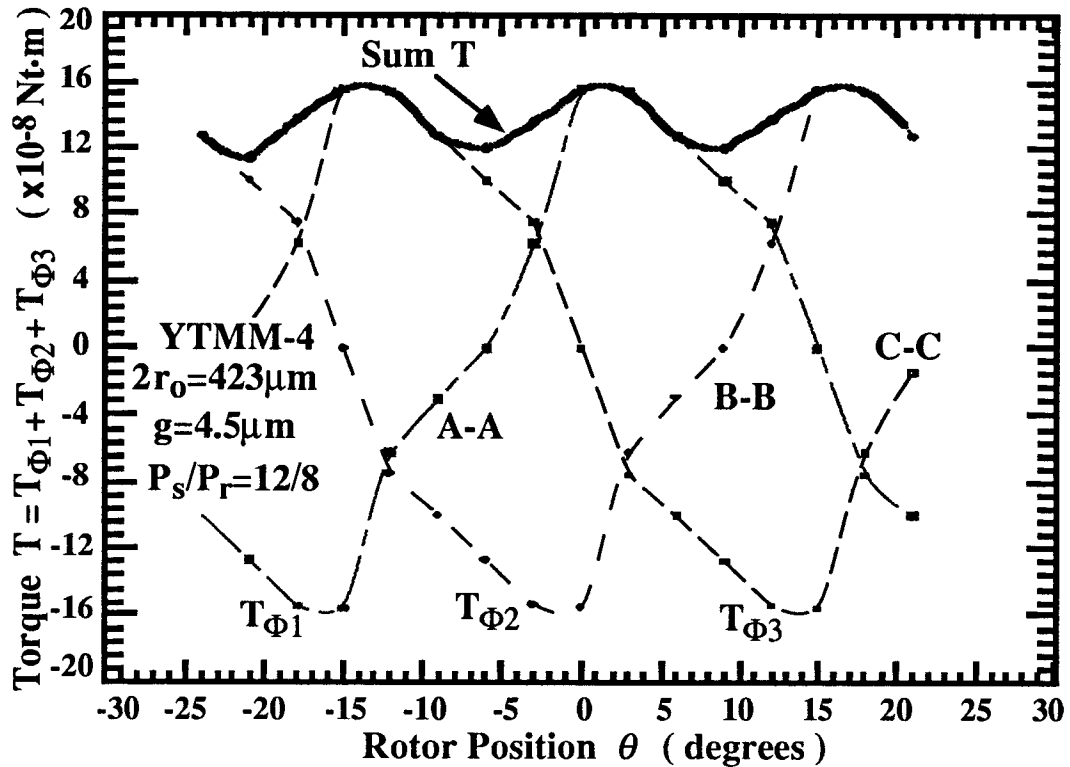


Figure 2.23 Torque curve for YTMM-4 micromotor with overlapping current supply phase sequence: (a) stator current supply with overlapping phase sequence; (b) torque versus rotor position characteristics for a single phase of excitation; (c) sum torque versus rotor position characteristics with three-phase current supply.

applied to the stator poles, the torque curve of Figure 2.23 (b) has been calculated for a single phase of excitation. The sum torque curve obtained with three-phase current supply is shown in Figure 2.23 (c). The maximum torque is approximately $156\text{nNt}\cdot\text{m}$, and the minimum torque is approximately $116\text{nNt}\cdot\text{m}$. The angular variation of the sum torque in Figure in Figure 2.23 is 25%.

The sum torque curve with overlapping current supply is much smoother and flatter, and the average torque is higher for YTMM-4

motor (in Figure 2.23) than the same micromotor is driven by non-overlapping current supply.

(5) Yoke-type magnetic micromotor geometry YTMM-5

The magnetic micromotor geometry selected for simulation is shown in Figure 2.24. The motor has 12 stator poles and eight rotor poles. The rotor is $423\mu\text{m}$ in diameter with a bearing post diameter of $108\mu\text{m}$. The rotor poles have a width of 15 degrees, and the stator poles also have a width of 15 degrees. The lateral rotor-stator air gap is $3\mu\text{m}$. This motor can be driven by a three-phase current. Similar to the simulation of YTMM-3, we use nine turns per stator pole and 0.6A per turn. The current can be non-overlapping or overlapping.

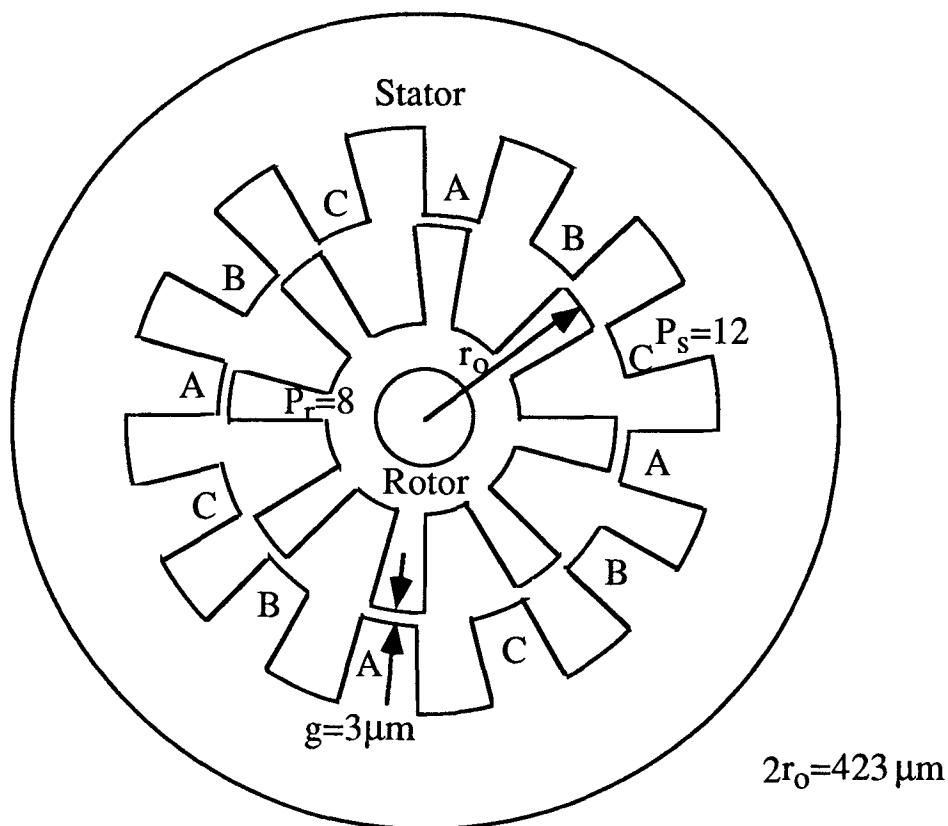
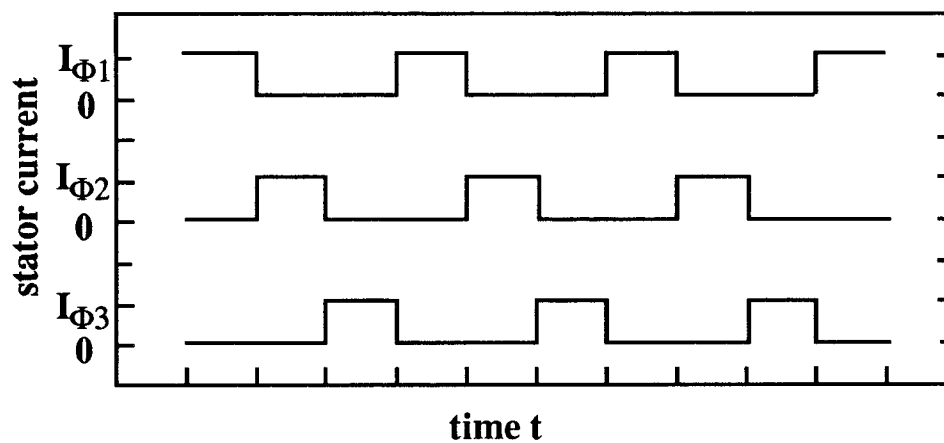
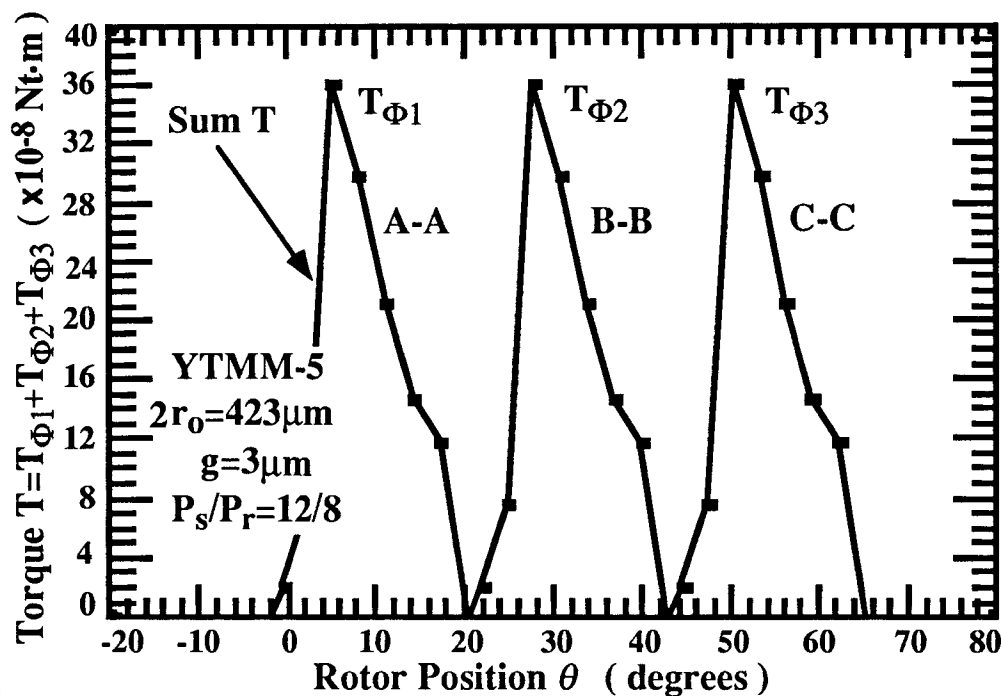


Figure 2.24 Yoke-type magnetic micromotor YTMM-5 -- not to scale.

When overlapping stator currents (as shown in Figure 2.25 (a)) are



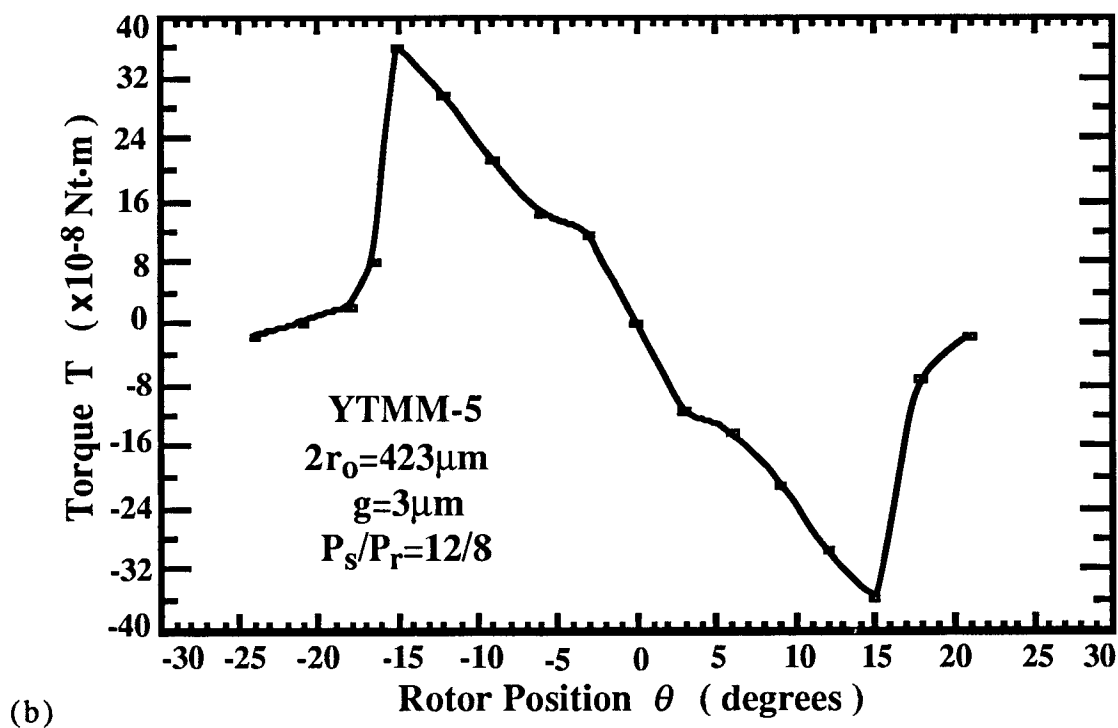
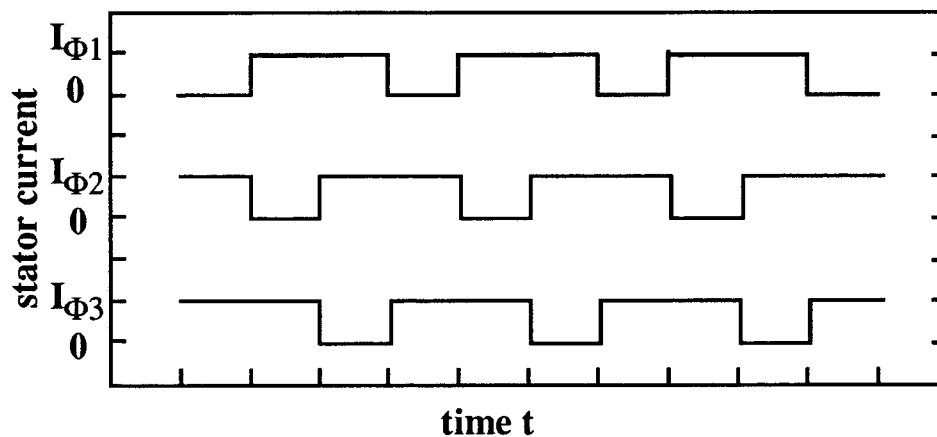
(a)



(b)

Figure 2.25 Torque curve for YTMM-5 micromotor with non-overlapping current supply phase sequence: (a) stator current supply with non-overlapping phase sequence; (b) sum torque versus rotor position characteristics.

applied to the stator poles, the torque curve when dc stator current supplying one stator pole pair (one phase) is shown in Figure 2.25 (b). The sum torque curve with multiphase current supply is shown in Figure 2.25 (c). The maximum torque in this case is approximately $360\text{nN}\cdot\text{m}$, and the minimum torque is 0. The torque varies rapidly when the rotor position changes.



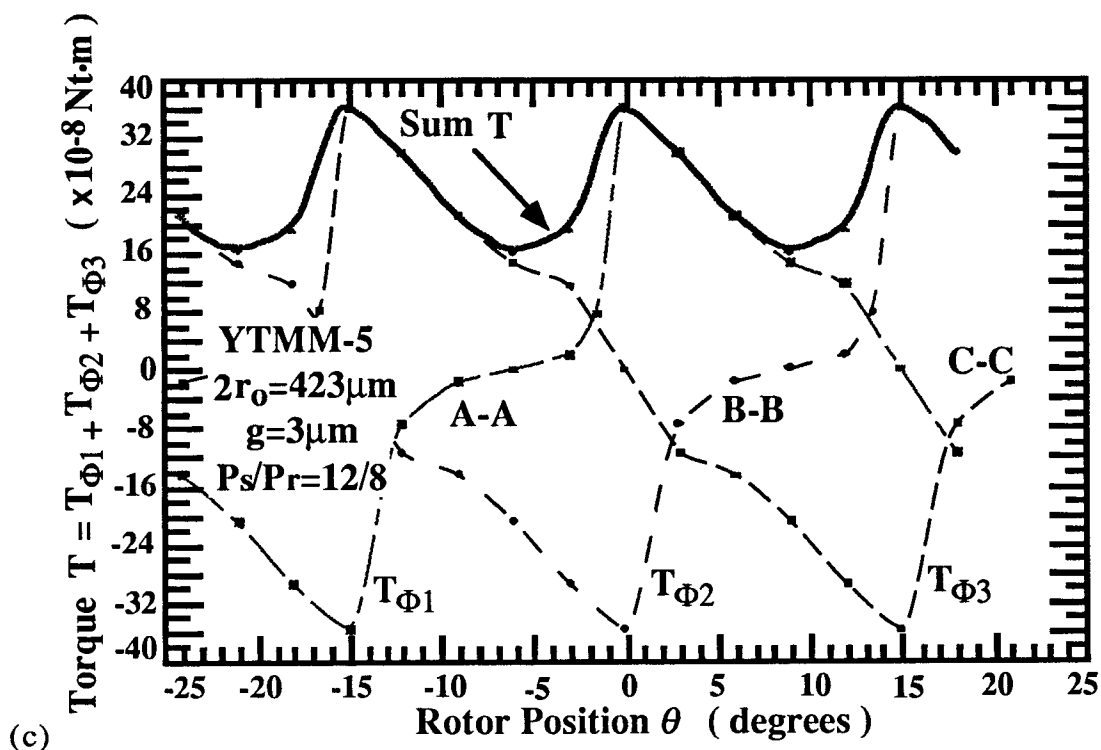


Figure 2.26 Torque curve for YTMM-5 micromotor with overlapping current supply phase sequence: (a) stator current supply with overlapping phase sequence; (b) torque versus rotor position characteristics for a single phase of excitation; (c) sum torque versus rotor position characteristics with three-phase current supply.

When overlapping stator currents (as shown in Figure 2.26 (a)) are applied to the stator poles, the torque curve of Figure 2.26 (b) has been calculated for a single phase of excitation. The sum torque curve obtained with three-phase current supply is shown in Figure 2.26 (c). The maximum torque in this case is approximately $360 \text{ nNt}\cdot\text{m}$, and the minimum torque is approximately $160 \text{ nNt}\cdot\text{m}$. The sum torque curve is rather flat. The angular variation of the torque in Figure 2.26 is 55%.

The sum torque curve with overlapping current supply is much flatter and smoother, and the average torque is higher for YTMM-5 motor (in Figure 2.26 (c)) than the same micromotor is driven by non-overlapping current supply.

2.4 Variation of Torque with Important Design Parameters

2.4.1 Variation of Torque with Relative Permeability

The relative permeability represents the magnetizable characteristic of the material. When the material of the rotor and stator is changed, the relative permeability changes, the magnitude of the induced magnetic field changes, and these cause the torque of the rotor changes. The maximum torque versus the relative permeability curve for YTMM-2 is shown in Figure 2.27. Note from this curve, the torque increases when the relative permeability increases. When the relative permeability μ_r is small, the torque increases linearly with the increasing of μ_r . At higher permeability μ_r values, the reluctance of the magnetic path becomes significant and the torque -- permeability curve in Figure 2.27 is seen to saturated. When the relative permeability μ_r is big, the torque will just change a little with it. When the relative permeability increases to a big enough value, the torque will reach a steady value, and this can be seen from Figure 2.27.

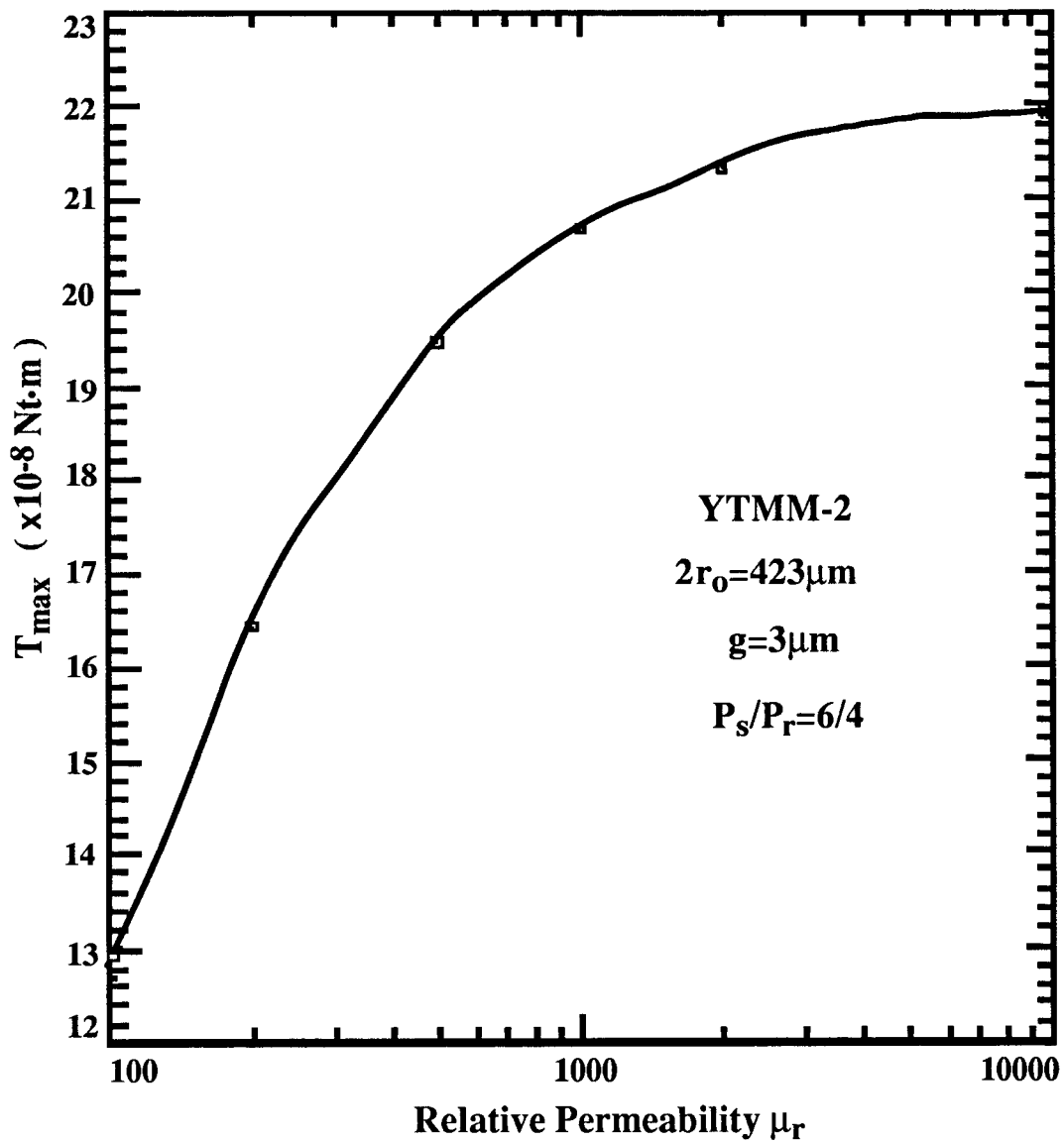


Figure 2.27 Maximum torque T_{\max} versus relative permeability μ_r .

2.4.2 Variation of Torque with Air Gap

The dimension of the air gap is also a very important parameter in this simulation. The force on the rotor is caused by the gradient of the energy stored in the air gap. When the dimension of the air gap

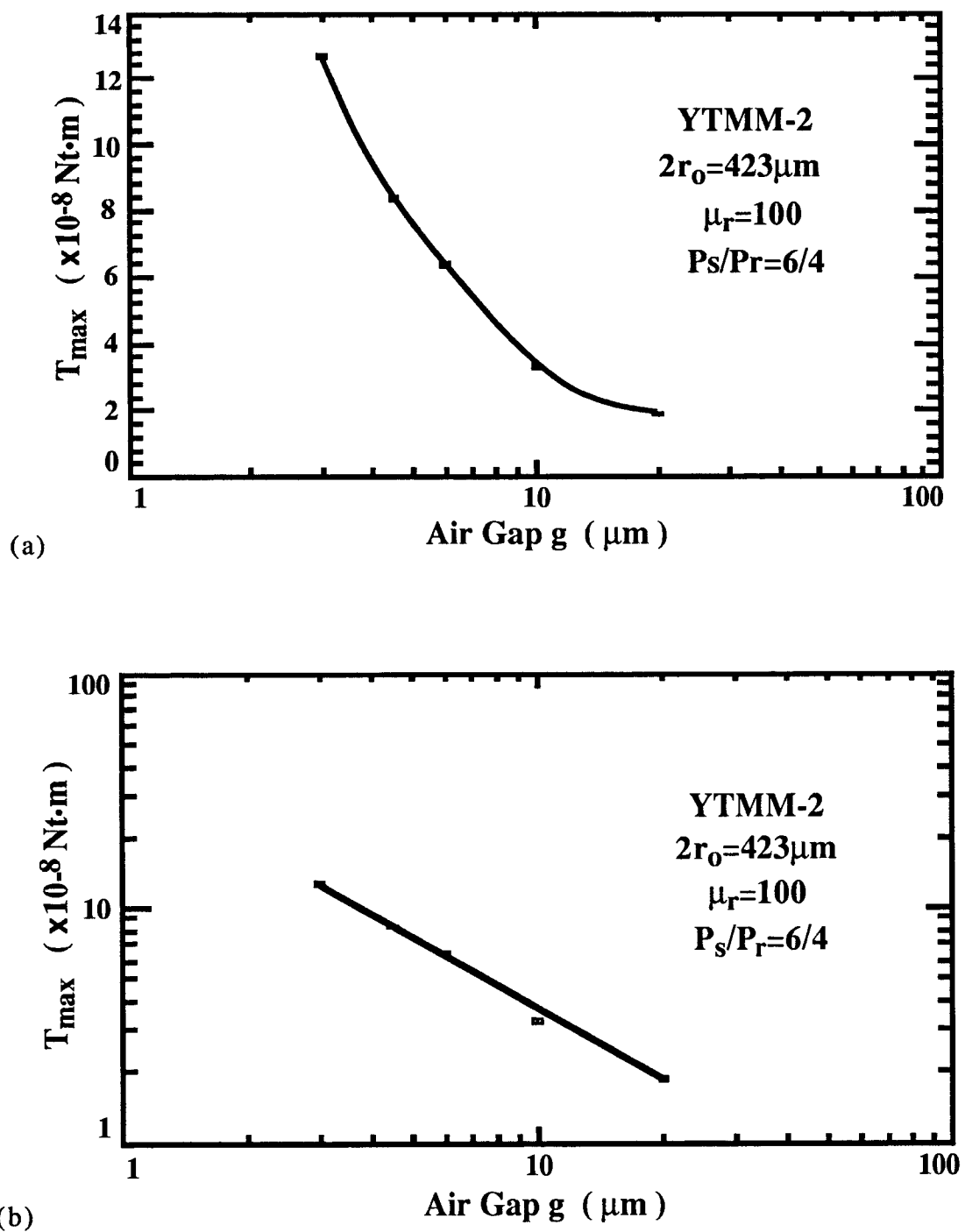


Figure 2.28 Maximum torque T_{\max} versus the air gap g : (a) semi-log maximum torque curve; (b) log maximum torque curve.

changes, the force on the rotor changes, and then the torque change. The maximum torque versus the air gap curve for YTMM-2 is shown in Figure 2.28. Figure 2.28 (a) is a semi-log maximum torque curve, and Figure 2.28 (b) is a log maximum torque curve. Note from the curve, the torque decreases when the air gap increases. When the air gap reaches a big enough value, the torque will be zero. This can be clearly seen from Figure 2.28 (b).

2.5 Summary of Modeling Results

In section 2.3, simulations for five different magnetic micromotor designs have been made. From the results, we can see there are many differences among them.

(1) Torque difference between non-overlapping and overlapping stator current cases

For the same micromotor geometry, the maximum torque is the same when the micromotor is driven by non-overlapping or overlapping stator current. The micromotor driven by overlapping stator current increases the minimum torque and the average sum torque. The sum torque curve is more constant for the case of overlapping stator current supplying.

(2) Torque difference between two rotor diameters

When the rotor diameter increases, the torque increases approximately linearly with it for the model used here.

For the micromotor with six stator poles and four rotor poles, the torque for 423 μ m rotor diameter motor (YTMM-2) is approximately 1.6 times the torque for 285 μ m rotor diameter motor (YTMM-1).

For the micromotor with 12 stator poles and six rotor poles, the torque for 423 μ m rotor diameter motor (YTMM-5) is approximately 2.3 times the torque for 285 μ m rotor diameter motor (YTMM-3).

It can be seen that the torque ratio is greater than the rotor diameter ratio. The torque increases when the rotor diameter increases, but not linear.

(3) Torque changes when the number of rotor and stator poles changes

When the number of rotor and stator changes, the torque changes with it.

For the micromotor with 285 μ m rotor diameter, the torque for the stator and rotor pole combination of 12/8 (YTMM-3) is approximately 2.1 times of the torque for the stator and rotor pole combination of 6/4 (YTMM-1).

For the micromotor with 423 μ m rotor diameter, the torque for the stator and rotor pole combination of 12/8 (YTMM-5) is approximately 2.9 times of the torque for the stator and rotor pole combination of 6/4 (YTMM-2).

So we can see that the ratio of the torque change is greater than the ratio of the poles, and the torque ratio increases when the number of stator and rotor poles changes.

(4) Torque changes with gap

When the gap changes, the magnetic field in the gap changes and the magnetic flux density changes. As an effect, the torque changes.

For the micromotor with 12 stator poles and eight rotor poles, 423 μm rotor diameter, the torque for 3 μm air gap (YTMM-5) is approximately 2.3 times of the torque for the micromotor with 4.5 μm (YTMM-4).

As the gap increases, the torque decreases very fast.

(5) Angular fluctuation of the sum torque curve when the micromotor is driven by overlapping stator current

In YTMM-1, the angular variation of the sum torque is 20%. The angular variation of sum torque is 40% in YTMM-2, 29% in YTMM-3, 25% in YTMM-4, 55% in YTMM-5. We can see that the sum torque curve of YTMM-1 has the minimum fluctuation, and the sum torque curve of YTMM-5 has the maximum fluctuation. The fluctuation of the sum torque curve increases when the ratio of the rotor diameter and the air gap increases.

2.6 References

- [2.1] H. Guckel and K. J. Skrobis, "A first functional current excited planar rotational magnetic micromotor", Fort Lauderdale, Florida, February, 1993. (IEEE Catalog Number 93DH3265-6).
- [2.2] T. R. Christenson, H. Guckel, K. J. Skrobis, J. Klein, "Preliminary results for an integrated planar microdynamometer", in Technical Digest, Solid-State Sensor and Actuator Workshop, Jun 1992.

[2.3] E. W. Becker, W. Ehrfeld, P. Hagmann, A. Maner, D. Munchmeyer, "Fabrication of microstructures with high aspect ratios and great structural heights by synchrotron radiation lithography, galvanoformung, and plastic moulding (LIGA Process)", *Microelectronic Engineering* 4, 1986.

[2.4] H. Guckel, Private communication, March, 1993.

CHAPTER 3

ANALYSIS OF YOKELESS VARIABLE RELUCTANCE MAGNETIC MICROMOTOR (YSMM)

3.1 Previous Research

In the "conventional" variable reluctance magnetic motor shown in Figure 2.1, there is a magnetic path formed through the magnetic yoke frame. It works well for full scale size "conventional" motors because the reluctance of the yoke is very small. In micromachines, it will be quite different. The micromachined magnetic circuit usually has a high magnetic reluctance due to a high achievable permeability of the magnetic core from processing limitation. In the micromagnetic actuators review here, the reluctance of the core and air gap can be comparable. It is very important to reduce the core reluctance in the micromachined magnetic circuit. There are two ways to do this. One way is to increase the permeability of the core. Another way is to modify the geometry of the core. It is not easy to greatly increase the permeability, but it is easier to modify the geometry. The major geometric factors that affect the reluctance in a magnetic core are the magnetic core area and length and thickness. Since the magnetic core area is limited by planar geometric constraints, one of the best design strategies to reduce the magnetic reluctance is to shorten the length of the magnetic core. Since the long magnetic path through the yoke adds significantly to the core reluctance, this motivation to minimize core reluctance makes it desirable to modify

the standard variable reluctance motor design. A schematic diagram of the modified magnetic micromotor design which does reduce the magnetic path length is shown in Figure 3.1. The micromotor configuration of Figure 3.1 is defined as Yokeless Magnetic Micromotor (YSMM). The wound poles of all phases are arranged in pairs of opposite polarity to achieve adjacent pole paths of short lengths. The stator poles are positioned to greatly shorten the magnetic flux path and to provide an isolated magnetic core for the flux path of each phase. This isolated magnetic circuit reduces both 50% of the core reluctance and 40% of the core loss compared with a yoke-type configuration (Figure 2.1). In addition, it is possible to wind coils on the outside of the stator poles to increase the number of current turns that can be achieved and allow the bonding pads to be on the periphery of the motor [3.1].

3.2 Structures and Processes

3.2.1 Structures

In realizing a magnetic-based micromotor, hybrid techniques have been used to either place permanent magnet components onto integrated planar coils [3.2] or to introduce external magnetic fields onto integrated high-permeability moving parts [3.3]. It is very difficult to fabricate three dimensional "wrapped" coils by using an integrated planar fabrication process. A new planar integrated meander inductive component has been proposed and demonstrated [3.4] that multilevel

magnetic cores can be "wrapped" around planar meander conductors. It can interchange the roles of the conductor wire and magnetic core in a conventional inductor. A schematic drawing of a section of the integrated toroidal-meander type inductor is shown in Figure 3.2.

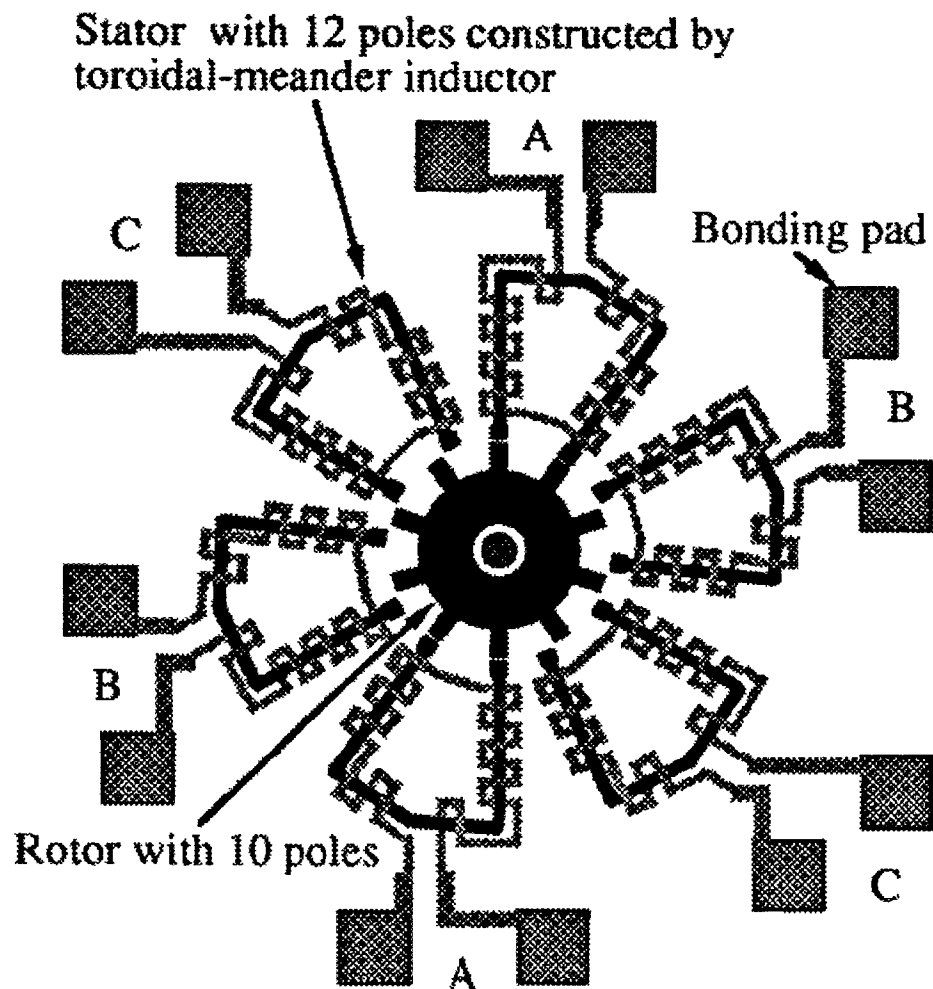


Figure 3.1 Schematic diagram of modified planar variable reluctance magnetic motor. The structure consists of 12 stator poles and 10 rotor poles in three-phase [3.1].

This structure can guide magnetic flux confined in an integrated magnetic core to the locations where magnetic actuation or sensing takes place. By using a movable cantilever beam [3.5], a magnetic microactuator can be fabricated in a fully integrated way. A new functional, electrically excited planar variable reluctance magnetic micromotor can be fabricated on a silicon wafer using this component as the basis for a micromotor stator to generate magnetic flux. This modified magnetic micromotor has almost the same operating principle to the "conventional" magnetic micromotor [3.1].

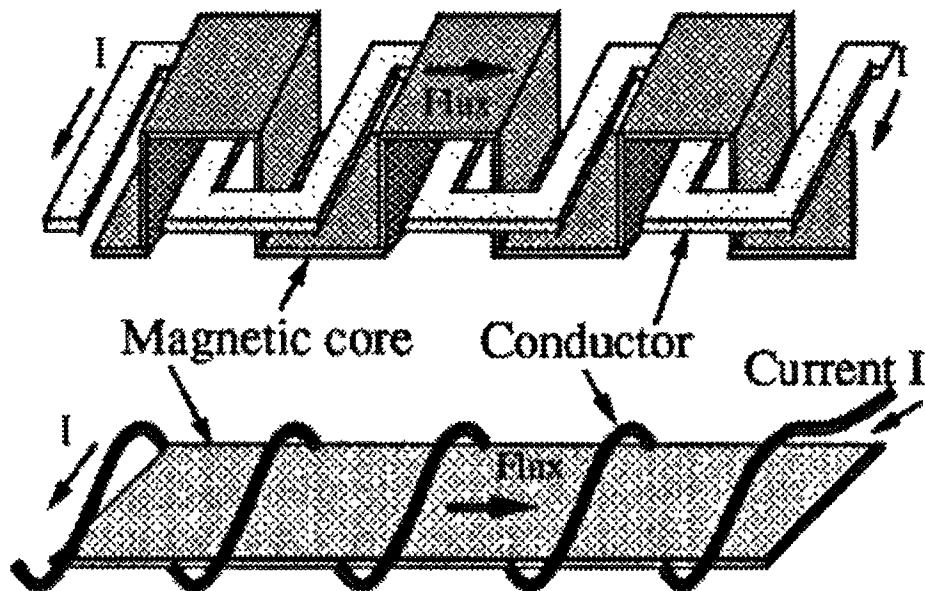
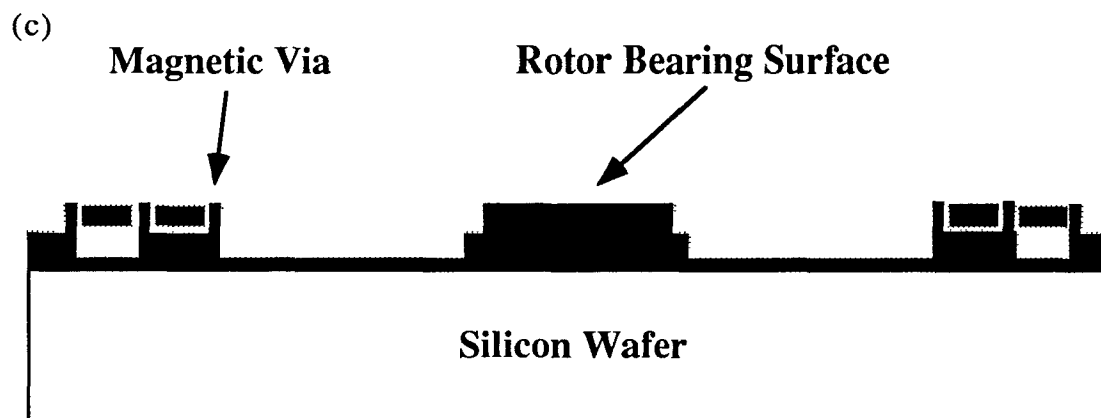
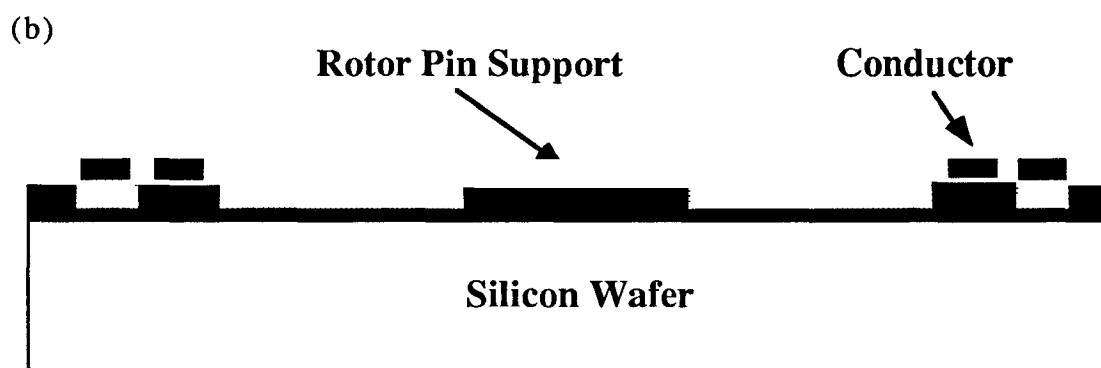
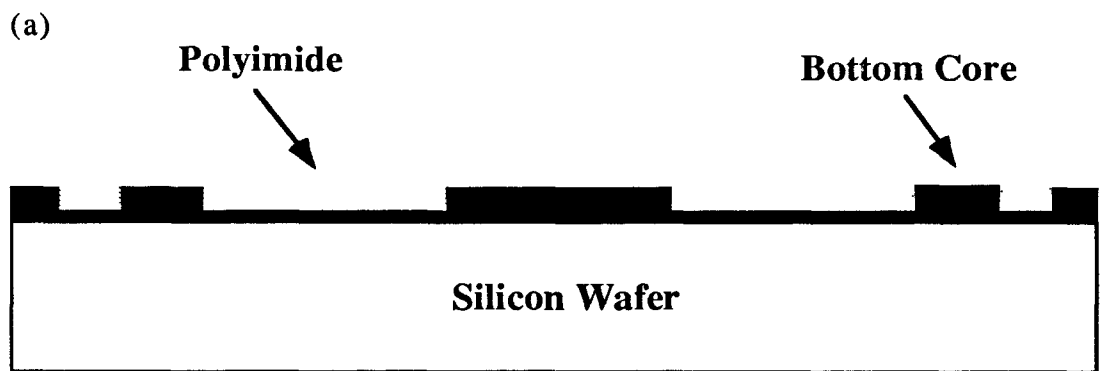


Figure 3.2 Meander type inductive component (top). A multilevel magnetic core is "wrapped" around a planar conductor coil. This structure is similar to the standard inductive component (bottom) [3.1].

3.2.2 Processes

The stator and pin were fabricated by using a polyimide multilevel metal interconnection technique where an electroplated high permeability nickel (81%) -- iron (19%) magnetic core has been used as the magnetic material [3.1]. A fabrication process of this micromotor is shown in Figure 3.3. Step 1: Polyimide deposition, dry etching, and bottom core electroplating. On a 3-inch <100> silicon wafer substrate, deposit 0.6 μm of PECVD silicon nitride. Next chromium(50nm)/copper(200nm)/chromium(70nm) layers are deposited as the electroplating seed layer. Polyimide (Dupont PI-2611) is spun on the wafer in multiple coats to build electroplating molds for the bottom magnetic core. Four coats are used to obtain a 40 μm thick polyimide film. First is "dry etching", and then is "electroplating the bottom magnetic cores". Step 2: Patterning of conductor. A thick planar meander conductor coil copper is plated through a thick photoresist mold. A chromium(50nm)/copper(200nm)/chromium(70nm) seed layer is deposited, and a 60 μm wide copper plating mold is formed in 8 μm thick positive photoresist. Step 3: Magnetic via and rotor pin electroplating. Approximately 10 μm polyimide coat is deposited. Via holes are dry-etched through the polyimide layer between the meander conductors using 100% oxygen plasma and an aluminum hard mask. Step 4: Top core and stator pole electroplating. A 100nm chromium layer is deposited as a dummy seed layer to provide a uniform magnetic top core plating and to protect the defined nickel seed layer. Stator poles, rotor pins, and top magnetic cores are processed on the same



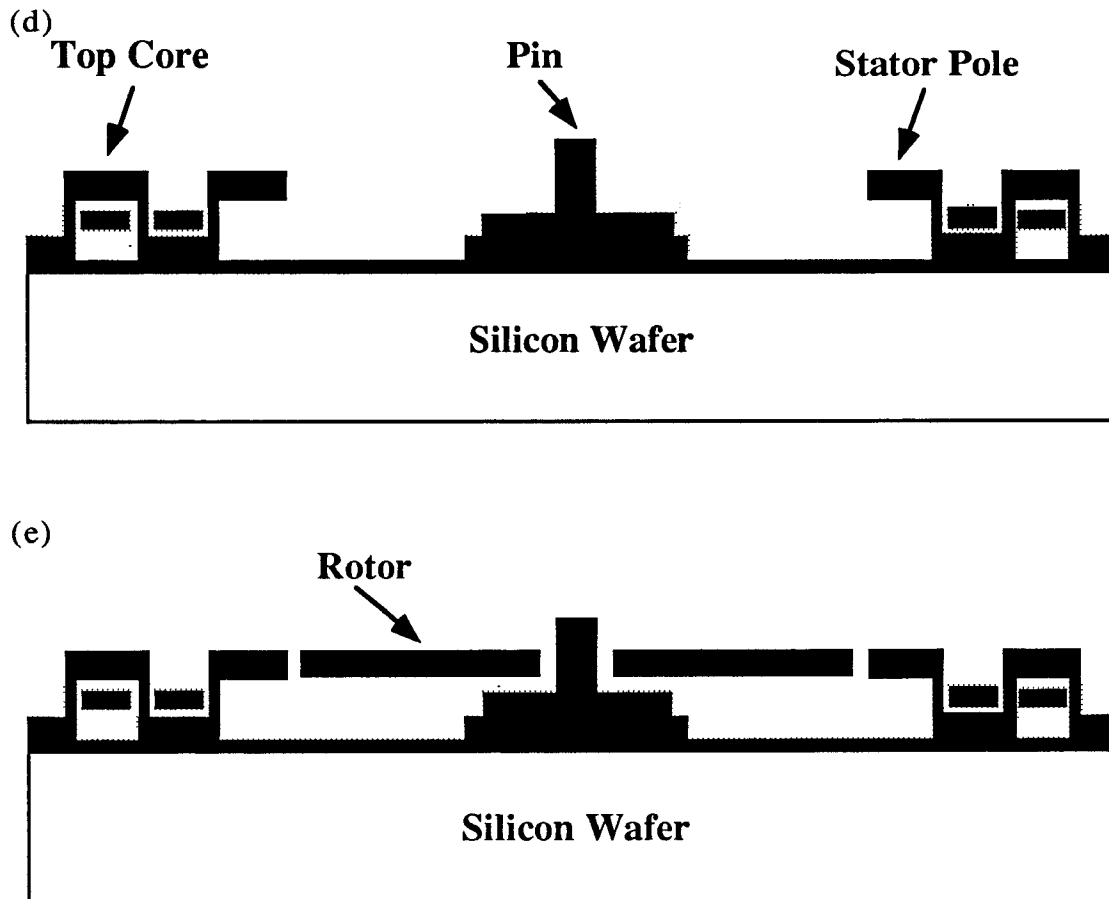


Figure 3.3 Fabrication process for the micromotor: (a) polyimide deposition, dry etching, and bottom core electroplating; (b) patterning of conductor; (c) magnetic via and rotor pin electroplating; (d) top core and stator pole electroplating; (e) rotor and stator microassembly.

level. Step 5: Rotor and stator microassembly. After the rotor is released from the substrate, it is assembled with stators [3.1].

A photomicrograph of the assembled planar variable reluctance magnetic micromotor is shown in Figure 3.4.

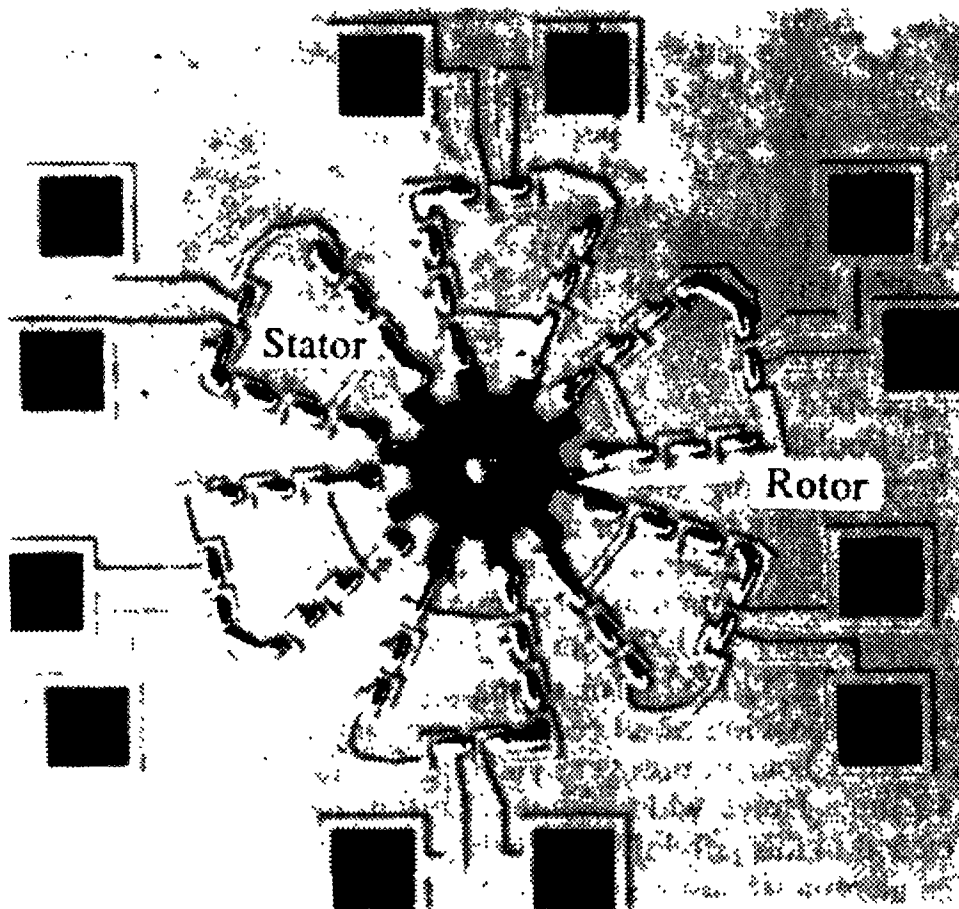
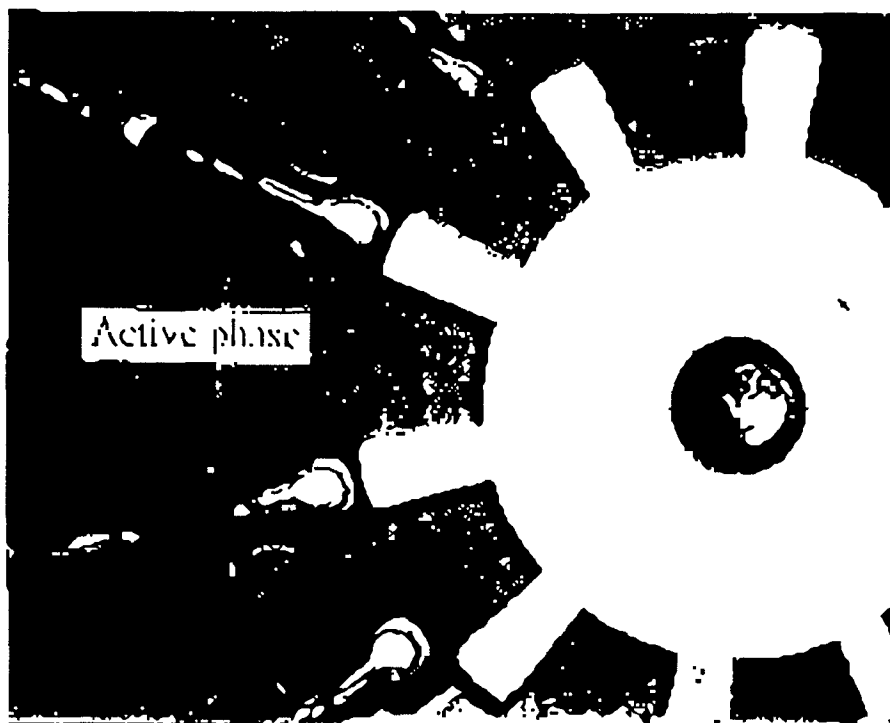
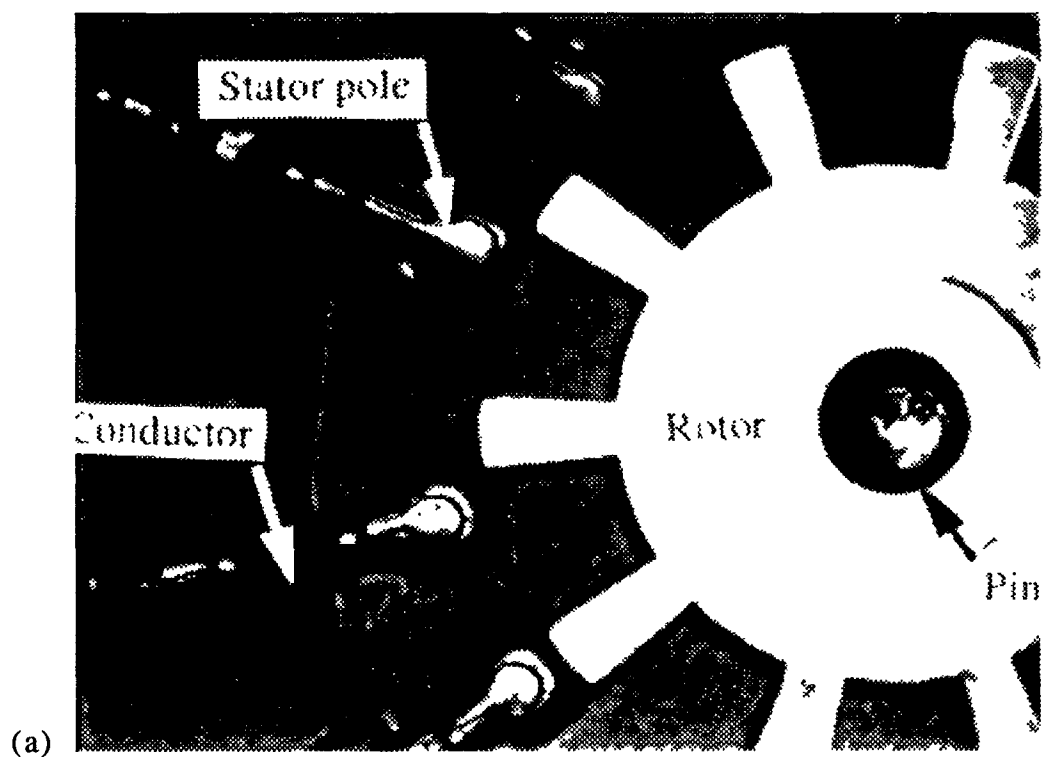


Figure 3.4 Photomicrograph of the fully fabricated micromotor [3.1].



(b) Figure 3.5 Photomicrograph of the actuated rotor. When 0.5A current was applied to each stator phase, 12 degrees of rotation was observed: (a) before current is applied; (b) after current is applied, rotor poles are aligned to the stator poles of the active phase. [3.1].

When phase stator current sequentially excited, the rotating of the rotor can be observed. Figure 3.5 is photomicrograph of the actuated rotor. Figure 3.5 (a) shows the rotor position that is misaligned in comparison to the phase which is to be made active. When applying 0.5A to the active phase, rotational actuation is shown in Figure 3.5 (b) [3.1].

3.3 Performance Modeling

3.3.1 Selected Geometry

The yokeless magnetic micromotor geometry for simulation here is shown in Figure 3.6 (with two stator pole pairs are "wrapped" with coils and active). The stator and rotor are made of nickel-iron. The relative permeability μ_r is 500. The rotor is 600 μm in diameter. The magnetic flux air gap is 5 μm . The rotor thickness is 40 μm . The stator thickness is 120 μm . There are seven turns of coils wrapped around one stator pole pair, 0.5A per turn. This micromotor has 12 stator poles and 10 rotor poles.

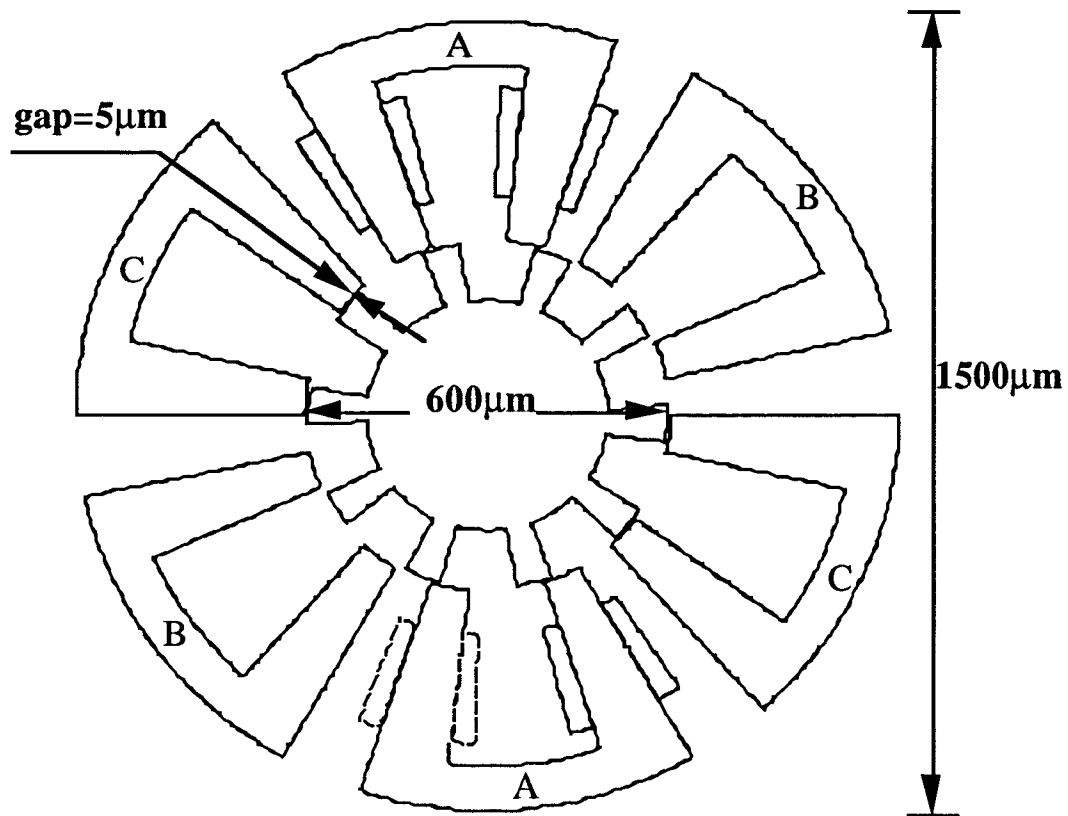


Figure 3.6 Yokeless magnetic micromotor geometry YSMM ($P_s/P_r=12/10$). Drawn to scale using MAXWELL.

3.3.2 First Order Analytical Model

When current is supplied to the stator, a torque is generated on the rotor and tends to move it to a minimum reluctance position where the rotor poles are aligned with the stator poles. The inductance L will vary when rotor rotates. The maximum inductance occurs when the rotor and stator poles are aligned and the minimum inductance occurs when a rotor interpolar axis is aligned with the stator poles. Inductance $L(\theta)$ changes with the rotor position θ . Assumed that magnetic saturation is

negligible and the linear relationship between flux-linkage and driving current is valid at the rotor position θ , the generated torque at the rotor is

$$T = \frac{1}{2} i^2 \frac{dL(\theta)}{d\theta} \quad (3-1)$$

where i is the applied current to the stator.

By using an idealized maximum available energy conversion in energy conversion loop [3.6], the maximum attainable torque from Reference [3.1] is $1.2\mu\text{m}$, and this torque can be expressed as:

$$T = v \frac{N_r B_s^2 g}{4\pi\mu_o r_o \beta} (\text{Nt} \cdot \text{m}) \quad (3-2)$$

where v is the rotor volume; N_r is the torque multiplier representing the number of rotor poles active, B_s is the magnetic flux density in the stator poles at the maximum flux linkage in the aligned position; β is the pole arc (assumed stator and rotor have the same arc); g is the air gap and r_o is rotor radius [3.1].

Equation 3-2 can be used to further derive the first order torque equation of this thesis from Equation 2-10 as follows:

$$B_s = \mu_o H_g = \frac{\mu_o NI}{g} \quad (3-3)$$

$$v = h a r_o \quad (3-4)$$

$$\beta = \frac{a}{2\pi r_o} \quad (3-5)$$

where a is the rotor or stator pole width.

Plug Equations 3-3, 3-4 and 3-5 into Equation 3-2, it turns to:

$$T = (h a r_o) \frac{N_r \left(\frac{\mu_o NI}{g} \right)^2 g}{4\pi \mu_o r_o \left(\frac{a}{2\pi r_o} \right)} = \frac{N_r}{2} \mu_o (NI)^2 r_o h / g \quad (\text{Nt} \cdot \text{m}) \quad (3-6)$$

$$\therefore M = N_r \quad (3-7)$$

\therefore Equation 3-6 and Equation 2-10 is the same.

3.3.3 Numerical Modeling with MAXWELL

The yokeless magnetic micromotor (YSMM) geometry selected for simulation is shown in Figure 3.6. This micromotor has 12 stator poles and 10 rotor poles. The rotor diameter is $600\mu\text{m}$, and the air gap is $5\mu\text{m}$. The rotor pole has a width of 12 degrees, and the stator pole has a width of 12 degrees, too. The magnetic flux for this magnetic micromotor when two stator pole pairs active is shown in Figure 3.7.

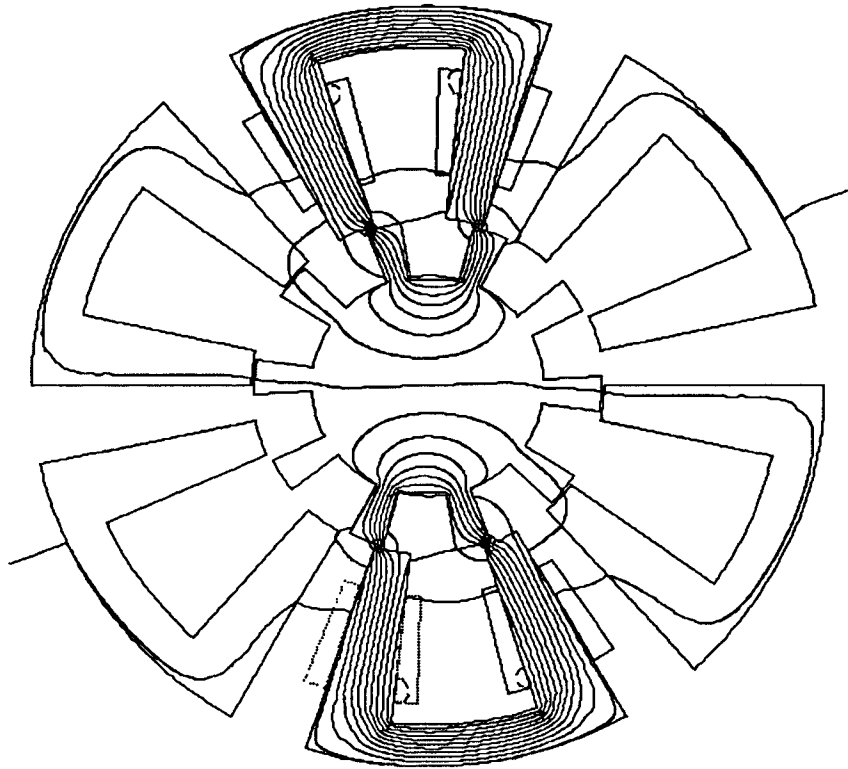


Figure 3.7 Magnetic flux for YSMM with two stator pole pairs active ($P_s/P_r=12/10$). The orientation is the same as Figure 3.6. Rotor diameter = $600\mu\text{m}$.

In this magnetic micromotor YSMM MAXWELL simulation, the stator current phase can be non-overlapping or overlapping. For different current phase sequence, the torque curve of the rotor will be quite different.

When non-overlapping stator currents (as shown in Figure 3.8 (a)) are applied to the stator poles, the torque curve is shown in Figure 3.8 (b). The maximum torque in this case is approximately

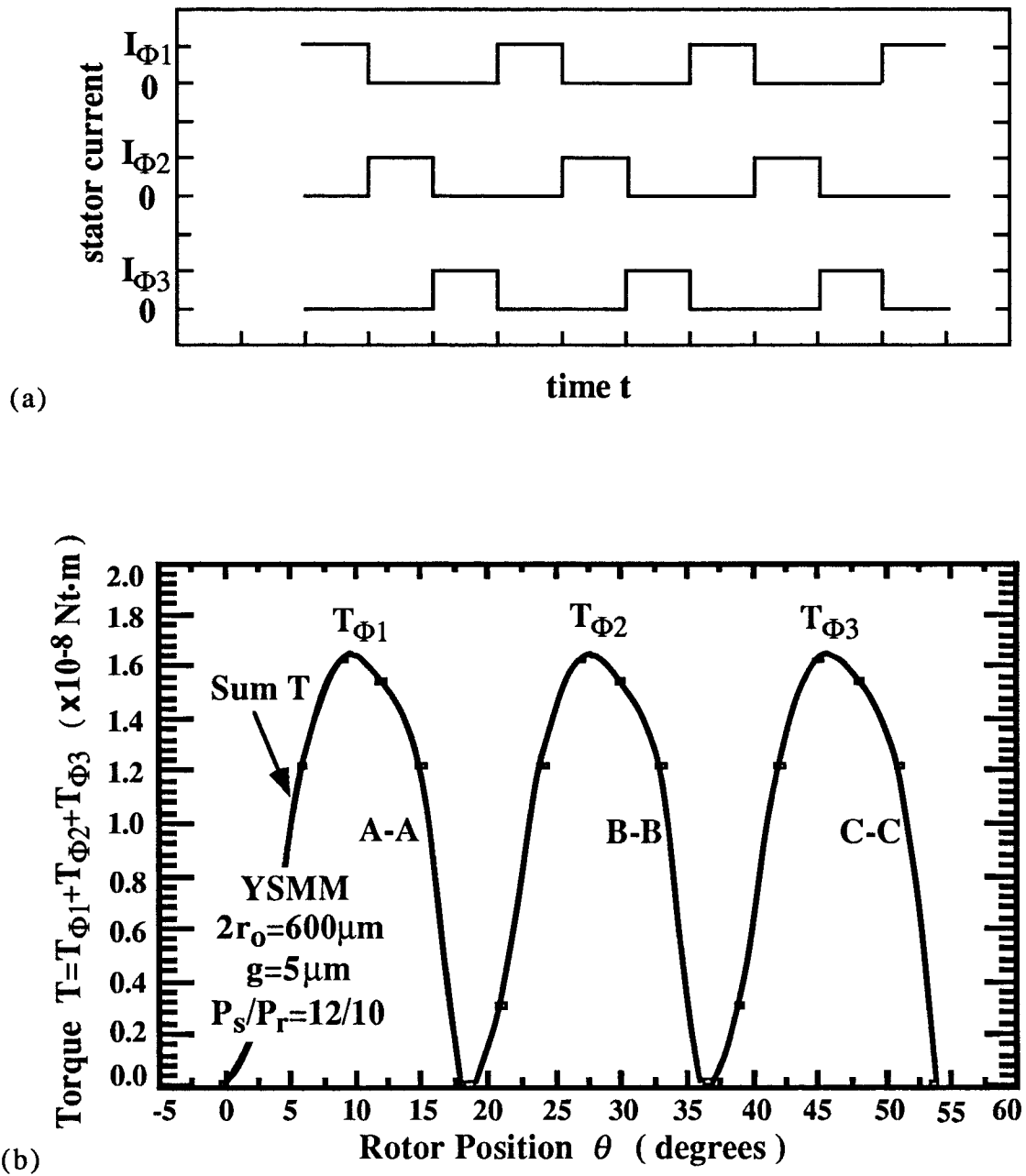
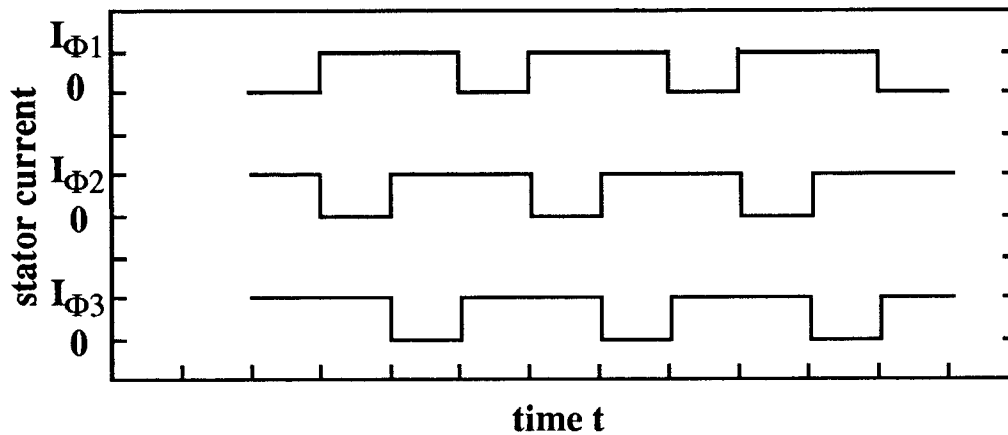


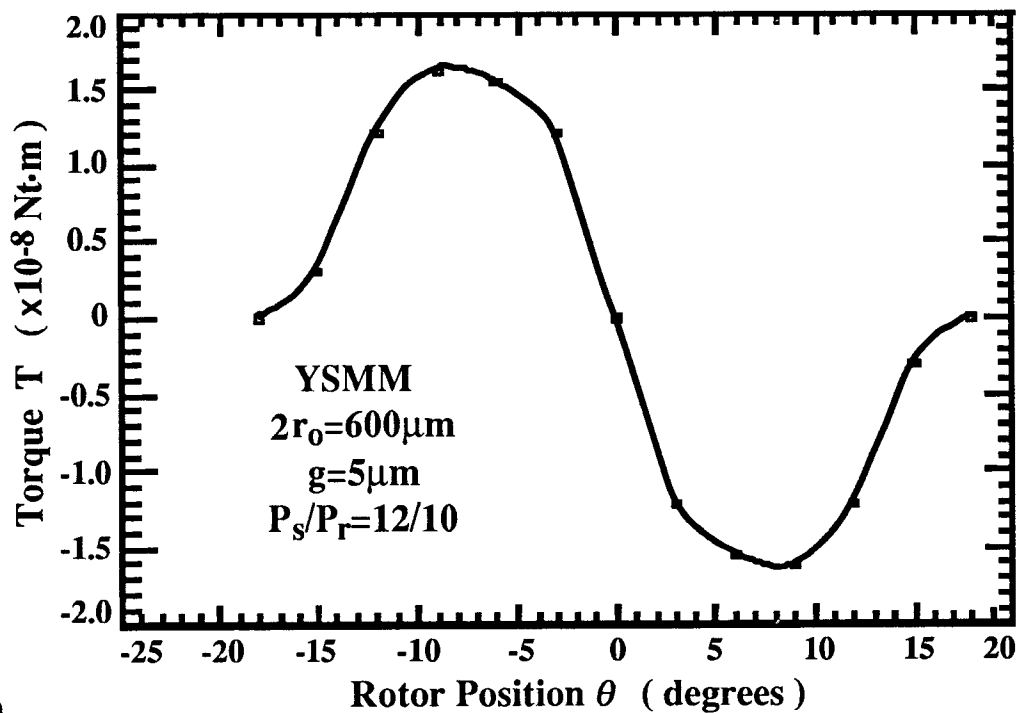
Figure 3.8 Torque curve for YSMM micromotor with non-overlapping current supply phase sequence: (a) stator current supply with non-overlapping phase sequence; (b) sum torque versus rotor position characteristics.

15.5nNt·m, and the minimum torque is 0. The torque is sharp and the torque varies very fast when the rotor position changes.

When overlapping stator currents (as shown in Figure 3.9 (a)) are



(a)



(b)

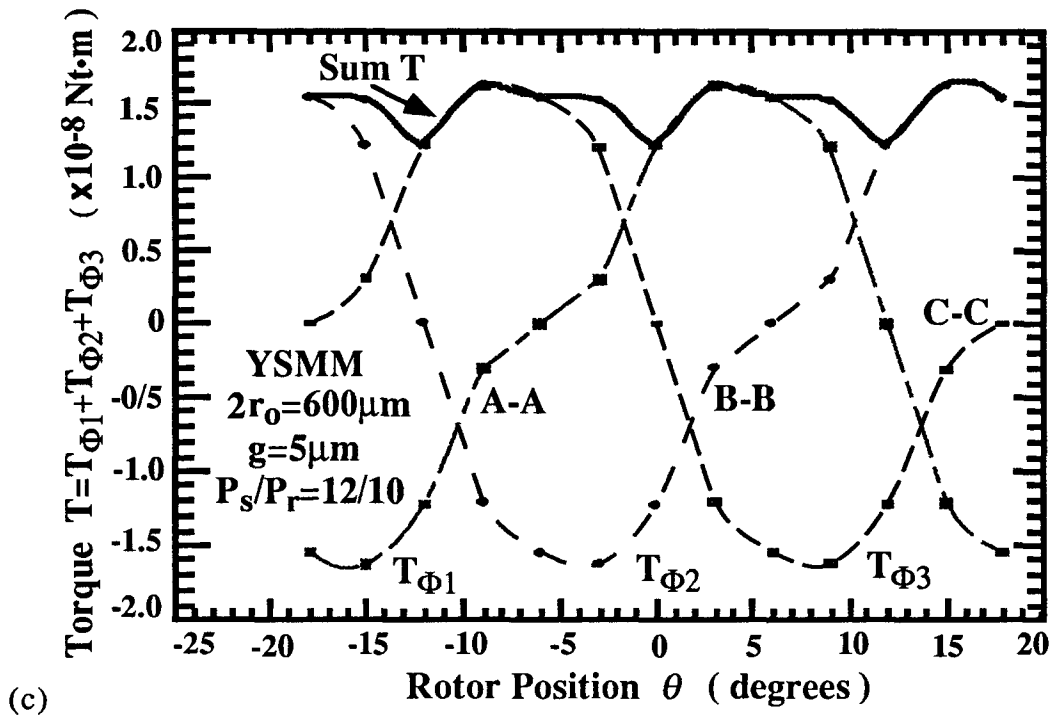


Figure 3.9 Torque curve for YSMM micromotor with overlapping current supply phase sequence: (a) stator current supply with overlapping phase sequence; (b) torque versus rotor position characteristics for a single phase of excitation; (c) sum torque versus rotor position characteristics with three-phase current supply.

applied to the stator poles, the torque curve of Figure 3.9 (b) has been calculated for a single phase of excitation. The sum torque curve with three-phase current supply is shown in Figure 3.9 (c). The maximum torque in this case is approximately $15.5 \text{ nNt}\cdot\text{m}$, and the minimum torque is $12.2 \text{ nNt}\cdot\text{m}$. The sum torque curve is rather flat. The angular variation of the torque in Figure 3.9 is 21%.

The sum torque curve with overlapping current supply is much smoother and flatter, and the average torque is higher for YSMM motor

(can be seen in Figure 3.9 (c)) than the same micromotor is driven by non-overlapping current supply.

Reference [3.1] contains an estimate of torque to be $1.2\mu\text{Nt}\cdot\text{m}$ for the YSMM micromotor configuration of Figure 3.1 with $r_o=600\mu\text{m}$, $g=5\mu\text{m}$, $NI=1.75\text{A}\cdot\text{turns}/(\text{stator pole})$, $h=40\mu\text{m}$.

3.4 Summary of Modeling Results

In this simulation, there is only one geometry. The maximum torque is the same when the micromotor is driven by non-overlapping or overlapping stator current. The micromotor driven by overlapping stator current increases the minimum torque and the average torque. The torque curve is more constant for the case of overlapping current supply.

3.5 References

- [3.1] Chong H. Ahn, Yong J. Kim, and Mark G. Allen, "A planar variable reluctance magnetic micromotor with fully integrated stator and wrapped coils", Fort Lauderdale, Florida, February, 1993. (IEEE Catalog Number 93DH3265-6).
- [3.2] B. Wagner, M. Kreutzer, and W. Benecke, "Linear and rotational magnetic micromotors fabricated using silicon technology", Proc. IEEE Microelectromechanical Systems Workshop, 1992.

- [3.3] H. Guckel and K. J. Skrobis and T. R. Christenson and J. Klein and S. Han, B. Choi and E. G. Novell and T. W. Chapman, "On the application of deep X-ray lithography with sacrificial layers to sensor and actuator construction (The magnetic micromotor with power takeoffs)", Proc. Transducers 91.6th International Conference on Solid-State Sensors and Actuators, Late News, San Francisco, CA, June, 1991.
- [3.4] C. H. Ahn and M. G. Allen, "A new toroidal-meander type integrated inductor with a multilevel meander magnetic core", submitted to IEEE Trans. on Magnetics.
- [3.5] C. H. Ahn and M. G. Allen, "A fully integrated micromagnetic actuator with a multilevel magnetic core", Digest, IEEE Solid State Sensor and Actuator Workshop, Hilton Head, SC, June 1992.
- [3.6] M. R. Harris, "Static torque production in saturated doubly-salient machines", Proc. IEEE, Vol. 33. March 1962.

CHAPTER 4

CONCLUSIONS

Two dimensional computer simulations with MAXWELL have been done for two types of variable reluctance magnetic micromotors: Yoke-type (YTMM) and Yokeless (YSMM). Table 4.1 summarizes the results of modeling for the micromotor designs selected. It also compares the detailed results of this thesis with the approximate results of Reference [2.4] and [3.1].

It can be generally seen from Table 4.1 that:

- With the same air gap dimension, the torque is approximately proportional to rotor diameter.
- If the number of rotor and stator poles is doubled, the torque will double, but the number of the poles is limited by the minimum pole width.
- The maximum torque is proportional to the square of the current-turns (NI), but is inversely proportional to the air gap. As the air gap increases, the torque decreases.
- For the same geometry, if the rotor and stator pole thickness increases, the torque will also increase.
- For the same geometry, the torque will increase when the relative permeability of the magnetic path increases.

These design conclusions listed above are especially important in permitting parameter optimization for micromotor fabrication and production.

Of the five different designs of yoke-type magnetic micromotor simulated (YTMM-1 through YTMM-5), YTMM-5 has the largest torque at 360nNt•m, and YTMM-1 has

Table 4.1: Different magnetic micromotor designs and the relative characteristics

Motor type	P_s / P_r	N·I (A·turns)	Rotor diameter (μm)	Rotor thickness (μm)	Air gap g (μm)	Relative permeability μ_r	T_{\max} ($\times 10^{-8}\text{Nt}\cdot\text{m}$)	T_{avg} ($\times 10^{-8}\text{Nt}\cdot\text{m}$)
YTMM-1	6 / 4	5.4	285	100	3.0	100	7.6	6.65
YTMM-2	6 / 4	5.4	423	100	3.0	100	12.4	9.9
YTMM-3	12 / 8	5.4	285	100	3.0	100	15.8	13.5
YTMM-4	12 / 8	5.4	423	100	4.5	100	15.6	13.6
YTMM-5	12 / 8	5.4	423	100	3.0	100	36.0	26.0
Ref [2.4] YTMM-1	6 / 4	5.4	285	100	3.0	120		2.0
YSMM	12 / 10	1.75	600	40	5.0	500	1.55	1.385
Ref [3.1] YSMM	12 / 10	1.75	600	40	5.0	500	120.0	
YSMM-1	12 / 10	5.4	423	100	3.0	100	12.6	
YSMM-2	12 / 10	5.4	423	100	3.0	500	28.6	
YTMM-6	12 / 8	5.4	423	100	3.0	500	62.33	

the smallest torque at 76nNt•m. The yokeless magnetic micromotor (YSMM) simulated in this thesis has a structure which is very different compared with the yoke-type magnetic micromotor. When these two micromotor types are designed with comparable dimensions, the torque from the YSMM type micromotor could be greater than the expected torque from the YTMM type micromotor if the magnetic path reluctance is small enough. However, the simulation results predicted that the torque of YTMM will be larger than the torque of YSMM with the specific geometry modeled. The yokeless motor configuration (YSMM) exhibits less torque compared to the yoke-type motor (YTMM) due to the increased reluctance of the motor stator frame. The magnetic reluctance affects the performance of the YSMM micromotor more than it does the performance of the YTMM micromotor. When the relative permeability μ_r increases, the torque of YSMM increases much more than the torque of YTMM. In Table 4.1 when the relative permeability μ_r increases from 100 to 500, the torque increases by a factor of 2.16x for the YSMM micromotor, but only by 1.76x for the YTMM when the relative permeability μ_r increases from 100 to 500.

Simulation results show that the maximum torque occurs when the leading edge of the rotor is aligned with the leading edge of the stator. The first order model of Equation 2-10 assumes that the pole-pair of interest does overlap at the maximum torque orientation because of the neglect of fringing field. One must conclude from this comparison that the first order analytical model is not very accurate and it could be in error by perhaps an order of magnitude.

The detailed torque calculations of this thesis are in agreement with H. Guckel et al (Reference [2.4]) torque calculation of 20nNt•m compared to the YTMM-1 micromotor. The torque calculation in this thesis for YSMM micromotor disagrees with the estimate of Reference [3.1]. Calculation details are not mentioned in either Reference [2.4] or [3.1].

APPENDIX A

MAXWELL PROGRAMMING DETAIL (EXAMPLE SCREENS FOR YTMM-5)

The following is a set of screens of MAXWELL modeling for magnetic micromotor design YTMM-5.

1 Meshmaker -- Draw the geometry of the design and make the mesh

(1) Set up the unit of the screen

In the menu, go to "param"--"Units", and choose the unit you want to use in solving the problem from the sub-menu bar shown on the screen (as shown in Figure A.1).

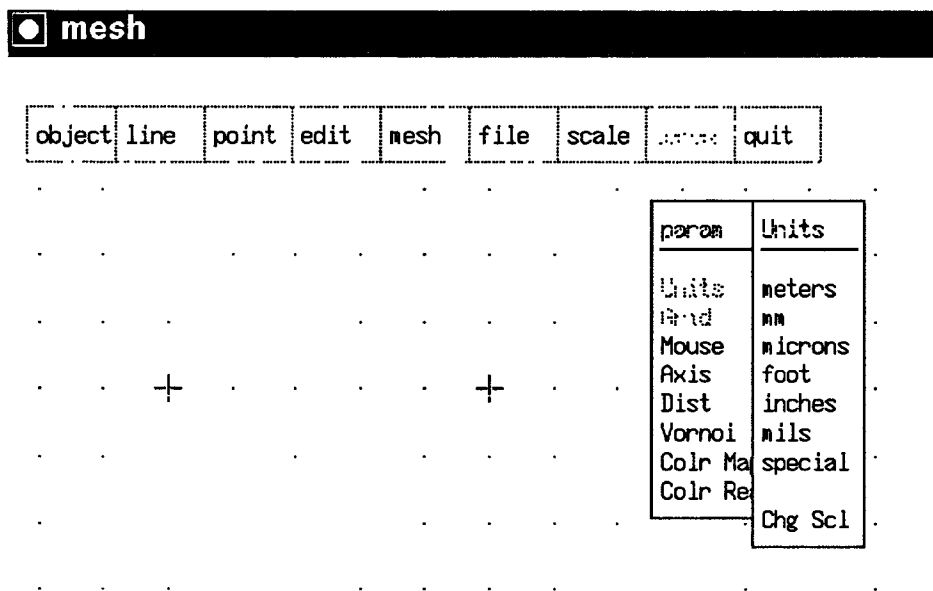


Figure A.1 Screen of setting the unit.

(2) Set up the grid type of the screen

In the menu, go to "param" -- "Grid", it will show the screen (as shown in Figure A.2). There are two kinds of coordinate systems can be chosen: Cartesian or Cylindrical. Either coordinate system can be chosen as for the convenes for drawing the geometry design.

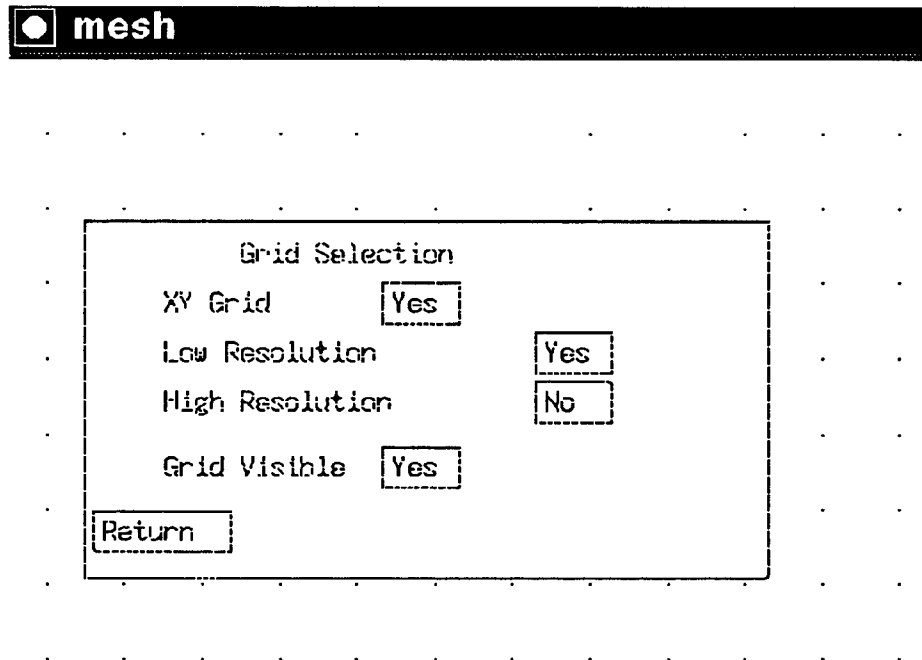


Figure A.2 Screen of setting the grid type.

(3) Set up the dimension of the grid

Go to "param" -- "Axis", a screen of "Axis" sub-menu is shown in Figure A.3. From this sub-menu, the dimension of the axis and the grid can be defined, and also the mouse grid spacing.

The screenshot shows a terminal window titled 'mesh'. The main content is a form for defining a region and grid. It includes fields for 'Upper Left Corner' (X Min, Y Min) and 'Lower Right Corner' (X Max, Y Max). Below these are fields for 'Length of window' and 'Height of window'. There is a checkbox for 'Fit entire region in window' which is currently set to 'No'. There are also fields for 'Number of microns per grid' and 'Mouse grid spacing'. A 'Return' button is at the bottom.

Region Size		microns	
Upper Left Corner		Lower Right Corner	
X Min	-6.7500e+02	X Max	6.7500e+02
Y Min	-5.4000e+02	Y Max	5.4000e+02
Length of window	1.3500e+03		
Height of window	1.0800e+03		
Fit entire region in window	No		
Number of microns per grid		5.4000e+01	
Mouse grid spacing		5.4000e+01	
Return			

Figure A.3 Screen of "Axis" sub-menu.

(4) Draw the problem geometry

In the menu, "object", "line" or "point" sub-menu can be used to draw the problem geometry, whatever the geometry is. A "line" sub-menu is shown in Figure A.4.

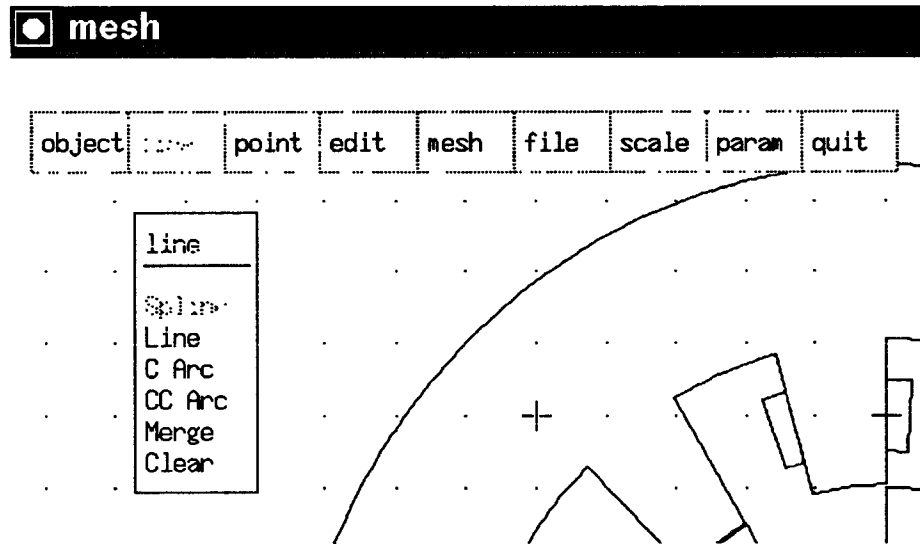


Figure A.4 Screen of "line" sub-menu.

(5) Edit the problem geometry

After the problem geometry has been drawn, the "edit" sub-menu can be used to edit the geometry ("edit" screen is shown in Figure A.5). By using the "edit" sub-menu, part or the whole geometry can be moved, copied or re-sized. And this makes the geometry making much easier.

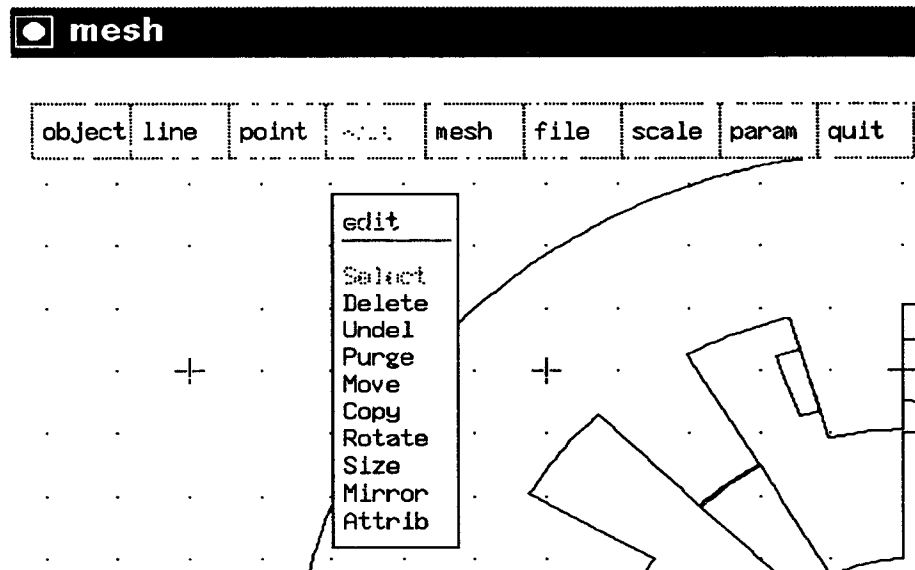


Figure A.5 Screen of "edit" sub-menu.

(6) Do the mesh making

After the geometry is set, mesh making is followed. A screen of "mesh" is shown in Figure A.6. From the menu, choose "Make" to do the initial mesh making. This is the first step of mesh making.

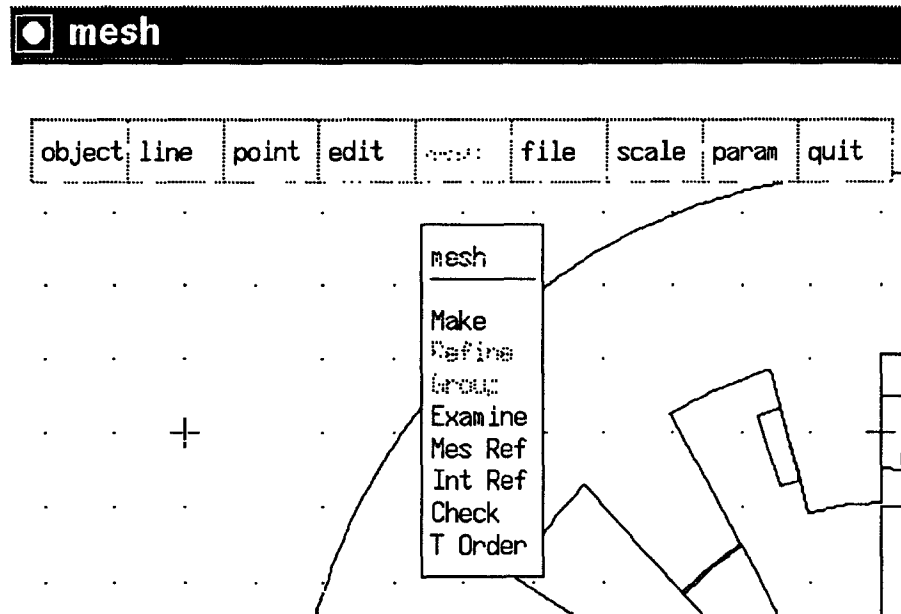


Figure A.6 Screen of "mesh" sub-menu.

(7) Refine the mesh

The initial mesh got from the "mesh" -- "Make" is pretty rough, so the refinement of the mesh is necessary. The "mesh" --"Refine" sub-menu is shown in Figure A.7. Different kinds of refinement can be chosen from this sub-menu according to the different geometry refinement required from the problem.

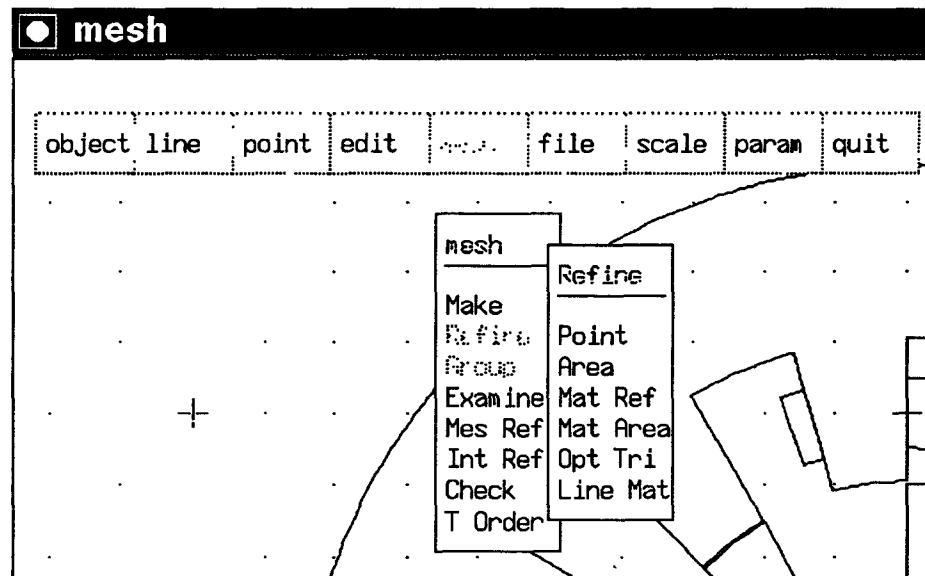
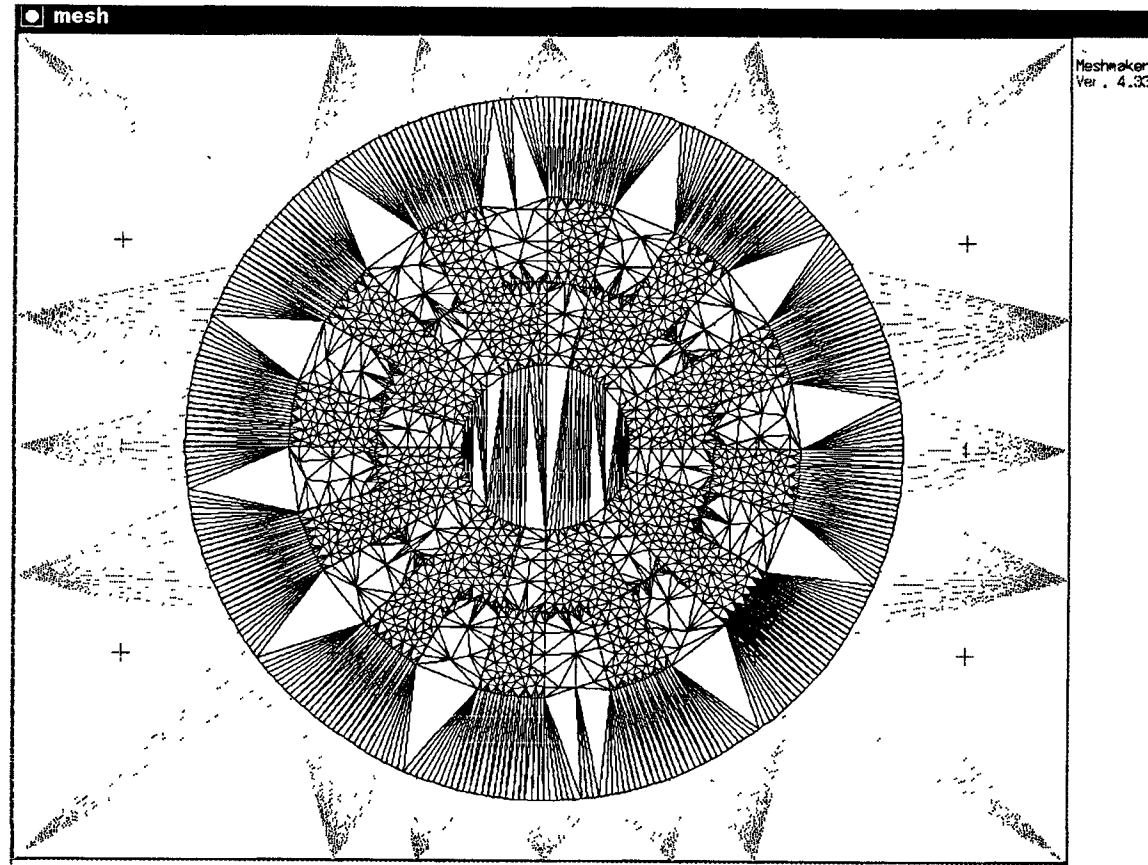


Figure A.7 Screen of "Refine" sub-menu.

After the refinement has been done, the mesh of the whole geometry area for this magnetic micromotor YTMM-5 is shown in Figure A.8.

Figure A.8 Screen of geometry with mesh



(8) Save the file

After the mesh is done and it is ready to solve the problem, save this as a file and exit from the meshmaker. A sub-menu of the "file" is shown in Figure A.9. After having saved the file, go to the "quit" to exit.

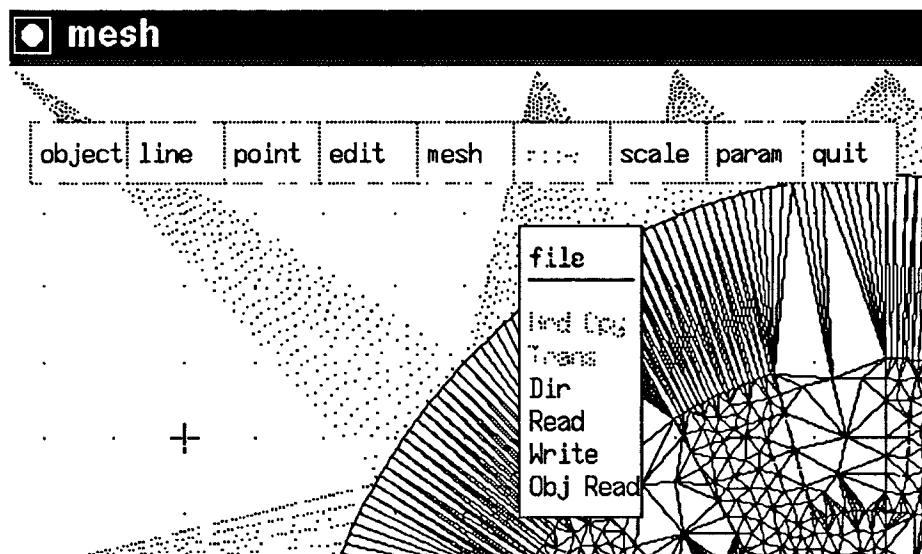


Figure A.9 Screen of "file" sub-menu.

2. Magnetostatic Solver -- Solve the problem

(1) Retrieve the file and set up the parameters for the problem

Use the "file" sub-menu and retrieve the file saved in Meshmaker. Then choose the "setup" -- "Att Set" sub-menu (as shown in Figure A.10). If we click and choose this function, a series of screens will appear and the parameters can be set through these screens. These screens are shown as Figure A.11.

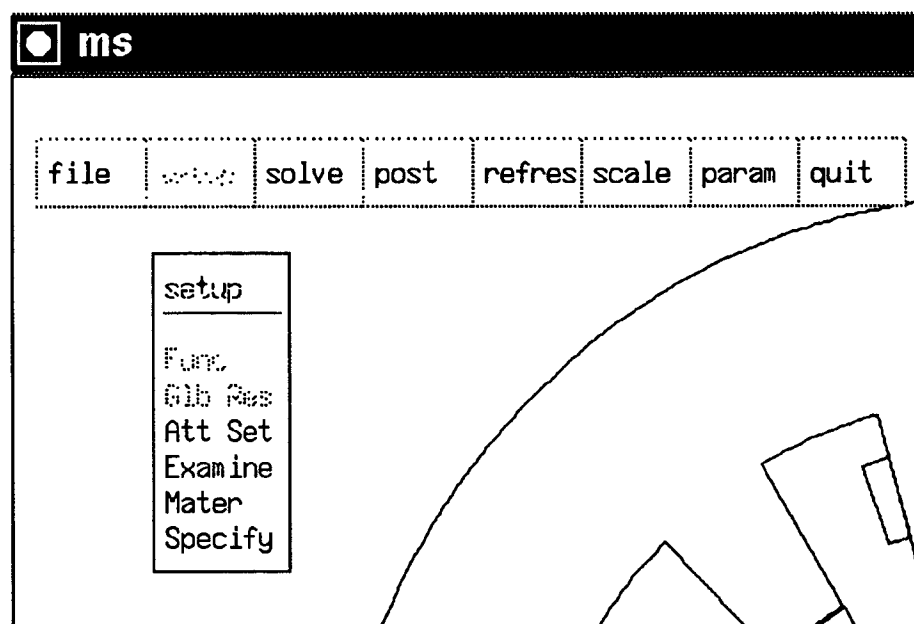


Figure A.10 Screen of "Att Set" sub-menu.

ms

Material Name : a2
 Area of region is 8.5358e-10

Existence Yes

Anisotropy Permeability No

Functional mu No mu

Perm. Magnet No

Functional Current No

Current Density Total Current

Continue entry Yes Accept Yes

(a)

ms

Material Name : a2+

Area of region is 8.5358e-10

Existence Yes

Anisotropy Permeability No

Functional mu No mu

Perm. Magnet No

Functional Current No

Current Density Total Current

Continue entry Yes Accept Yes

(b)

ms

Material Name : a1-
 Area of region is 9.5358e-10
 Existence Yes
 Anisotropy Permeability No
 Functional mu No mu 1.0000e+00

Perm. Magnet No

Functional Current No
 Current Density -5.6629e+09 Total Current -5.4000e+00

Continue entry Yes Accept Yes

(c)

ms

Material Name : a1+
 Area of region is 9.5358e-10
 Existence Yes
 Anisotropy Permeability No
 Functional mu No mu 1.0000e+00

Perm. Magnet No

Functional Current No
 Current Density 5.6629e+09 Total Current 5.4000e+00

Continue entry Yes Accept Yes

(d)

ms

Material Name : s1
Area of region is 4.1910e-07

Existence Yes

Anisotropy Permeability No

Functional mu No mu

Perm. Magnet No

Functional Current No

Current Density Total Current

Continue entry Yes Accept Yes

(e)

ms

Material Name : stator
Area of region is 1.0566e-07

Existence Yes

Anisotropy Permeability No

Functional mu No mu

Perm. Magnet No

Functional Current No

Current Density Total Current

Continue entry Yes Accept Yes

(f)

ms

Material Name : rotor
 Area of region is 7.3270e-08

Existence Yes

Anisotropy Permeability No

Functional μ No μ

Perm. Magnet No

Functional Current No

Current Density Total Current

Continue entry Yes Accept Yes

(g)

ms

Material Name : background
 Area of region is 7.9616e-07

Existence Yes

Anisotropy Permeability No

Functional μ No μ

Perm. Magnet No

Functional Current No

Current Density Total Current

Continue entry Yes Accept Yes

(h)

Figure A.11 Screens of setting the parameters for different materials in this problem: (a), (b), (c), (d) set the currents to the coils wrapped around one stator pole pair; (e) set the relative permeability μ_r to the stator (yoke and poles); (f) set the parameters for the area between the stator and rotor; (g) set the relative permeability μ_r to the rotor; (h) set the parameters to the program running background.

(2) Pick the boundary for solving the problem

Go to the "solve" -- "B Pick" sub-menu (as shown in Figure A.12), choose any command and set up a boundary for this problem.

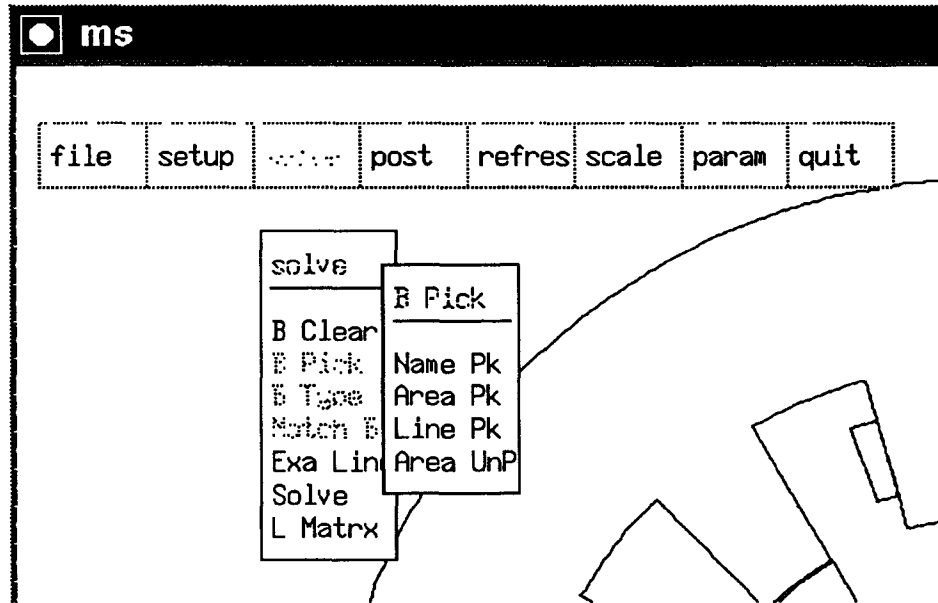


Figure A.12 Screen of "B Pick" sub-menu.

(3) Define the type of the boundary chosen before

After choosing the boundary, then to define the type of this boundary.

A "B Type" sub-menu is shown in Figure A.13. "Balloon" is chosen as the boundary for solving this problem.

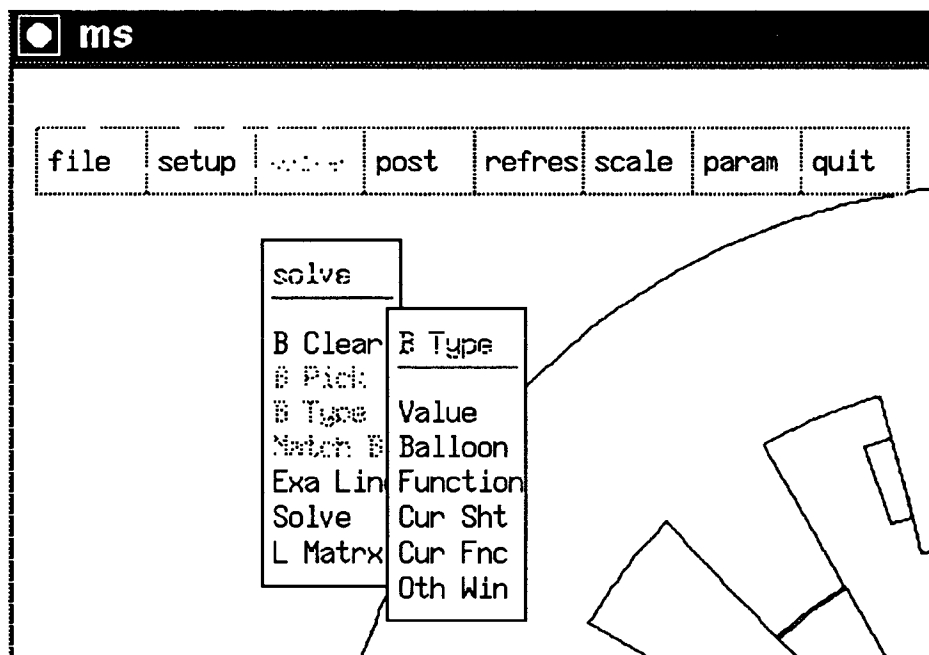


Figure A.13 Screen of "B Type" sub-menu.

(4) Solve the problem

Go to "solve" -- "Solve" and solve the problem. A screen of "Solve" sub-menu is shown in Figure A.14. After the "solve" has finished, some unknown parameters such as torque can be calculated.

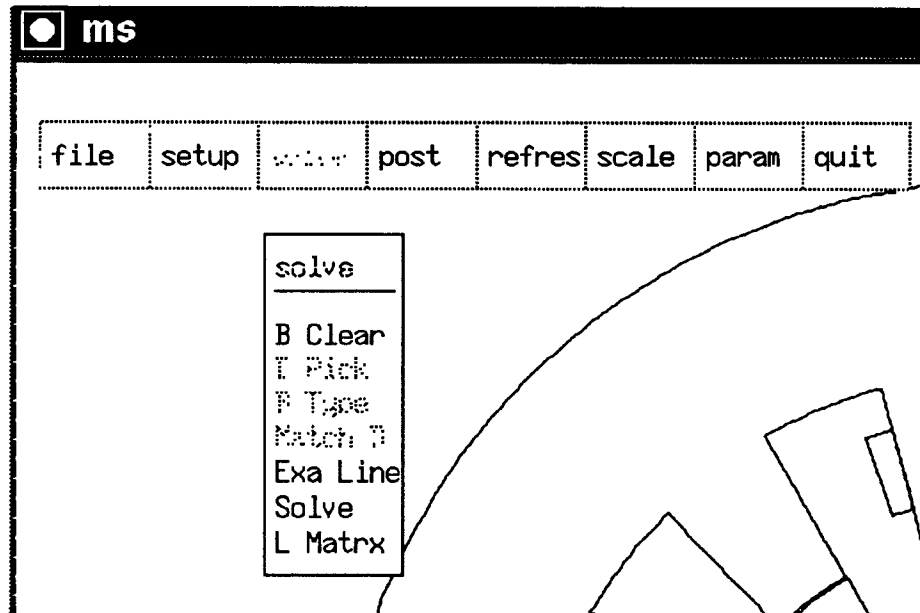


Figure A.14 Screen of "Solve" sub-menu.

(5) Calculate some unknown parameters

Once the solve has completed, go to "post" -- "line" sub-menu (as shown in Figure A.15). First, use "Enter", "Crc Line" or "Obj Line" to choose a line for calculation.

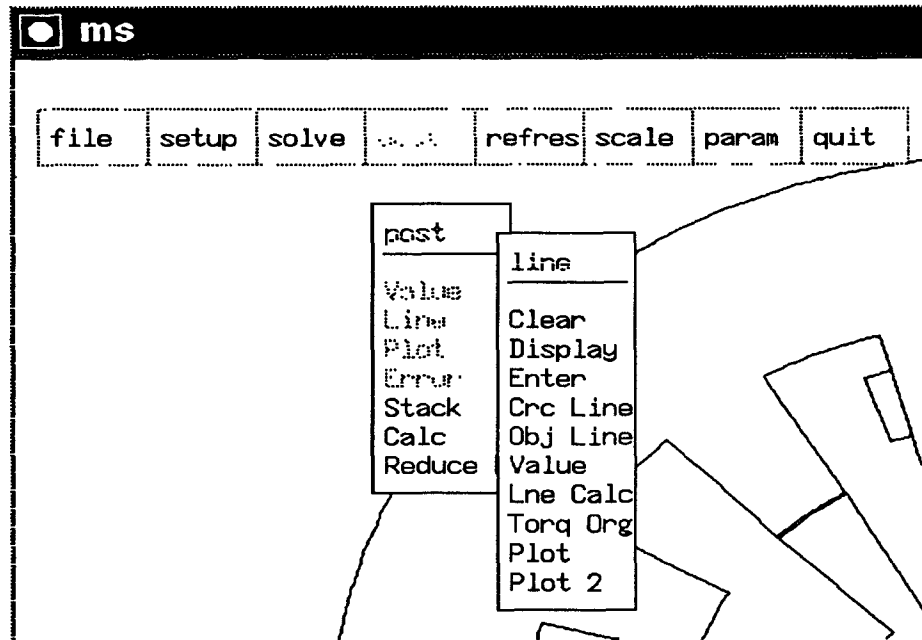


Figure A.15 Screen of "post" -- "line" sub-menu.

Then go to "Lne Calc" sub-menu (as shown in Figure A.16) to calculate some unknown parameters like torque. If calculate the torque, press "t", then key in the "Number of points". Then, press "Return" key to start calculating the torque.

```

ms
Line Expression
Line Expression

/

. clear solution      . add                . function
. copy and enter line . multiply           . integrate
. name line          . scalar multiply   . normal
. pop register       . error analysis    . tangent
. roll registers     .                   . value
. exchange registers Force
                   : Torque

.: Go to Number Calc
.: Output to file
.: Read from file

Computing y tensor
Computing Fy normal to surface
Number of points [100] 2000
|

```

Figure A.16 Screen of "Lne Calc" sub-menu.

The calculating result of the torque is shown in Figure A.17, and the calculating expression is also shown in the figure. The result here is MKS unit, so the unit for the torque is Nt.m. The "-" sign of the torque just means the direction of this torque is counter-clockwise.

```

ms
Number Register      Line Expression
-----
/

.. clear solution      add          - function
.. copy and enter line multiply       integrate
.. name line          .. scalar multiply  : normal
.. pop register       .. error analysis   : tangent
.. roll registers
.. exchange registers - Force
                          - Torque
.: Go to Number Calc
.. Output to file
.. Read from file

.: quit

The result is -1.402928e-03
Enter in number calculator [n] y
ctrl-f : Line Calc Command ^

```

Figure A.17 Screen of "Line Calc" sub-menu with calculating result.

(6) Get plots from MAXWELL solving result

Go to "post" -- "plot" sub-menu (as shown in Figure A.18), different kinds of plots can be got. For example, if we want to get the magnetic flux, just choose any one choice from the "plot" sub-menu . If "Equi" is chosen, a screen for that is shown in Figure A.19, where settings for the plot can be defined. After we click the "Return" box, the magnetic flux plot comes up (some kind like the plot in Figure 2.18).

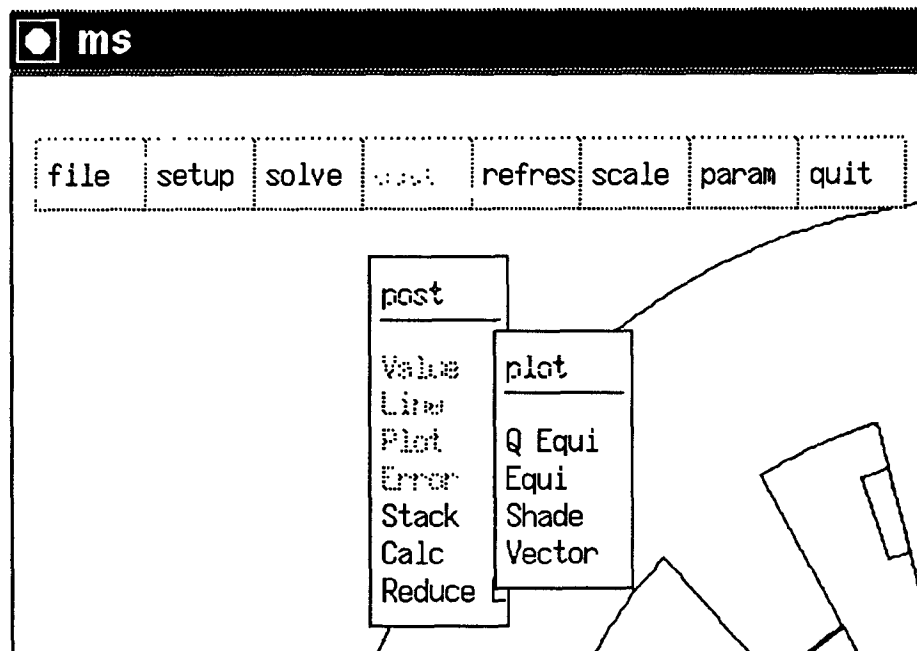


Figure A.18 Screen of "plot" sub-menu.

ms

Maximum Value	<input type="text" value="1.7858e-05"/>
Minimum Value	<input type="text" value="-1.7858e-05"/>
Divisions	<input type="text" value="20"/>
Color	<input type="text" value="1"/>
+/- Shading	<input type="text" value="No"/>
Shading	<input type="text" value="No"/>
Plot Quality	
Good	<input type="text" value="No"/>
Better	<input type="text" value="No"/>
Excellent	<input type="text" value="Yes"/>
Abort Plot	<input type="text" value="No"/>
	<input type="text" value="Return"/>

Figure A.19 Screen of "Equi" settings.

APPENDIX B

BOUNDARY CONDITIONS FOR 2-D AND 3-D MAXWELL SIMULATIONS IN MAGNETOSTATIC PROBLEM

Boundary condition is very important in MAXWELL simulations, because it gives the initial condition for the problem. For 2-D and 3-D simulations, the types of boundary are some kind of similar but a little bit complex for 3-D simulation.

B.1 Boundary Conditions for 2-D MAXWELL Simulations

A simple example is shown in Figure B.1 which displays the magnetic flux and illustrates the effect of the different boundary conditions.

(1) Neumann (Natural)

This is the default of MAXWELL. At an outer boundary, it assumes that the tangential component of the magnetic field (\mathbf{H}) goes to zero. At the interface between any two meshed objects, it models the general condition in which the tangential component of \mathbf{H} and the normal component of \mathbf{B} are continuous.

In Figure B.1, the left edge of the problem space has been set to a Neumann boundary. The lines of magnetic flux are perpendicular to this

boundary. Physically, this represents the case in which another circle carrying current lies off screen and to the left, forming a mirror image of the problem. The Neumann boundary in *Magnetostatic* solver allows the user to simplify problems by taking advantage of symmetry [B.1].

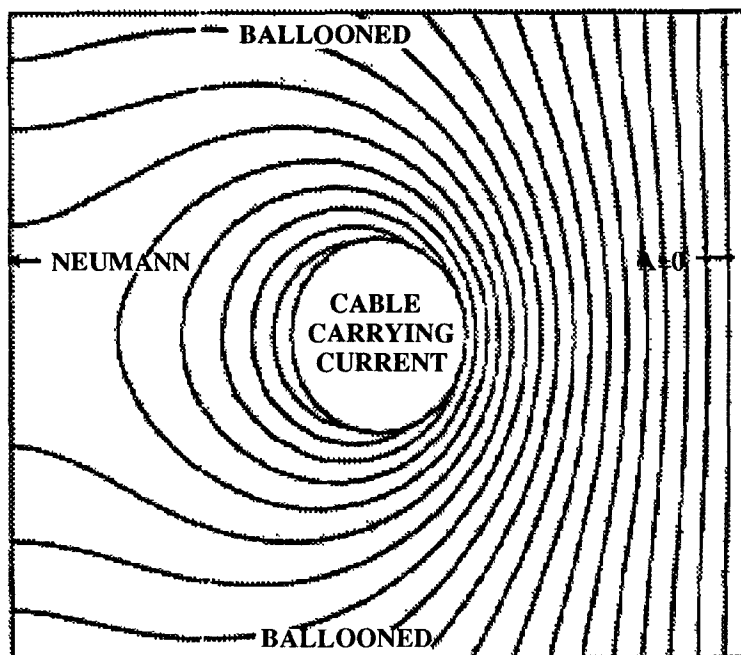


Figure B.1 Lines of magnetic field at Neumann, Dirichlet and Ballooned Boundaries [B.1].

(2) Dirichlet

It can be used to specify the value of A at an interface or boundary. A constant value of A results in the normal component of B going to zero along the boundary.

In Figure B.1, the boundary on the right edge of the screen is a Dirichlet boundary that has been set to $A=0$. The lines of B are tangential to this boundary and are unable to cross the boundary [B.1].

(3) Balloon

This boundary can only be applied to the outer boundaries of the background which border the edge of the problem space. It simulates open boundary conditions by modeling the background as extending to infinity. The magnetic vector potential goes to 0 at infinity.

In Figure B.1, the top and bottom boundaries have been set to ballooned boundaries, indicating that the background extends to infinity in these directions. Equipotential contours are not necessarily either perpendicular or normal to these boundaries [B.1].

B.2 Boundary Conditions for 3-D MAXWELL Simulations

There are four types of boundary conditions for 3-D MAXWELL simulation and are listed below.

(1) Natural

At the surface between two objects, the natural condition is simply that the appropriate normal and tangential components of the B -field and the H -field are continuous. No additional conditions are enforced. It is used to model the ordinary H -field behavior on interface boundaries. All surfaces are initially set to this boundary condition [B.2].

(2) Neumann

If an outer boundary (a surface exposed to an unmeshed region) is set to be a Neumann boundary, the system forces the \mathbf{H} -field to be tangential to that boundary. This boundary condition is used to model the case in which magnetic flux is prevented from crossing the boundary. This is the default boundary condition in *Magnetostatic* solver that all outer boundaries in a magnetostatic problem are set to Neumann boundaries [B.2].

(3) Dirichlet

This is the boundary condition that tangential components of the \mathbf{H} -field are set to pre-defined values. By setting the tangential components of the \mathbf{H} -field to 0 along that surface, the \mathbf{H} -field can be normal to a surface. This condition is most useful in defining a plane of symmetry that cuts perpendicularly through the flux. All surfaces that are set to Dirichlet boundaries must be contiguous. If two groups of Dirichlet boundaries are separated by a Neumann boundary, there is no unique solution to the problem, and the system produces unexpected results [B.2].

(4) Matching

It can be used to force the field solution at one surface to match the magnitude and direction (or the negative of the direction) of the field solution at another surface. This allows the user to use symmetry when modeling a periodic structure where the \mathbf{H} -field is neither tangential to nor normal to the plane of symmetry [B.2].

B.3 References

- [B.1] MAXWELL 2-D Field Simulation User's Guide, June 1991.
- [B.2] MAXWELL 3-D Field Simulation (Version 1.2) User's Guide, April 1992.